Contactless Vital Signs Monitoring via Radar Sensing for Sleep Applications

Master Thesis Report

Yichuang Han

Contactless Vital Signs Monitoring via Radar Sensing for Sleep Applications

Dissertation

to obtain the degree of Master of Science
in Electrical Engineering
at Delft University of Technology
to be defended publicly on Friday August 27, 2021 at 09:00 AM

by

Yichuang Han

born in Shaanxi, China.

This thesis has been approved by the

Supervisor: prof. DSc. Alexander Yarovoy
Daily supervisor: Dr. Francesco Fioranelli

Thesis Committee:

Prof. DSc. Alexander Yarovoy,	MS3 TU Delft
Dr. Borbála Hunyadi,	CAS TU Delft
Dr. Francesco Fioranelli,	MS3 TU Delft

*Keywords: Sleep apnea detection, Applied machine learning, Time-…
frequency analysis, UWB radar*

An electronic version of this dissertation is available at
http://repository.tudelft.nl/.

Acknowledgements

I will always cherish the memories of the two years I spent studying and living at TU Delft. Like a jar the campus housed the infinite tenderness and passion, offering me whatever insights from people who studied here even years before I came. It offers me well-stocked library, sunsets at EWI, the moon over the pathway and, most importantly, warm and friendly people. This thesis is not just an essay composed to get a degree, it is a condensation of a period, a work of art that blends the creative process with the final result. The smoothness and hardship of the process, the perfection and imperfections of the outcome are all things I treasure. Thus I would like to offer my most sincere thanks to those who have helped and encouraged me during this journey.

First of all, I would like to express my great gratitude to my supervisor, Prof. Alexander Yarovoy, for giving me the general direction of my research and a lot of useful advice. He attends the mid-term reports and defences of all masters students whenever possible, giving his holistic and professional opinion, which has inspired me in terms of his academic expertise and research philosophy. I learned from him the qualities that a researcher should have: clear research objectives and a research plan, in-depth analysis of research results, the creation of scholarly articles, the delivery of self-contained lectures and, above all, always being open and rigorous.

I sincerely appreciate the guidance of my daily supervisor Dr. Francesco Fioranelli, for the support and enthusiastic encouragement he has provided when I have encountered difficulties. Every week I met with him, he gave me constructive advice that helped me to work more effectively and gave me a broader understanding of the issues involved in this thesis project. He was always very prompt in responding to my questions, even when he was on holiday. For so many times, he spent hours and days revising my writing drafts, suggesting changes to my thesis in general and in detail, guiding me to write in an academic manner and making clear demonstrations. I am very thankful for his support and instruction, which will always be invaluable in my future career.

I would also like to thank all the professors and PhD as well as MSc students at Microwave Sensing, Signals and Systems Group who together have created a harmonious and vigorous atmosphere in MS3, for asking questions, exchanging ideas and giving unique insights at the meetings every Friday, each of whom has helped me greatly with my research. Their clear and structured presentations have given me insights into how to organise academic presentations and sometimes inspired me to solve problems that were bothering me in my final project. I also wish to thank Dr. Jianping Wang for his very valuable advice and help; Ph.D. Sen Yuan and MSc. student Zhuoyu Chen from TJU, thank you for discussing with me about the problem of failure in phase demodulation, Ms. Esther de Klark thank you for helping me to schedule and reschedule my defence. Thanks to several other MSc. students who were also under Dr. Francesco's supervision with me for the discussion we had about the study.

My sincere thanks extend to the fourteen volunteers in our group who helped me with my experiment, without whom I would not have been able to finalise my project. Moreover, I would like to thank Dr. Hong Hong from Nanjing University of Science and Technology and Huai'an First People's Hospital, Jiangsu, China, for being willing to share the radar recording of real patients with us. This set of data makes it possible to validate the value of algorithms we proposed in clinical applications.

Special thanks to all my friends, especially Anqi Chen and Xinhan Liu for their continued encouragement and accompany in this tough Covid-19 period. I also wish to thank my family who always love and support me and offer me that kernel of themselves, somehow– the heart and spirit that deals not in words, traffics not with dreams and is untouched by time, by joy, by adversities.

I would also like to thank a few books that have brought me comfort and helped me get through this lonely and difficult period of isolation: *The Plague* by Albert Camus, *Love in the Time of Cholera* by García Márquez and *Ficciones* by Jorge Luis Borges. Additionally, thanks to the music (e.g. *Date* by Faye Wang, *Myself* by Kary Ng, *Nightingale* by Yanni, *La Vita* by Il Volo and *Gracias* by Pablo Alborán) and the bright, warm summer in Delft. All of these people and events mentioned above have brought me lasting happiness. If I have any modest achievement in the future, it will be inseparable from them. I wish them all the best and peace and prosperity in the future.

Yichuang Han
Delft, August 2021

Contents

Acknowledgements v

List of Figures ix

List of Tables xii

1 Thesis Introduction and Literature Review 1

1.1 Background . . . 1
1.2 Contribution of the Research . . . 2
1.3 Overview of Vital Signs Monitoring Technologies . . . 3
1.4 Radar - Based Sleep Apnea Detection: State of Art . . . 3
1.5 Structure of the Thesis . . . 6

2 Signal Models And Radar System for Sleep Apnea Detection 9

2.1 Signal Models For Respiration And Heartbeat . . . 9
2.1.1 Physiology Motion Of Respiration And Heart System . . . 9
2.1.2 Signal Model for Cardiopulmonary Activity . . . 11
2.2 Signal Models For Different Types Of Apnea . . . 14
2.2.1 Obstructive Sleep Apnea . . . 14
2.2.2 Central Sleep Apnea . . . 15
2.2.3 Mixed Sleep Apnea . . . 16
2.3 Radar System For Sleep Apnea Detection . . . 16
2.3.1 Continuous Wave Radar . . . 17
2.3.2 Ultra Wide Band Radar . . . 19
2.3.3 Frequency Modulated Continuous Wave Radar . . . 20
2.4 Conclusion . . . 22

3 Algorithms Developed for Sleep Apnea Detection 24

3.1 Signal Processing and Classification Pipeline . . . 24
3.2 Pre-processing Algorithms . . . 25
3.2.1 Phase Extraction . . . 25
3.2.2 Short-Time Fourier Transform . . . 26
3.2.3 Discrete Wavelet Transform . . . 28
3.2.4 Envelope Extraction . . . 31
3.2.5 Noise reduction and Signal Smoothing Based on Variational Mode Decomposition . . . 33
3.3 Vital Signs Frequency Estimation . . . 38
3.4 Sleep Apnea Detection . . . 39
3.4.1 Threshold-based detection . . . 39
3.4.2 Apnea Detection using Applied Machine Learning . . . 40

3.5 Conclusion . . . 42

4 Simulation Results **44**
4.1 Strategy of Monte Carlo Simulation . . . 44
4.1.1 Evaluation Metrics . . . 45
4.2 Monte Carlo Simulation for Different Subjects . . . 46
4.2.1 Error Analysis . . . 46
4.3 Monte Carlo Simulation for the Environment . . . 47
4.3.1 Result for Frequency Estimation . . . 48
4.3.2 Simulation in Supine Position . . . 49
4.3.3 Simulation for different sleeping posture . . . 49
4.3.4 Error Analysis . . . 52
4.4 Conclusion . . . 52

5 Experimental validation **54**
5.1 Experimental Environment Setup . . . 54
5.2 Pre-processing Results . . . 56
5.2.1 Signal Reconstructed by Phase Demodulation. . . . 56
5.2.2 Signal Reconstructed by Short-time Fourier Transform . . . 59
5.2.3 Signal Reconstructed by Discrete Wavelet Transform . . . 60
5.2.4 Comparison with Measurements of Respiration Belt . . . 61
5.3 Apnea Detection Results . . . 64
5.3.1 Apnea Detection Results for All the Experimental Data . . . 64
5.3.2 Apnea Detection Results for Different Sleeping Postures . . . 65
5.3.3 Apnea Detection Results Versus Existence of Blanket . . . 68
5.3.4 Results Versus Gender . . . 68
5.4 Non-ideality of Experiment . . . 69
5.4.1 Vibration of the Radar . . . 69
5.4.2 Participants holding breath for too long . . . 70
5.5 Results in Real Sleeping Scenario . . . 71
5.6 Validation With Real Patient's data . . . 73
5.6.1 Pre-processing of the Results . . . 73
5.6.2 Apnea Detection results . . . 76
5.6.3 Error Analysis . . . 78
5.7 Conclusion . . . 81

6 Conclusion and Future Work **83**
6.1 Conclusion . . . 83
6.2 Future Work . . . 84
References . . . 86

List of Figures

2.1 Motion of the chest cavity during one pulmonary ventilation cycle 10
2.2 Sketch of the cardiac cycle and circulation 11
2.3 Signal model for heartbeat, $f_h = 1.375Hz$, $A_h = 0.0005m$, $\tau = 0.05$, $f_{cut} = 1Hz$, $f_s = 262826.6667Hz$ 13
2.4 Signal model for respiration, $f_r = 0.25Hz$, $A_r = 0.005m$, $f_s = 262826.6667Hz$ 13
2.5 Combined signal model for respiration and heartbeat 13
2.6 Sketch of OSA physiology with obstruction of air flow to the lungs 14
2.7 OSA type1 signal model 14
2.8 OSA type2 signal model 15
2.9 OSA type3 signal model 15
2.10 Demonstration of CSA: (a)Sketch of CSA physiology with central nervous system failure (b) Signal model for CSA 16
2.11 Simplified block diagram of CW radar sensor and the mechanism of non-contact respiration detection based on the thorax/abdomen displacement . . 17
2.12 The basic principle of the FMCW radar with the sawtooth shape modulation:(a) the transmitted and received signal, (b) the corresponding beat frequency, and (c) the beat signal processing flow.[1] 21

3.1 Signal processing pipeline proposed in this thesis work 24
3.2 Results of phase extraction on simulation data: (a)normal respiration, without noise; (b) normal respiration, SNR=20 dB; (c) sleep apnea, without noise; (d) sleep apnea, SNR=20 dB 26
3.3 Range-Time plot of radar signal with noise added, SNR = 20dB 27
3.4 Results of spectrogram of simulation data: (a)normal respiration, without noise; (b) normal respiration, SNR=20 dB; (c) sleep apnea, without noise; (d) sleep apnea, SNR=20 dB 28
3.5 Third level filter bank block diagram representation of DWT 30
3.6 Characteristics of the Daubechies' extremal phase wavelet with 4 vanishing moments:(a) the four lowpass and highpass, decomposition and reconstruction filters associated db4 wavelet; (b) the scaling function and wavelet waveform. 31
3.7 DWT decomposition of radar signal containing respiration, SNR = 20 dB . 32
3.8 Results of envelope extraction on simulation data: (a)normal respiration, without noise; (b) sleep apnea, without noise 33
3.9 Results of signal smoothing by VMD: (a)normal respiration, without noise; (b) sleep apnea, without noise 37

3.10 Improvement of reconstructed signal after VMD when SNR = 3 dB: signal before VMD (a) normal breath (b) CSA (c) OSA, and signal after VMD (d) normal breath (e) CSA (f) OSA 38
3.11 Respiration rate estimation for modelled signal under SNR = 20dB with ground truth $f_{res\_true} = 0.35Hz$ 39
3.12 Demonstration of apnea detection based on threshold 40
3.13 Demonstration of SVM principle with support vectors and separation hyperplane 41

4.1 Confusion matrix for two-class classification problem. 45
4.2 Results of each step of the signal pre-processing workflow: after STFT (Doppler-time spectrogram pattern) with (a) central sleep apnea and (d) obstructive sleep apnea, after envelope extraction (Doppler frequency vs time pattern) with (b) central sleep apnea and (e) obstructive sleep apnea, after VMD (Doppler frequency vs time pattern) with (c) central sleep apnea and (f) obstructive sleep apnea 47
4.3 RMSE of respiration frequency estimation as a function of SNR for wavelet-based vs phase extraction approaches 48
4.4 Evaluation metrics of Monte Carlo simulation on the environmental noise: (a) Accuracy (b) Precision (c) Recall (d) F1 Score 49
4.5 Ellipsoid geometry used to model human torso; target lies on the xOy plane along the y axis 50
4.6 Evaluation metrics of Monte Carlo simulation on the environmental noise in different sleeping posture: (a) Accuracy (b) Precision (c) Recall (d) F1 Score 51
4.7 Examples of detection errors, i.e. patterns that are incorrectly recognised by the classification algorithms: for SNR = 0 dB (a) normal breath (b) CSA (c) OSA, and for SNR = 3 dB (d) normal breath (e) CSA (f) OSA 52

5.1 Picture of the experimental setup with radar in the red circle; the subject is lying on his side 55
5.2 Phase demodulation results: normal breathing in supine position for phase demodulation with unwrap process (a) phase demodulation without unwrap process (c) and ground truth (e), and holding breath episode in supine position for phase demodulation with unwrap process (b) phase demodulation without unwrap process (d) and ground truth (f) 57
5.3 Phase demodulation results: normal breathing in side position for phase demodulation with unwrap process (a) phase demodulation without unwrap process (c) and ground truth (e), and holding breath episode in side position for phase demodulation with unwrap process (b) phase demodulation without unwrap process (d) and ground truth (f) 58
5.4 Spectrogram for: normal breath in supine position (a), holding breath episode in supine position (b), normal breath in side position (c) and holding breath episode in side position (d) 59
5.4 Wavelet decomposition (a) normal breath in supine position (b) apnea in supine position 61

5.5 Picture of the Go Direct Respiration Belt product 61
5.6 Waveform comparison radar vs reference respiration belt: normal breathing in side position for radar based on STFT (a) DWT (c) and for belt (e), and holding breath episode in prone position for radar based on STFT (b) DWT (d) and for belt (f) 62
5.7 Spectrum comparison radar vs reference respiration belt: normal breathing in side position for radar (a) and belt (c), and holding breath episode in prone position for radar (b) and belt (d) 63
5.8 Signal reconstructed for Target 2 in prone position: normal breathing in prone position without blanket (a) with a blanket (c), and holding breath episode in prone position without blanket (b) with a blanket (d) 66
5.9 Signal reconstructed for Target 6 in side position: holding breath episode in prone position without blanket (a) with a blanket (b) 67
5.10 Reconstructed signal for Target 1: normal breathing in supine position (a) side position (b) prone position (c) without blanket, and normal breathing in supine position (d) side position (e) and prone position with a blanket . . 68
5.11 Examples of the effects on signal processing caused by radar vibration: target in supine normal without blanket (a) supine apnea with a blanket (b) prone apnea without blanket (c) side normal without blanket(d) 69
5.12 Example of the effect that participant holding breath for too long: reconstructed signal (a) reconstructed zoomed in (b) 70
5.12 Typical examples of the measurement in sleeping scenario: (a) normal breath, (b) body movement during sleep and (c) possible sleep apnea 72
5.13 Phase information obtained by collaborators at Huai'an First People's Hospital, Jiangsu, China: an example of normal breath 73
5.14 Phase information obtained by Huai'an First People's Hospital, Jiangsu, China: example of sleep apnea 74
5.15 Reconstructed signal from spectrogram for real patient: (a) normal breath (b) sleep apnea episodes (with ground truth) 75
5.16 Reconstructed signal from DWT for real patient: (a) normal breath (b) sleep apnea episodes (with ground truth) 76
5.17 Error case for the result on real patient: Hypopnea 78
5.18 Error case for the result on real patient: Body movement 79
5.19 Error case for the result on real patient: Random case 80

List of Tables

1.1 Brief description and comparison of different vital signs monitoring technologies . . . 4
1.2 Brief Description of Radar-based Physiological Montoring Researches in Recent Years . . . 7
1.3 Table 1.2. (Continued) . . . 8

2.1 Comparison of Radar-Based Vital Signs Monitoring Systems . . . 23

4.1 Apnea Detection Results For 100 Simulated Subjects and 3 Classification Algorithms, SNR = 20dB . . . 46
4.2 Apnea Detection Results For 420 Simulated Subjects and 3 Classification Algorithms; Subjects are in supine position and SNR = 20dB . . . 48

5.1 Experimental Data Composition; Units in the table: number of data collection 55
5.2 Apnea Detection Results Based on Threshold For The Entire Experimental Dataset . . . 64
5.3 Apnea Detection Results For The Entire Experimental Dataset . . . 65
5.4 Apnea Detection Experimental Results for Different Positions . . . 66
5.5 Apnea Detection Results versus Blanket . . . 68
5.6 Apnea Detection Results versus Gender . . . 69
5.7 Apnea Detection Results for Real Patient's data versus Segment Duration (Threshold based) . . . 77
5.8 Apnea Detection Results for Real Patient's data versus Segment Duration (SVM Classifier) . . . 77
5.9 Apnea Detection Results for Real Patient's data - Different classifiers . . . 77
5.10 Apnea Detection Results for Real Patient's data with segment duration of 40s; record with the first hour removed . . . 79

1

THESIS INTRODUCTION AND LITERATURE REVIEW

Sleep apnea is a severe disorder that degrades sleep quality for those affected and has been found related to a variety of cardiovascular diseases. The clinical approach used to diagnose obstructive sleep apnea-hypopnea syndrome (OSAHS) is polysomnography (PSG). However, this requires several wires attached to the patient all night, which is very uncomfortable and stressful. For this reason, in this thesis, algorithms to provide sleep apnea detection using contactless radar systems are investigated.

1.1. BACKGROUND

Sleep apnea is a prevalent disease with a high incidence in the population, particularly among older people, and is related to several neurocognitive and cardiovascular diseases such as stroke, chronic heart failure (CHF), coronary artery disease, hypertension[2] and diabetes, which can be a significant burden on health systems[3]. Meanwhile, it can be present without significant symptoms; therefore, most potential patients remain undiagnosed and untreated. According to the research by dr. Adam V. Benjafield et al. in 2019[4], in typical developing countries such as China and Brazil, about 23.6% and 49.7% of the population suffers from OSAHS respectively; meanwhile, the prevalence remains very high even in some developed countries, at 33.2% and 49% in the United States and the Netherlands respectively. The number of adults aged 30-69 who suffer from various degrees of obstructive sleep apnea (OSA) is estimated to be more than 900 million worldwide [4], making it a potentially growing global problem in the coming years.

Based on current researches into nocturnal breathing disorders, there are three defined types of respiratory obstruction: obstructive sleep apnea (OSA), central sleep apnea (CSA), and mixed sleep apnea (MSA)[5]. OSA occurs when there is a physical blockage of the airway at the back of the throat. This obstruction can lead to temporary breathlessness. During sleep, the body's muscle tone is usually in a relaxed state. In the human pharynx, the respiratory tract is composed of collapsible soft tissue walls. During sleep, the soft tissues may collapse and block the airway, preventing airflow in and out, causing what is clinically defined as obstructive sleep apnea. When obstructive sleep apnea occurs, the bones and muscles controlled by the central nervous system continue to expand and contract periodically, but no airflow is inhaled or exhaled[6–8]. In contrast, CSA occurs because of a malfunction of the central nervous system, which prevents it from adequately controlling the bones and muscles involved in breathing, resulting in inadequate or absent lung ventilation. In this case, the volume of the chest cavity no longer changes in response to the breathing process[9, 10]. It is referred to as mixed sleep apnea or complex sleep apnea when a person suffers from OSA and CSA simultaneously[11].

At present, the standard method for clinical diagnosis of sleep apnea is polysomnography (PSG), which requires patients to be monitored overnight in a hospital under the supervision of medical professionals to measure multiple physiological signals, including electroencephalography (EEG), electrooculography (EOG), electromyography (EMG) and electrocardiography (ECG). Many potential patients, however, consider this procedure invasive and uncomfortable. Therefore, although the PSG system offers good quality and durability, it is not the most suitable option for long-term continuous monitoring use and especially not for home use. Thus there is a high demand for alternative diagnostic technology. Several other technologies have been proposed in recent decades, such as actigraphy, acoustic sensor, camera, and their description and comparison of advantages and disadvantages will be developed in detail in section 1.3.

1.2. CONTRIBUTION OF THE RESEARCH

The main contributions of the research described in this thesis are summarized as follows:

- Proposed a signal processing pipeline involving spectrogram envelope extraction based on image processing and signal smoothing (specifically VMD, Variational Mode Decomposition) algorithms.

- Developed a simulation tool that allows Monte Carlo generation of synthetic data from multiple subjects and models beyond simple sines the vital signs as well as different types of sleep apnea. Moreover, the sleep position is taken into account.

- Validated the proposed algorithms on experimental data, with a comparison with the state of the art. Furthermore, possible improvements to state of the art algorithms such as those by T. Koda[12] have been proposed and validated.

- The potential of the system for more practical applications is confirmed by providing an example of monitoring a more extended recording of respiration in natural conditions in a home bedroom. Furthermore, the system was applied to radar data obtained from actual patients and achieved classification accuracies of upwards of 80%, demonstrating the potential of the developed system for clinical applications.

- The research work developed as part of this thesis has been submitted as a conference paper entitled "An Approach for Sleep Apnea Detection based on Radar Spectrogram Envelopes" for the European Microwave Week 2021, London, UK.

1.3. OVERVIEW OF VITAL SIGNS MONITORING TECHNOLOGIES

Many researchers are devoted to investigating new technologies that could reduce the manual involvement and improve the monitoring experience. Many portable and wearable devices which could accurately capture vital signals such as heart rate, breathing rate, blood pressure, oxygen saturation (SaO_2). have been developed. However, even though they are often small, non-invasive and comfortable to wear, they still have to be connected to the skin via electrodes, which might affect some of the physiological signals.

Besides, several kinds of non-contact sensors have been applied in many studies, including acoustic sensors, passive infrared (PIR) sensors and lidar. The description and comparison among these vital signs monitoring technologies are shown in Table 1.1. Contactless sensors can obtain respiratory, heartbeat or temperature information, but electrophysiological signals and blood oxygen saturation are often beyond their reliable detection capabilities. This trade-off allows them to be employed in a variety of applications.

Each of the listed mechanisms for contactless breath detection also has its own advantages. Camera-based and infrared sensors are particularly suitable for instantaneous monitoring over long periods of time. Lidar has merits of high resolution, high resistance to active interference, small size and lightweight. Radar and ultrasound sensor share the same advantages of environment independence and no perception of the subject, while radar is the one at relatively lower cost and more acceptable accuracy. Thus in this study, the focus is on radar-based monitoring. Some researchers are also working on developing the system with a combination of multiple sensors and conducting multi-sensor fusion, which could be a direction for future research of this study. Studies have pointed out that at 2.4 GHz and above, more than half of the incident power will be reflected back at the skin surface, which contributes to the most significant source of reflected power. Therefore, in practice, one can default to Doppler radar vital signs detection as displacement measurements of the skin surface[13].

This thesis work aims to perform sleep breathing disorder identification. The algorithm was based on the amplitude information of the breathing signal, so only respiration was studied in detail among the different vital signs, and the focus was on radar technology rather than on all the possible sensors.

1.4. RADAR - BASED SLEEP APNEA DETECTION: STATE OF ART

In this section, a comprehensive review of the current state of radar-based sleep monitoring technology will be provided, including a review of types of the radar system, signal processing methodologies and types of classification and features. For each type of radar application, the latest technologies and achievements, as well as the challenges faced, are presented in relation to the corresponding literature.

In recent decades, quantitative studies on radar-based sleep monitoring and apnea detection have been done. The most widely used systems are single-tone continuous wave (CW) radar [24–26], frequency-modulated continuous-wave (FMCW) radar [27–29] and Ultra Wide Band (UWB) radar [30][31]. Doppler CW radar, with its simple topology and

Table 1.1: Brief description and comparison of different vital signs monitoring technologies

Sensing Technology	**Contact or not**	**Description**	**Advantage**	**Disadvantage**
Actigraphy[14–17]	✓	A wearable device that measures movements by an accelerometer and estimate blood pressure using PhotoPlethysmoGraphy	1. Documents sleep at home 2. Objective, long-term record 3. Small size and light weight	Limited usefulness in assessment of SOL and diagnosis of sleep disorders
Acoustic Sensor[18]	×	Record breathing and snoring signals during sleep for sleep assessment	1. Low cost 2. No perception of the subject	1. Sensitivity to surrounding movements 2. Indirect analysis of breath
Camera-Based[19]	×	Measure the cardiac pulse by detecting the pulse-induced subtle color changes of the human skin	1. Long-term continuous record 2. Cost-effective, easy to implement	1. Suffers from color distortion caused by parallax 2. Environment dependent
Passive Infrared Sensor[20]	×	Capture thorax movement or air temperature changes around the nose area	1. Non-invasive 2. Instantaneous recording	1. Must use more one sensor 2. Ideal measuring distance less than $50cm$
Pressure Sensor[21]	✓	Collects vital signs using ballistocardiogram (BCG) sensor that reflects torso mass movement (due to cardiovascular activity)	1. Simple installation 2. Accessibility (nonwearable)	1. Non-portable 2. Not easily applicable to different people
Laser[22][23]	×	Laser-based common carotid pulse measurement using Doppler effect	1.Immune to interference of radio reflection 2. Non-invasive	1. Affected by the presence of obscurants (eg. clothes) 2. High cost
Radar	×	Vital sign monitoring by measuring Doppler signature of skin surface displacement	1. Environment independent 2. Capability of penetrating obscurants	Sentivity to interference

low power consumption, is the most common type of application for vital sign monitoring. However, the lack of distance information limits its application in the field of multi-target detection. Meanwhile, FMCW and UWB radars retain distance awareness while detecting the movement of the target through the Doppler effect despite that they each have their limitations, with FMCW radar having high power consumption and phase noise, while UWB radars are not suitable for long-range measurements. While each of these three radars comes with its own advantages and disadvantages, in general, a number of studies have demonstrated their effectiveness in sleep monitoring applications.

Life signals are low-speed target signals with small Doppler shifts, weak echoes and easily drowned in the background of strong clutter. It is a low frequency, quasi-periodic, low signal-to-noise ratio, multi-harmonic combination signal that must be detected and extracted more accurately and effectively by effective signal processing. The classical approach of retrieving vital signs from the radar data is based on phase processing. Both traditional arctangent demodulation [32][33] and differentiate and cross multiply (DACM) [27][30] algorithms have been investigated and implemented in many pieces of research. However, the signal phase is easily affected by noise; thus, alternative signal processing methods in the spectral domain are also explored. Signal processing approaches such as FFT [34][35], continuous wavelet transform (CWT) [36], multiple signal classification (MUSIC) [24][37], relaxation (RELAX) [24], atomic norm minimization (ANM) [37] amongst others, have been verified to provide sufficient accuracy for vital sign signal spectrum estimation.

Furthermore, separating the respiratory or heartbeat signals is a signal processing challenge. The energy of the collected respiratory signal is much greater than that of the heartbeat signal, and the higher harmonics of the respiratory signal cause surface micro-movements to overlap with those caused by the heartbeat, and the spectral overlap of the corresponding signals can make it difficult to isolate the heartbeat signal from the respiratory signal. In recent years, various algorithms have emerged for the separation of heartbeat, and respiratory signals, such as the minimum mean square error cost function method, which first estimates the complex coefficients of each harmonic and subtracts the harmonic signal from the mixed-signal containing the heartbeat and respiratory harmonics to obtain the desired signal[35]. Empirical modal decomposition is applied to decompose the radar signal into a finite number of intrinsic modal functions, and then the IMF component, which reflects the structural characteristics of the vital signal, is used to recover the respiratory and heartbeat signals independently in the time domain to avoid the interference of the respiratory harmonics with the heartbeat signal[27, 36]. In 2011, the University of Trento, Italy, applied the independent component analysis (ICA) algorithm to distinguish between noise and clutter and successfully extracted respiratory and heartbeat signals[38].

Several algorithms have been proposed that implement non-contact apnoea detection based on energy spectroscopy. The most widely used is to judge the constructed respiratory signal according to a threshold based on the strength characteristics of the normal respiratory signal and the signal when apnea occurs. Machine and deep learning algorithms are also extensively used in breath pattern classification. An approach using a Support Vector Machine (SVM) on features extracted from the spectrogram is proposed in [12] and applied to experimental data measured on two patients suffering from sleep apnea. They obtained an accuracy of 79.2% and 79.5% for OSA and CSA, respectively. A hybrid CNN-LSTM network that could provide real-time apnea detection with an accuracy over 90% based on UWB radar is presented in this recent work [39].

Some selected publications studying radar-based vital signs monitoring as well as their brief description are listed in Table 1.2 and its continued Table 1.3.

It is worth noticing that the achievement of radar-based vital signs monitoring in most studies is based on the test subject sitting or lying on his back, facing straight to the radar and remaining stationary, which deviates from the actual sleep situation. There is still much space to explore the complexity of the sleep environment, such as random body motions, different sleeping positions, body orientation and harmonics of vital signs. In addition, attention can be given to the radar-based detection for other physiological signals that may aid in the detection of respiratory obstruction such as pulse pressure, tidal volume, minute ventilation and air flow[40].

In terms of signal processing algorithm optimization, inverse tangent demodulation, time-frequency analysis, adaptive DC calibration, noise and clutter cancellation are still the focus of future research focus; blind source separation (BSS) signal processing techniques will increasingly be used to distinguish between ward environment clutter and interference caused by multiple targets and unconscious body movement. The need for algorithms to monitor the human body's vital signals in motion has also been addressed; more clinically relevant evaluation metrics for medical surveillance radar have yet to be proposed. More clinically relevant evaluation metrics for medical surveillance radar are yet to be proposed.

Based on this summary of state of the art, this thesis research focused on the gaps of methods to identify the respiration signal based on the envelopes of spectrograms and simple machine learning classifiers. These have been extensively validated with simulations and experimental data with 14 volunteers as well as actual patients.

1.5. STRUCTURE OF THE THESIS

The rest of the thesis is organized as follows. The physiology of the respiration system and heart and three types of sleep apnea, as well as their corresponding mathematical models, is presented in Chapter 2. Furthermore, the architecture and principle of Doppler radar are also explored in this chapter. The pipeline of signal processing and breathing pattern classification algorithm is described in Chapter 3. Chapter 4 and Chapter 5 presents the procedure and results of simulation and experimental validation respectively, while Chapter 6 concludes the thesis.

Table 1.2: Brief Description of Radar-based Physiological Montoring Researches in Recent Years

Reference	**Type of radar**	**Signal Processing Algorithm**	**Experiment Set-up**	**Results**
C. Li et al.[41]	4- to 7-GHz broadband portable radar	Spectral estimation by RELAX algorithm	Subject seating still on a chair in a laboratory environment	Identification and estimation of the heartbeat and respiration rates
J. Li et al.[42]	2.4GHz UWB Radar	Clutter cancellation by CT Noise reduction by SVD Spectral analysis by FFT&RGK	Subject face to the wall sitting 1.5m away from radar	Through wall radar detection Vital signs frequency estimation
L. Sun et al.[37]	2.475GHz CW Radar	Vital signs frequency estimation by StANM	Subject seating 2m away from the antenna	Accurately extract heartbeat and respiration
X. Hu et al.[36]	IR-UWB Radar	Noise reduction by EEMD Vital sign separation by CWT	Healthy male sitting in a chair at a distance of around 0.3m	Well separate the vital signs
J. Kernec et al.[24]	2.4GHz CW Radar	Frequency estimation by SST, MUSIC, RELAX, StANM Sleep stage estimation by ML	Patients in Nanjing Chest hospital people in controlled position	Accurate spectral estimation Sleep stage classification with accuracy about 80%
L. Sun et al.[43]	77GHz FMCW Radar	2-D Phase Accumulation Vital sign separation by EEMD Frequency estimation by MUSIC	Subject seating 1.5m away from the radar	Distinguish the heartbeat component from respiration Accurately estimate the heart rate
M.Kagawa et al.[44]	77GHz FMCW Radar	Body Movement Cancellation by Automatic Gain Control Heart rate extration by Spectrum Shape Analysis	Two radar were used to measure the vibrations of the chest and the abdomen of 31 elderly outpatients in hospital	Identify 3 types of sleep apnea with accuracy about 90%
A. Javaid et al.[45]	IR-UWB Radar	Signal extraction by 20 tap triangular filter Motion Detection by thresholds Classification by Linear Discriminant classifier	Over 1,200 60-second epochs collected from 4 subjects	Apnea classification accuracy of 73%

Table 1.3: Table 1.2. (Continued)

Reference	Type of radar	Signal Processing Algorithm	Experiment Set-up	Results
N. Du et al.[33]	24GHz CW Radar	Phase extraction by acrtangent demodulation Vital sign separation by BPF Classification by drop in amlitude	Whole night monitoring on a volunteer with diagnosed sleep apnea at home	Apnea classification accuracy of 92%
M. Baboli et al.[32]	2.4 GHz and 24GHz quadrature radar	Phase extraction by acrtangent demodulation Classification by detecting drop in amplitude or an increase in area and a drop in length of the I/Q arc	Patient lying in supine position, radar placed 1 m above the chest	83% sensitivity and 90% specificity in apnea detection
J. Xiong et al.[46]	2.4 GHz CW Radar	Residual comparison algorithm Classification by drop in amlitude	Whole night monitoring on male patient with diagnosed snoring and emphysema pulmonum	Apnea detection accuracy of 86%
C. Wang et al.[34]	UWB Radar	Filter by FFT Feature extraction by Principal Component Analysis (PCA) Classification by ML	100-minutes monitoring on five healthy person	66% sensitivity and 98% specificity in apnea detection
T. Koda et al.[12]	24GHz CW Radar	Preprocessing by STFT Classification by SVM	7-hour monitoring on 2 patients	Apnea detection accuracy of 79%
H. Kown et al.[39]	IR-UWB Radar	Range-Time plot using FFT Classification by CNN-LSTM	Experiments on volunteers who were considered as a part of the high-risk group	Real time apnea classification with accuracy over 90%
E. Antolinos et al.[27]	FMCW Radar at 122GHz	Phase extraction by DACM Artifacts removement by EMD	A 22-year-male lying down and holding breath to simulate apnea	Extract the respiratory and heart-beat rates Obtained the heart rate variability (HRV) sequence

2

Signal Models And Radar System for Sleep Apnea Detection

This chapter describes the physiology of the respiration system and heart and proposes mathematical models of chest wall motion induced by cardiopulmonary activity. Then the pathology and clinical classification of sleep apnea, including their idealized models, is introduced. At the end of this chapter, the radar system's principles, especially those commonly used in vital sign monitoring applications, such as continuous wave radar, frequency-modulated continuous wave radar, and ultra wide band radar, are discussed.

2.1. Signal Models For Respiration And Heartbeat

2.1.1. Physiology Motion Of Respiration And Heart System

Respiratory System

The most fundamental function of the human respiratory system is to complete the gas exchange, that is, to diffuse oxygen into the capillaries at the blood-gas barrier and to liberate carbon dioxide from the capillaries into the alveoli to be exhaled. This gas exchange process is completed during every pulmonary ventilation cycle. Pulmonary ventilation is induced by alterations in the volume and atmospheric pressure of the chest cavity. This process is accompanied by air circulation through the respiratory tract, where the air is drawn into the body through the mouth and nose, then sequentially through the pharynx, larynx and trachea into the lungs, where it is oxygenated and then exhaled in the reverse direction—during normal inhalation, the diaphragm and external intercostal muscles contract, allowing the thoracic cavity to expand and air to rush into the lungs. During normal exhalation, the muscles relax, inducing the chest cavity to contract and the air pressure to rise, which allows the air to expel. As demonstrated in Figure. 2.1, the expansion and contraction of the chest cavity cause distinct displacements on the surface of the skin, which can

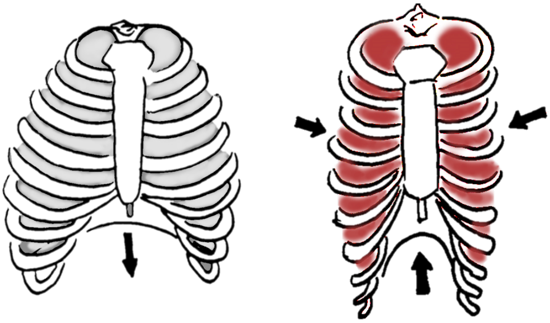

Figure 2.1: Motion of the chest cavity during one pulmonary ventilation cycle

be captured by radar, allowing non-contact measurement of respiration.

Many researchers have done quantitative studies on the motion of the chest wall during breathing. DeGroote et al.[47] marked 36 points by using the projection of a grid on the body and measured the movement of the chest in all directions. The largest movement occurs at the sternum and the navel, with the displacement 4.3 and 4.03 mm, respectively. Kondo et al.[48] studied the relationship between tidal volume and displacement of the abdomen. The results showed that the maximum displacement of the abdominal wall reached 12mm (with more than 1100 mL inspiration). In conclusion, thorax motion is different for every individual during a breathing cycle due to the difference in personal physiology and pulmonary ventilation volume. Statistically, the fundamental frequency of the respiratory signal falls in the interval of 0.1 to 0.7 Hz (6 to 42 bpm), and the amplitude of the chest wall ranges from 4 to 12 mm[48].

Heart System

The heart plays a pivotal role in the circulatory system like a pump, delivering a constant blood flow to the entire body. The left side of the heart pumps arterial blood, which carries oxygen and nutrients to the tissues and organs, while the right side pumps blood saturated with metabolic waste like CO_2 to the lungs. The demonstration of one cardiac cycle is shown in Figure. 2.2. In each cardiac cycle, the heart experiences contraction and relaxation. As the heart contracts to create the pressure that powers the blood flow, it shifts within the thoracic cavity, striking the chest wall and producing detectable displacement on the surface of the skin.

The fundamental frequency of the heartbeat signal lies between 0.9 Hz and 3 Hz (54 to 180 bpm) with an amplitude of approximately 0.5 mm[49].

The ranges of amplitude and frequency listed above are selected from the literature and will be used in subsequent simulations of respiratory and heartbeat signals. It is worth notice that these numbers do not necessarily describe the vital signatures of particular individuals in reality very precisely; however, a precise estimation of these quantities is not the scope of this thesis; the models built in the following sections will still hold even if those numbers are slightly changed.

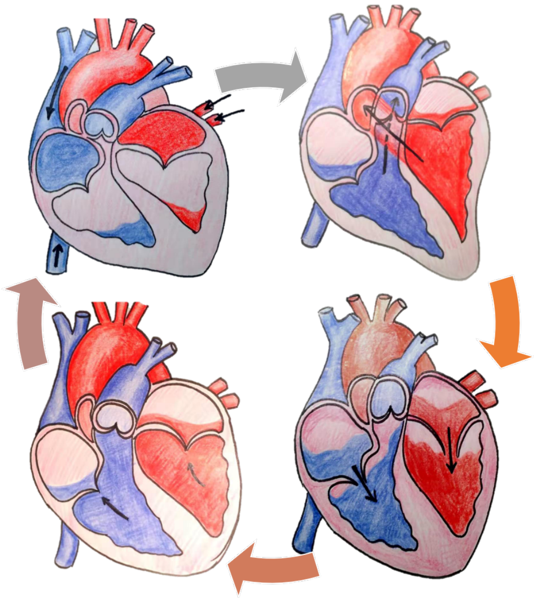

Figure 2.2: Sketch of the cardiac cycle and circulation

2.1.2. Signal Model for Cardiopulmonary Activity

In this section, the development of a signal model demonstrating the movement of the thoracic/abdominal wall during normal breathing is presented. Based on this model, the simulation to study the signal processing techniques could be conducted.

The simplest and most commonly used modelling method uses two sinusoidal signals with different amplitudes and frequencies to simulate the displacement at skin surface caused by respiration and heartbeat, respectively. This method is employed by many researchers due to its simplicity[50]. With known amplitude and frequency of breathing and heartbeat, skin surface displacement could be modelled as:

$$x(t) = A_r \sin\left(2\pi f_r t\right) + A_h \sin\left(2\pi f_h t\right) \tag{2.1}$$

where A_r, f_r represent the amplitude and frequency of respiration, respectively, and A_h, f_h represent the amplitude and frequency of heartbeat respectively.

However, in reality, the displacement of the chest wall caused by respiration and heartbeat is much more complicated than sinusoidal signals. Many researchers have studied how to model respiration and heartbeat authentically. In 2008, Dennis R. Morgan et al. found that it is more accurate to model the waveform of breathing with a higher-order sinusoidal signal[35]. They also pointed out that the signal model they developed was not intended as a rigorous physiological model. It was still a highly idealized model of skin-surface movement. However, it could provide sufficient precision for capturing the essence of vital signs and verifying the signal processing techniques. The movement of chest-wall can be expressed as:

$$x(n) = x_h(n) + x_r(n) \tag{2.2}$$

where $x_h(n)$ and $x_r(n)$ are the contribution of cardiac and respiratory component, respectively.

The heartbeat can be constructed by periodically repeating the prototype analog pulse p_h (t)[35]. The exponential $e^{-t/\tau}$ is used to approximate the pulse signal, where τ is the time constant. The pulse signal is filtered by a second-order Butterworth filter which has f_{cut} as its cutoff frequency. This model conceptualizes a cardiac cycle. During the isovolumic systole, the ventricles continue to contract. As the pressure in the ventricle continues to rise, exceeding the pressure of the aorta and pulmonary arteries, the heart valves open. The blood will be quickly injected into the artery, producing a short impulse movement which is eventually sensed by the thorax/abdomen wall through the filtering of bones and tissue. The characteristic pulse shape can be derived by taking inverse Laplace transform of the product of impulse response of the exponential, after which a Butterworth filter is applied, and the result is as follow:

$$p_h(t) = e^{-t/\tau} + \left[\left(\frac{\sqrt{2}}{\omega_{cut}\tau} - 1 \right) \sin\left(\frac{\omega_{cut} t}{\sqrt{2}} \right) - \cos\left(\frac{\omega_{cut} t}{\sqrt{2}} \right) \right] e^{-\omega_{cut} t/\sqrt{2}} \tag{2.3}$$

where $\omega_{cut} = 2\pi f_{cut}$. We then repeat p_h periodically at frequency f_h to construct the heartbeat signal. After sampling at frequency f_s, the discrete-time motion could be obtained:

$$x_h(n) = p_h\left(\frac{n}{f_s} - \left\lfloor \frac{n}{f_s} f_h \right\rfloor \cdot \frac{1}{f_h} \right) \tag{2.4}$$

where $\lfloor x \rfloor$ is the floor function. Then the discrete-time signal component should be scaled to the amplitude A_h. The improved heartbeat model is shown in Figure 2.3, where the amplitude and frequency of heartbeat are set to be 5×10^{-4}m and 0.25Hz, respectively. In section 2.1.1, a range of values for the frequency and amplitude of the cardiopulmonary signal was introduced; here, a value typical within this interval is chosen. This particular value was taken to give an example of the signal waveform, and the proposed model remains valid for other values in the range.

The improved respiration signal model can be defined by a half-cycle kth order sinusoidal function:

$$p_r(t) = \sin^k \pi f_r t, 0 \le t \le \frac{1}{f_r} \tag{2.5}$$

The exponent k controls the rounding of the cusp as well as the general shape. In a similar approach, we get the expression of discrete-time respiration signal model:

$$x_r(n) = p_r\left(\frac{n}{f_s} - \left| \frac{n}{f_s} f_r \right| \cdot \frac{1}{f_r} \right) \tag{2.6}$$

where f_r and f_s represent the respiration frequency and sample frequency, respectively. Then we scaled it to amplitude A_r. The waveform of this respiration model is shown in Figure 2.4:

The movement of the chest wall can be modelled as the superposition of the heartbeat and respiration signal, the waveform is shown in the Figure. 2.5 below:

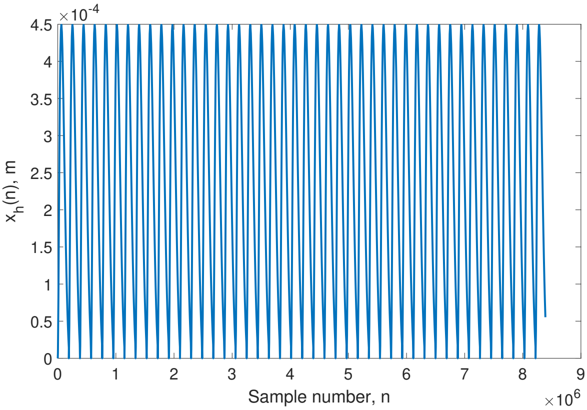

Figure 2.3: Signal model for heartbeat, $f_h = 1.375Hz$, $A_h = 0.0005m$, $\tau = 0.05$, $f_{cut} = 1Hz$, $f_s = 262826.6667Hz$

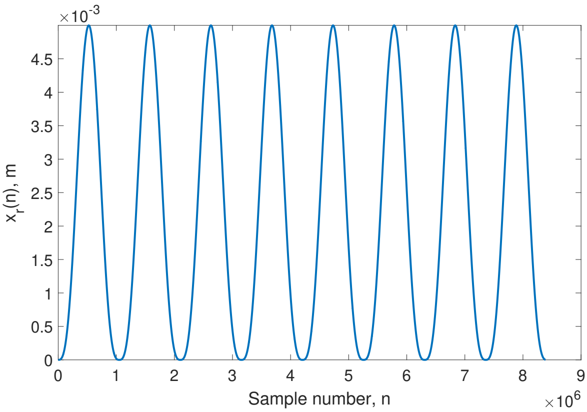

Figure 2.4: Signal model for respiration, $f_r = 0.25Hz$, $A_r = 0.005m$, $f_s = 262826.6667Hz$

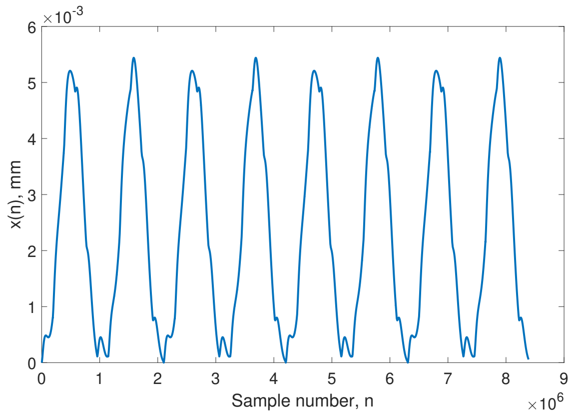

Figure 2.5: Combined signal model for respiration and heartbeat

2.2. SIGNAL MODELS FOR DIFFERENT TYPES OF APNEA

As demonstrated in the previous chapter, clinically, there are three types of sleep apnea: OSA, CSA and MSA. This section will introduce the pathological characteristics of these three types of sleep apnea and develop an appropriate model for each of them.

2.2.1. OBSTRUCTIVE SLEEP APNEA

OSA is caused by repetitive bouts of upper airway obstruction during sleep due to the narrowing of respiratory passages[51]. This kind of block causes temporary cessation of respiration. Patients usually suffer from snoring and awakening from sleep with a feeling of suffocation because their nasopharynx is blocked. The schematic diagram of physiological characteristics of OSA is shown in Figure. 2.6.

When OSA occurs, the nerve centre still gives instructions to the bones and muscles, controlling them to maintain breathing. In this case, the undulation of the chest wall and abdomen will be maintained; however, since there is no air coming in through the nose and mouth, the pulmonary ventilation volume is reduced significantly, resulting in subnormal chest displacement. Sometimes, due to the shortage of oxygen, the frequency of respiration will increase under the control of the brain. The amount of reduction in the amplitude of chest motion and the change in respiratory rate vary from person to person.

It is assumed that when respiratory obstruction occurs, the waveform of the respiration remains unchanged; only the amplitude and frequency are affected. On the other hand, the impact of respiratory obstruction on the heartbeat is negligible. Based on the vital sign models derived in the previous section, in subsequent simulations, the following models are used to simulate OSA[52]:

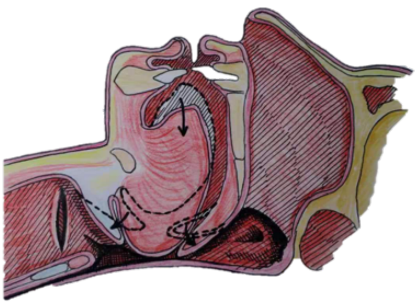

Figure 2.6: Sketch of OSA physiology with obstruction of air flow to the lungs

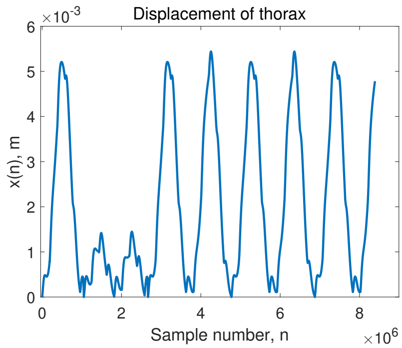

Figure 2.7: OSA type1 signal model

1. As shown in Figure. 2.7, the amplitude values of respiratory activity decreasing, $A_r^{'} = 0.2 \times A_r$ and the respiratory frequency accelerating, $f_r^{'} = 1.3 \times f_r$.
2. The frequency of the breathing activity is constant, but the amplitude is diminished by more than 50%, $A_r^{'} = 0.5 \times A_r$, as demonstrated in Figure. 2.8;

3. The amplitude and frequency of respiratory activity are of fluctuating nature. The model of this type of OSA is shown in Figure. 2.9. The frequency of the three respiratory cycles during obstructive sleep apnea is 1.5, 1.8 and 2.2 times that of normal breathing, with amplitudes of 0.18, 0.19 and 0.2 times respectively.

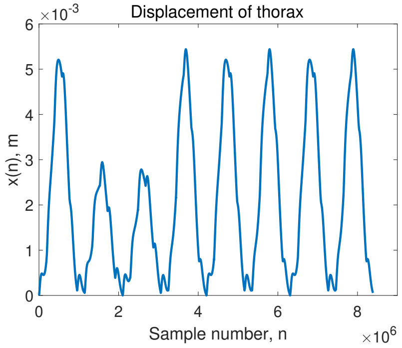

Figure 2.8: OSA type2 signal model

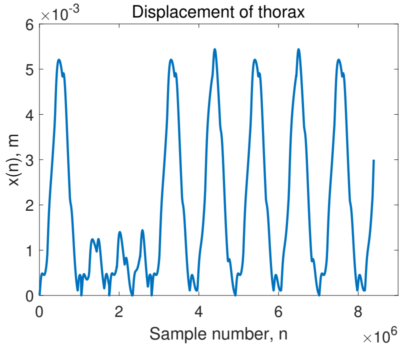

Figure 2.9: OSA type3 signal model

It is worth noting that all three of the above mathematical models of respiratory obstruction are based on the following assumptions:

- At the level of mathematical modelling, the envelope shape of the respiratory signal remains unchanged when OSA occurs, which means Equation 2.5 and 2.6 are still used to simulate breathing during respiratory obstruction, except that the two parameters of respiratory amplitude and frequency are changed.

- When OSA occurs, the heartbeat signal is assumed to be completely unaffected by the respiratory obstruction, and the waveform remains consistent, whose mathematical model is described by Equation 2.3 and 2.4. However, there is also a coupling between the heartbeat signal and the respiratory obstruction, but since their correlation has not been studied thoroughly and precisely, and since the amplitude of the heartbeat signal is very weak compared to that of respiration, the variance of heartbeat is ignored here.

- For reasons of simplicity, the proportional decrease in respiratory amplitude at the occurrence of OSA, as well as the increase in frequency, is chosen as a typical value in the interval given by the model, in order to give a visual example of the three different types of OSA. The results of the whole modelling and simulation still hold when other values are taken.

2.2.2. Central Sleep Apnea

Compared to OSA, CSA is rarer in the population but also more severe. One specific type of central sleep apnea, also called the Ondine curse, often happens in neonates, which can be fatal. CSA occurs because the part of the brain stem that controls breathing behaviour operates abnormally. In central sleep apnea, the brain stem shows less sensitivity to changes in the level of carbon dioxide in the blood. Thus, muscles involved in respiration are not excited by the signal from the brain, which causes the displacement of the chest wall due to breathing. As the change in chest volume due to breathing disappears when CSA occurs, the chest wall no longer undulates due to breathing, but the displacement caused by the heartbeat remains[9]. At the level of the equation expression, as shown in Equation 2.2, the second term vanishes and only the component of the heartbeat represented by the first term is retained. The model of the heartbeat is still described by Equation 2.3 and 2.4. The pathological demonstration and the signal model of CSA are shown in Figure. 2.10, the motion of the thorax is merely associated with the heartbeat.

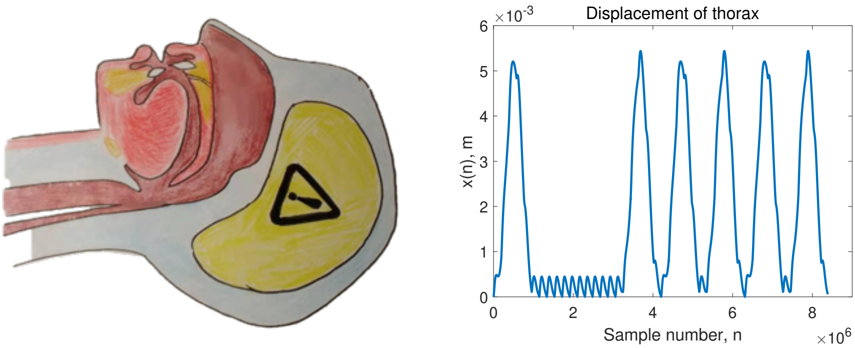

(a) Physiology of CSA

(b) Signal model for CSA

Figure 2.10: Demonstration of CSA: (a)Sketch of CSA physiology with central nervous system failure (b) Signal model for CSA

2.2.3. Mixed Sleep Apnea

When OSA and CSA occur at the same time, it is medically defined as mixed sleep apnea(MSA). The exact mechanism of the failure of the central respiratory controller in mixed sleep apnea remains unknown. The inducement and manifestation of MSA are very complex and have not been thoroughly studied. Typically, this type of apnea is detected when treating OSA with continuous positive airway pressure, and central sleep apnea emerges. Therefore, an additional model of MSA is omitted in this research.

2.3. Radar System For Sleep Apnea Detection

As discussed in previous sections, the breathing and heartbeat of living organisms cause chest wall movement, which can be captured by the radar. The electromagnetic wave emitted by the radar is reflected by the chest wall, and the reflected wave carries the information of the heartbeat and breathing of the monitored object. The vital signs can be well extracted by conducting appropriate signal processing algorithms. The signal processing techniques for different radars are distinctive. In the field of vital sign monitoring, researchers generally use three types of radars: CW (Continuous-Wave) Doppler radar, FMCW (Frequency-Modulated Continuous-Wave) radar and UWB (Ultra Wide-Band) radar. This section presents a summary of the models of these radars and the comparison between them.

2.3.1. Continuous Wave Radar

Doppler CW radar detects vital signs based on the Doppler effect of moving objects. It emits a continuous single frequency sinusoidal wave signal and simultaneously continuously receives reflected wave. The movement of the skin surface causes the Doppler effect, which is equivalent to phase modulation of the incident wave. The vital signs could be constructed by performing phase demodulation of the reflected signal in the receiver end. Figure. 2.11 demonstrates a typical structure of Doppler CW radar, in which synchronous demodulation is applied, that is, the local oscillator signal of the receiver is directly taken from the transmitter.

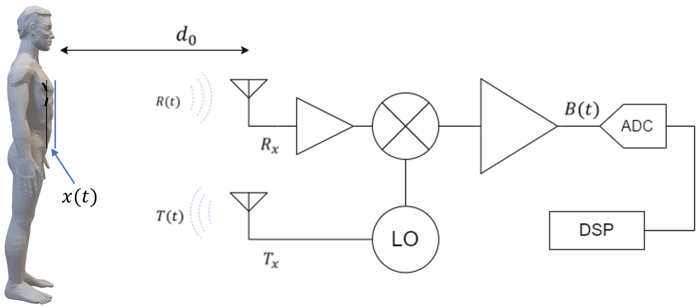

Figure 2.11: Simplified block diagram of CW radar sensor and the mechanism of non-contact respiration detection based on the thorax/abdomen displacement

In the transmitter, the transmitted signal is generated by frequency synthesizer and can be represented as:

$$s_t(t) = A_t \cos\left(2\pi f_c t + \Phi(t)\right) \tag{2.7}$$

where f_c represents the carrier frequency, A_t represents the amplitude of the transmitted signal and $\Phi(t)$ is the phase noise.

Assume the movement of the thorax is $x(t)$ and the initial distance between the radar and the thorax is d_0. Thus, the distance between the transmitter and chest wall can be represented as:

$$d(t) = d_0 + x(t) \tag{2.8}$$

For CW radar, the distance between the transmitter and the chest will induce a round trip time delay, which is:

$$t_d = \frac{2d(t)}{c} = \frac{2(d_0 + x(t))}{c} \tag{2.9}$$

where c is the light speed. Therefore, the received signal can be considered as a scaled replication of the transmitted signal with a time delay:

$$s_r(t) = s_t(t - t_d) \tag{2.10}$$

$$= A_r \cos\left[2\pi f_c (t - t_d) + \Phi(t - t_d) + \theta_0\right] \tag{2.11}$$

where θ_0 is the phase shift induced by variety of factors. Substitute eq. 2.8 and eq. 2.9 into eq. 2.11, the following equation could be obtained:

$$s_r(t) = A_r \cos\left[2\pi f_c t - \frac{4\pi d_0}{\lambda} - \frac{4\pi x(t)}{\lambda} + \Phi\left(t - \frac{2d_0}{c}\right) + \theta_0\right] \tag{2.12}$$

$$= A_r \cos\left[2\pi f_c \left(t - \frac{2d(t)}{c}\right) + \Phi\left(t - \frac{2d(t)}{c}\right) + \theta_0\right] \tag{2.13}$$

By mixing the received signal with the local oscillator $s_{LO}(t) = \cos\left[2\pi f_c t + \Phi(t)\right]$ we can obtain the beat signal:

$$s_b \approx A_b \cos\left[2\pi f_{IF} t + \theta + \frac{4\pi x(t)}{\lambda} + \Delta\Phi(t)\right] \tag{2.14}$$

similarly, A_b represents the amplitude while $\Delta\Phi(t) = \Phi(t) - \Phi\left(t - \frac{2d_0}{c}\right)$ is the residual phase noise. $\theta = \frac{4\pi d_0}{\lambda} - \theta_0$ is the phase shift related to the initial location of the target. Then the signal is filtered by a low-pass filter, which results in a simplified signal component:

$$s_b = A_b \cos\left[\frac{4\pi x(t)}{\lambda} + \theta + \Delta\Phi(t)\right] \tag{2.15}$$

After sampling by the ADC module, the analog signal is converted to a time discrete form:

$$s_b(n) = A_b \cos\left[\frac{4\pi x(nT)}{\lambda} + \theta + \Delta\Phi(nT)\right] \tag{2.16}$$

Doppler CW radar uses phase demodulation to extract vital sign information with high accuracy[53][54]. When the Doppler radar uses a single-channel structure, the first-order expansion of eq. 2.16 is generally used to approximate the phase. However, we generally will encounter a problem of null detection point, that is, when the target locates at some specific positions, the eq. 2.16 has a zero value differential, which results in a significant detection error. In this case, a quadrature receiver is commonly used to avoid this problem. The output of the I/Q component is shown as follows:

$$I(n) = A_I \cos\left[\frac{4\pi x(n)}{\lambda} + \theta + \Delta\Phi(n)\right] \tag{2.17}$$

$$Q(n) = A_Q \sin\left[\frac{4\pi x(n)}{\lambda} + \theta + \Delta\Phi(n)\right] \tag{2.18}$$

The phase history that contains range information of the target is extracted by conducting the arctangent transformation:

$$\Phi_{his}(t) = \arctan\left(\frac{Q(t) - b}{I(t) - a}\right) + \frac{k\pi}{2} \tag{2.19}$$

$$= \frac{4\pi x(n)}{\lambda} + \theta + \Delta\Phi(n) \tag{2.20}$$

where a and b denote the dc offsets in I and Q channels.

2.3.2. ULTRA WIDE BAND RADAR

UWB pulse radar is one of the most commonly used vital signs detection radar. It continuously emits periodic electromagnetic pulses, whose pulse width are generally below one nanosecond. The pulses will be reflected back by the object and then be captured by the receive antenna. Similar to the CW radar, the information of chest wall motion is modulated into the reflected electromagnetic wave. Ultra wide band refers to an instantaneous fractional energy bandwidth greater than about 0.2-0.25[55, 56]. The relative large bandwidth of UWB radar leads to a considerably high range resolution, which helps it distinguish and eliminate most of the multipath interference. The good performance of UWB radar in range resolution makes it eminently suitable for the detection of small signals such as heartbeat and breathing. Unlike CW radar, UWB radar is also very applicable for multi-target detection because the echoes contain distance information. IR-UWB radar is characterised by robustness in noisy environments, accurate positioning to the centimetre level, low power consumption[57] and good object penetration[58], which contributes to it being widely used in many fields[59–62].

Assume the distance between the object and antenna is $d(t)$, then the round trip time lag is $\tau_d(t) = \frac{2d(t)}{c}$. Based on the time delay, the position of the object is determined. The signal of interest at the receiver front end for IR-UWB radar is the convolution of transmitted pulse (with a carrier of frequency ν_c) and impulse response of vital signs $h(\tau,t)$ multiplied by the amplitude of collected pulse A[63]:

$$r(\tau,t) = s(\tau) * h(\tau,t) = A \cdot s(\tau - \tau_d(t)), \tag{2.21}$$

The output of I/Q branches and the corresponding complex pulse are described by:

$$I(\tau,t) = r(\tau,t) \cdot \cos(2\pi\nu_c\tau) \tag{2.22}$$

$$Q(\tau,t) = r(\tau,t) \cdot \sin(2\pi\nu_c\tau) \tag{2.23}$$

$$\begin{aligned} y(\tau,t) &= I(\tau,t) - Q(\tau,t) && (2.24)\\ &= r(\tau,t) \cdot \exp\left(-j2\pi\nu_c\tau\right) && (2.25) \end{aligned}$$

Then the FFT of $y(\tau,t)$ in fast-time and slow-time can be obtained, denoted respectively as $Y(\tau,\nu)$ and $Y\left(\tau,f\right)$. The received signals are sampled in fast time with ADC sampling period T_f and in slow time with pulse repetition interval T_s:

$$\boldsymbol{R}[n,k] = r\left(\tau = nT_f, t = kT_s\right), \quad k = 1,2,...,K, \quad n = 1,2,...,N. \tag{2.26}$$

where N and K denote the number of discrete time sequence in fast time and slow time domain, respectively. The chest wall displacement is contained in the Doppler information and range history for UWB radar can be acquired by selecting range cell r where the target is located:

$$R_{his}[k] = \boldsymbol{R}[r,k] \tag{2.27}$$

The phase information of UWB radar can be obtained along slow-time by performing FFT on each pulse:

$$\begin{aligned} Y(\nu,t) &= \left[A \cdot S(\nu)\exp\left(-j2\pi\nu\tau_d(t)\right)\right] * \delta(\nu+\nu_c)\\ &= A \cdot S(\nu+\nu_c)\exp\left[-j2\pi(\nu+\nu_c)\tau_d(t)\right] && (2.28) \end{aligned}$$

where $S(\nu)$ is the result of the FFT performed on transmitted pulse (τ, t) in τ. To get the FFT under minimal computation complexity, Equation 2.28 is computed at dc:

$$
\begin{aligned}
Y(0,t) &= \sum_{k} \left[I(\tau_k, t) - jQ(\tau_k, t) \right] \\
&= A \cdot S(\nu_c) \exp\left[-j2\pi\nu_c\tau_d(t) \right].
\end{aligned}
\tag{2.29}
$$

Phase history is then demodulated from the I/Q component of $Y(0,t)$:

$$
\Phi_{his}(t) = \arctan\left(\frac{M(t)}{R(t)}\right) + \frac{k\pi}{2} \tag{2.30}
$$

$$
= \frac{4\pi x(n)}{\lambda} + \Phi \tag{2.31}
$$

In which $M(t) = Imag[Y(0,t)]$ and $R(t) = Real[Y(0,t)]$. Phase history for the UWB radar is consistent with that for CW radar which is expressed by Equation 2.20, showing a linear relationship between time delay.

Due to the extremely small pulse width, high accuracy can be achieved when calculating the target position over time. The range resolution of UWB radar is determined by -3dB bandwidth, which could be approximated by the inverse of pulse duration, $B = 1/\tau$. The Doppler resolution of pulse radar depends on main lobe width of an individual spectral line, which is inverse of coherent processing interval T_d according to principle of Fourier transform of finite long sequences, $\Delta f_d = 1/T_d$.

2.3.3. Frequency Modulated Continuous Wave Radar

Doppler CW radar is widely used in the field of vital signs detection because of its high accuracy, low power consumption and simple structure. However, using CW radar will lose the range information and multi-target discrimination ability. UWB radar can maintain robustness to multipath interference and cluttering while measuring the target position with high accuracy.

FMCW radar transmits frequency modulated continuous wave, which is also called chirp signal, as shown in Figure 2.12, The expression of chirp signal can be written as[53][54]:

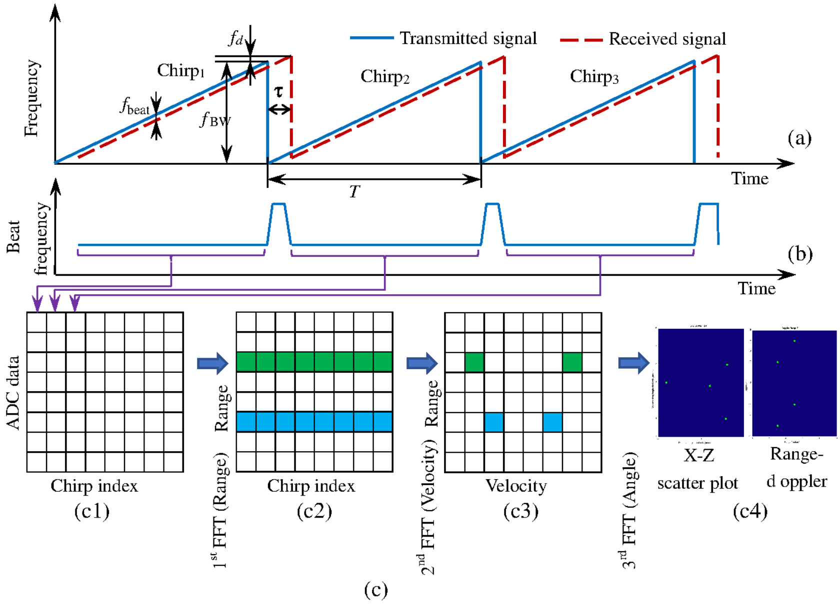

Figure 2.12: The basic principle of the FMCW radar with the sawtooth shape modulation:(a) the transmitted and received signal, (b) the corresponding beat frequency, and (c) the beat signal processing flow.[1]

$$s_{LFM}(t) = A_t e^{j\left[2\pi \int_0^t \left(f_c + \frac{B}{T_S} t\right) dt + \phi(t)\right]} \tag{2.32}$$

$$= A_t e^{j\left[2\pi\left(f_c + \frac{B}{2T_S} t\right) t + \phi(t)\right]}, 0 < t < T_s \tag{2.33}$$

where A_t is the amplitude of the transmitted signal, f_c is the carrier frequency, B is the bandwidth and T_s represents the chirp duration.

The transmitted signal is reflected by the chest wall of the object. As the chest wall moves very slowly, it can be considered immobile at the moment the electromagnetic waves are reflected. Suppose we have a target with an initial range R and a radial velocity v_r, the time delay will be $\tau = \frac{2(R+v_r t)}{c}$.Thus the received signal can be expressed by:

$$s_r(t) = s_{LFM}(t - \tau) \tag{2.34}$$

$$= A_r e^{j\left\{2\pi\left[f_c + \frac{B}{2T_S}(t-\tau)\right](t-\tau) + \phi(t-\tau)\right\}} \tag{2.35}$$

$$\tag{2.36}$$

where A_r represents the amplitude of received signal. After mixing with the local oscillator signal, the high frequency components will be filtered out, which produces a baseband signal:

$$s_b(t) = A_b e^{j\left[2\pi\left(\frac{B}{T_S}\tau t + f_c \tau - \frac{B}{2T_S}\tau^2\right) + \phi(t) - \phi(t-\tau)\right]} \tag{2.37}$$

$$\approx A_b e^{j2\pi\left(\frac{B}{T_S}\tau t + f_c \tau\right)} \tag{2.38}$$

the term $\frac{B}{2T_s}\tau^2$ is called residual video phase, which can be ignored. $\phi(t)-\phi(t-\tau)$ is the residual phase noise, which is also negligible, especially when the target is close to radar. Then we could obtain the phase of beat signal as:

2

$$\phi_b(t) = 2\pi\left[\frac{2f_c R}{c} + \left(\frac{2f_c \cdot v_r}{c} + \frac{2B \cdot R}{c \cdot T_s}\right)t + \frac{2B \cdot v_r}{c \cdot T_s}t^2\right] \tag{2.39}$$

By taking the differential, the frequency of beat signal can be calculated:

$$f_b = \frac{1}{2\pi}\frac{\partial \phi_b(t)}{\partial t} = \frac{2B \cdot R}{c \cdot T_s} + \frac{2f_c \cdot v_r}{c} \tag{2.40}$$

in which the Range-Doppler-Coupling is emitted. As introduced previously, the analog beat signal is sampled at frequency $\frac{1}{T}$ by the ADC module and get to the time discrete form:

$$s_b(n) = A_b \cdot w(n)\, e^{j2\pi\left[\frac{2f_c R}{c} + \left(\frac{2f_c \cdot v_r}{c} + \frac{2B \cdot R}{c \cdot T_s}\right)nT\right]} \tag{2.41}$$

It can be seen that the frequency of the beat signal is proportional to the range of the chest wall. Thus the target position can be calculated by reconstructing the signal frequency. We could use the same phase extraction procedure as in the CW radar system. However, the introduction of the arctangent function will bring us a typical "unwrap" problem. The unwrap function compensates for a π where the phase is not continuous, but this will reduce its robustness to noise. Therefore, many researchers have proposed other algorithms to recover the respiration component from the beat signal; some of them are discussed in Chapter 3.

The overall comparison of the three radar systems discussed above is summarised in Table 2.1[64, 65].

In the subsequent study, the modelling and simulation in Chapter 4 is based on the FMCW radar because of the desire for higher SNR and the lack of restrictions on power consumption, while the experimental part in Chapter 5 is based on the UWB radar, as this model of radar was readily available, compact and simple to use for the experimental verification outside of laboratory conditions. As the scenario assumed in this study was in a home sleep environment and the measurements were taken on a single person, the results would not change massively if another type of radar capable of measuring range information had been used. This is because the proposed signal processing pipeline starts from range-time matrices generated by both FMCW and UWB radars.

2.4. CONCLUSION

This chapter presented a mathematical model of chest wall displacement due to normal cardiopulmonary activity and mathematically models of different types of sleep apnea. Then three radars that are widely used in the field of contactless vital sign monitoring are introduced: CW, FMCW and UWB radars, followed by a brief description of the radar principles and the signal processing pipeline for the received beat frequency signals. Lastly, a comparison of the three radars' applications is discussed as a conclusion.

Table 2.1: Comparison of Radar-Based Vital Signs Monitoring Systems

Radar Type	**Advantage**	**Disadvantage**
CW	1. Simple topology 2. Low power consumption	Lack of range information
FMCW	1. Enhanced result with MIMO antenna topologies 2. Combine the results from each channel 3. Relatively high SNR	1. Relatively high level of phase noise 2.Require calibration to compensate for nonlinearities during frequency sweeping 3. High power consumption
UWB	1. Good range resolution 2. Relatively high SNR 3. Immunity to spurious and multipath interference	1. Require high-speed ADC 2. Limited power of the pulse

3

Algorithms Developed for Sleep Apnea Detection

This chapter demonstrates the pipeline of signal processing and breathing pattern classification for sleep apnea detection. The block diagram of the complete algorithm can be seen in Figure 3.1. This chapter is structured as follows: Section 3.2 describes three signal pre-processing methods based on phase and time-frequency analysis and discusses feature extraction and signal denoising algorithms. Section 3.3 and Section 3.4 discuss strategies of respiration frequency estimation and apnea detection respectively. Afterwards, the pros and cons of different signal processing methods are stated as the conclusion of this chapter.

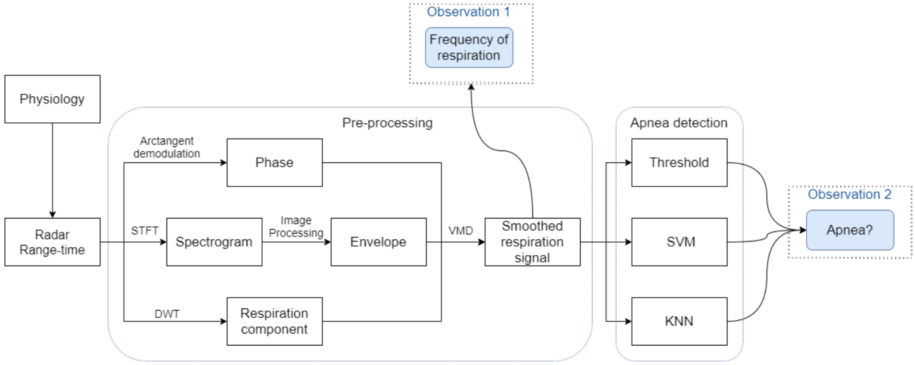

Figure 3.1: Signal processing pipeline proposed in this thesis work

3.1. Signal Processing and Classification Pipeline

The pipeline of the complete signal processing and breathing pattern classification algorithm is shown in Figure 3.1. To obtain the waveform of respiration signal, the range-time matrix obtained from the radar is processed with three pre-processing algorithms: Arctangent demodulation, DWT and STFT together with image processing. Then the reconstructed respiration waveform is processed for noise reduction and smoothing via VMD and the result is considered as feature for apnea detection. Threshold-based approach and applied machine learning are employed for breathing obstruction detection.

Note that each of the three branches of pipeline represents one possible signal processing as well as classification method. Not all of these branches are necessary, they can be substituted for each other. A comparison of these methods will be developed in subsequent sections.

3.2. Pre-processing Algorithms

3.2.1. Phase Extraction

As demonstrated in Chapter 2, the phase of the signal is obtained by equation 2.20. However, this process requires using the arctangent function, which will introduce a typical "unwrap" problem. Since the range of the arctangent function is $(-\pi/2, \pi/2)$, the calculated phase is limited to this interval, which breaks the original continuity of the signal phase. Therefore, it is necessary to apply a process to unwrap the values of the phase, that is, to compensate the phase of π at the point where the phase is interrupted. But unwrapping is not easy. If the signal varies too fast, it will cause the failure of the unwrapping process. In the meanwhile, the unwrapping process will also reduce the algorithm's robustness to noise. An algorithm that can avoid this problem is the differentiate and cross multiply algorithm, which takes advantage of the fact that although the arctangent function is a transcendental function, which is difficult to calculate, its derivative is a rational function[66].

The derivative of arctanget is: $\frac{\mathrm{d}arctan(x)}{\mathrm{d}t} = \frac{1}{(1+x^2)} \times \frac{\mathrm{d}x}{\mathrm{d}t}$. Therefore, the corresponding phase value can be obtained by integrating $\frac{\mathrm{d}arctan(x)}{\mathrm{d}t} = \frac{1}{(1+x^2)} \times \frac{\mathrm{d}x}{\mathrm{d}t}$, and the integration process ensures the continuity of the calculation result.

For instance, the value of $arctan(Q(t)/I(t))$ can be calculated as follows:

$$arctan(Q(t)/I(t)) = \int_t^{-\infty} \frac{I^2(s)}{Q^2(s)+I^2(s)} \cdot \frac{\dot{Q}(s)I(s) - Q(s)\dot{I}(s)}{I^2(s)} \mathrm{d}s \tag{3.1}$$

$$\int_t^{-\infty} \cdot \frac{\dot{Q}(s)I(s) - Q(s)\dot{I}(s)}{Q^2(s)+I^2(s)} \mathrm{d}s \tag{3.2}$$

The above formula can be discretized as:

$$arctan(Q[n]/I[n]) \approx \sum_{k=-\infty}^{n} \frac{(Q[k]-Q[k-1])I[k] - Q[k](I[k]-I[k-1])}{Q^2[k]+I^2[k]} \tag{3.3}$$

where $Q[n] = Q(n\Delta t)$, $I[n] = I(n\Delta t)$.

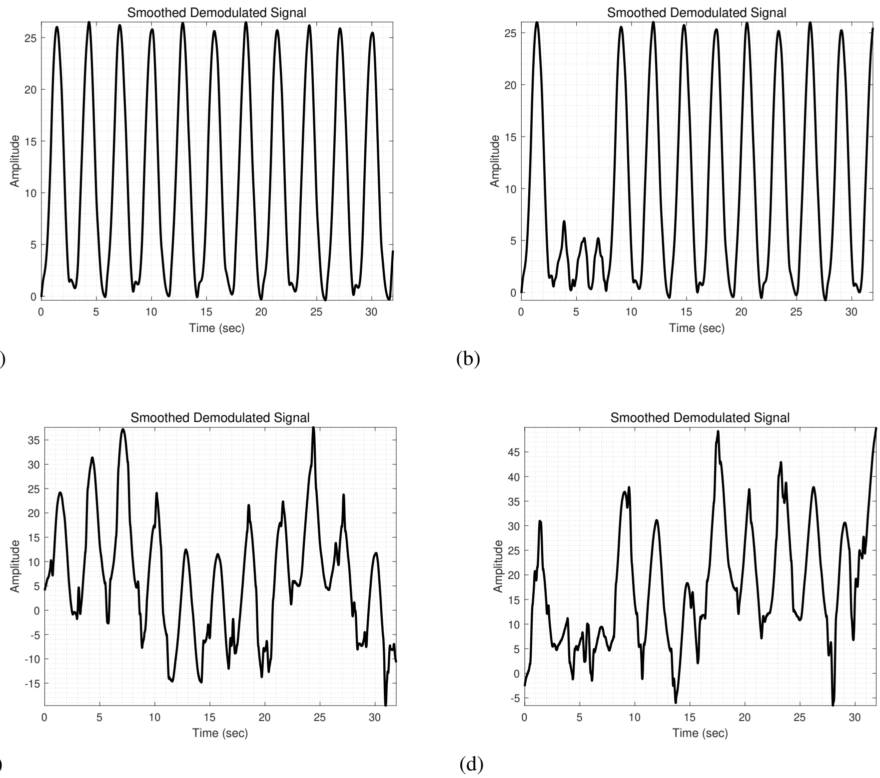

Figure 3.2: Results of phase extraction on simulation data: (a)normal respiration, without noise; (b) normal respiration, SNR=20 dB; (c) sleep apnea, without noise; (d) sleep apnea, SNR=20 dB

As shown in Figure 3.2, phase extraction with the differentiate and cross multiply algorithm could well reconstruct the desired signal in an clean environment; however, when there exists some noise, the result of phase extraction is not so reliable because the signal phase is easily affected by noise. Thus, alternative signal processing methods in the spectral domain are also explored.

3.2.2. SHORT-TIME FOURIER TRANSFORM

Short-time Fourier transform is an effective approach widely used in vital sign detection. As the most classic frequency domain analysis tool, Fourier transform also has its limitation, which is that it depicts the frequency spectrum globally and cannot reflect the characteristics of the local area in the time dimension. This limitation of the Fourier Transform is particularly severe for non-stationary signals as vital signs. Although people can clearly see the value of each frequency component contained in a whole signal from the Fourier transform, it struggles to obtain temporal information of the signal corresponding to the frequency domain component, which greatly reduces the role of Fourier transform in more sophisticated analysis. The short-time Fourier transform applies a sliding window with cer-

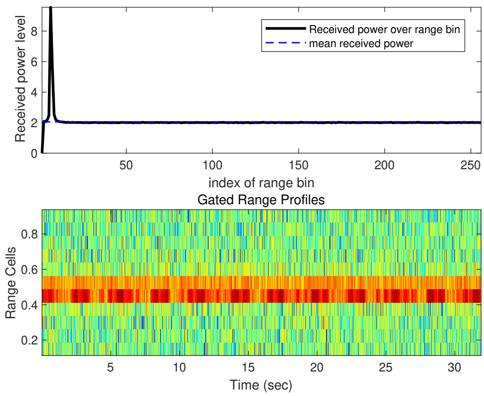

Figure 3.3: Range-Time plot of radar signal with noise added, SNR = 20dB

tain width and step length on the time domain signal, and calculate the Fourier transform of each window separately to obtain its corresponding frequency domain signals, which is spliced together to become time-frequency information.

The definition of short-time Fourier transform is as follows:

$$X(n,\omega) = \sum_{m=-\infty}^{\infty} x(m)w(n-m)e^{-j\omega m} \tag{3.4}$$

where $x(m)$ is the input signal and $w(m)$ is the window function, which is inverted in time and has an offset of n samples. $X(n,\omega)$ is a two-dimensional function of time t and frequency ω. Based on which time-frequency analysis could be performed, for example to obtain the spectrogram by $S(n,\omega) = |X(n,\omega)|^2$.

The range-time plot of the simulated radar signal is shown in Figure 3.3; the target was located half a meter away from the radar. Then spectrogram was applied on the coherent range bins where the target was. The results are shown in Figure 3.4, Figure 3.4a and Figure 3.4b respectively show the time-frequency information of normal breathing and obstructive sleep apnea under ideal conditions, while Figure 3.4c and Figure 3.4d demonstrate the spectrogram of normal respiration and sleep apnea in a noisy environment (with SNR=20 dB). After comparing with the results of phase extraction, it can be found that the short-time Fourier transform is more robust to noise.

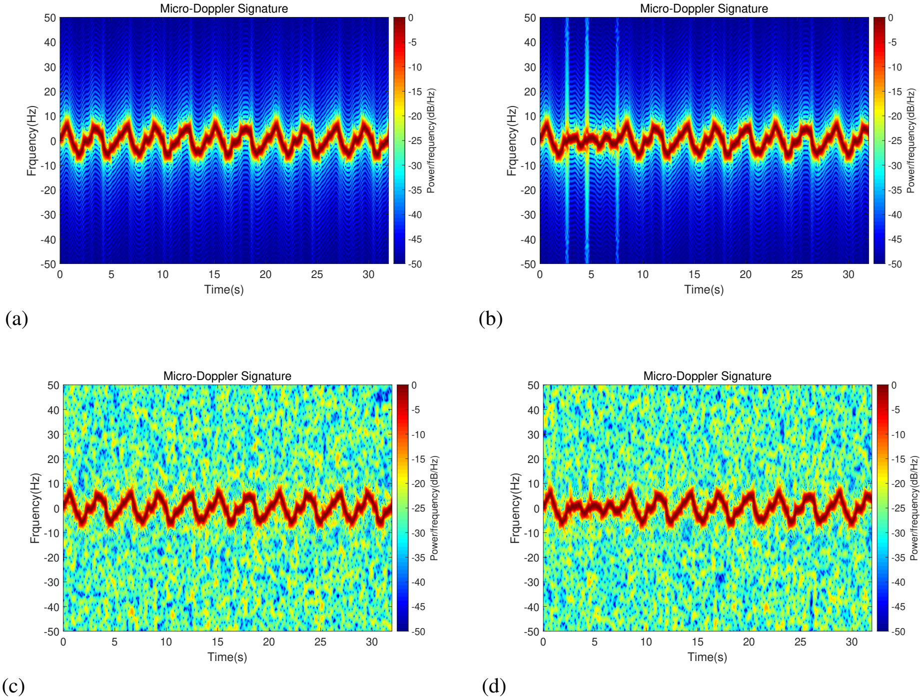

Figure 3.4: Results of spectrogram of simulation data: (a)normal respiration, without noise; (b) normal respiration, SNR=20 dB; (c) sleep apnea, without noise; (d) sleep apnea, SNR=20 dB

It can be noted that in Figure 3.4b, artefacts appear at the time bins corresponding to approximately 3s, 5s, and 8s. In the simulation of obstructive sleep apnea, due to the simplicity of the model, the decrease in respiratory amplitude cannot be a continuous process as in practice. In contrast, the respiration obstruction can only be approximated by a sudden drop in signal amplitude, which will lead to the appearance of intermittent points in the mathematical model built, further leading to the formation of artefacts in the frequency domain. The existence of artefacts is due to limitations in accurately modelling the signal and is not a defect in the signal processing algorithm, as can be seen from the following envelope extraction results where artefacts do not show much impact on signal waveform reconstruction. Moreover, in practical application scenarios, artefacts do not appear; thus, the algorithm's reliability is ensured.

3.2.3. DISCRETE WAVELET TRANSFORM

Apart from STFT, wavelet transform (WT) is also a type of transform which is capable of providing time localization of the spectral components, hence delivering us the time-frequency information of the signal. WT is widely used in the field of biological signals analysis, due to its effectiveness in non-stationary signals processing[67][68]. Meanwhile, because of the particularity of wavelet base, wavelet transform is non-redundant and allows more accurate local description and separation of signal features. Discrete wavelet transform (DWT), also called binary wavelet transform, is obtained by discretizing the scale and displacement of continuous wavelet transform (CWT) by a power of two. To provide sufficient information for signal synthesis and realize an utterly reversible transformation, discrete wavelet transform requires the wavelet base to be orthogonal or biorthogonal. In the discrete case, filters with different cut-off frequencies are used to analyze signals of different scales. The signal passes a series of high-pass filters to analyze high frequencies and low-pass filters to analyze low frequencies[69].

Assume that $\psi(t) \in L^2(R)$, and its Fourier transform is $\hat{\psi}(\omega^*)$, when $\hat{\psi}(\omega)$ satisfies:

$$C_\psi = \int_R \frac{\left|\hat{\psi}(\omega)\right|^2}{|\omega|} d\omega < \infty \tag{3.5}$$

Then ψ is called a basic wavelet or mother wavelet. After scaling and translating the mother wavelet, a wavelet sequence is obtained:

$$\psi_{s,\tau} = \frac{1}{\sqrt{|s|}} \psi\left(\frac{t-\tau}{s}\right), \tau, s \in \boldsymbol{R}; s \neq 0 \tag{3.6}$$

Which contains two variables, s and τ, the scale and translation parameters, respectively. For any function $f(t) \in L^2(R)$, the continuous wavelet transform is defined as:

$$W_f(s,\tau) = \langle f, \psi_{s,\tau} \rangle = \frac{1}{\sqrt{|s|}} \int x(t) \psi^* \left(\frac{t-\tau}{s}\right) dt \tag{3.7}$$

The definition of inverse transform is as follows:

$$f(t) = \frac{1}{C_\psi} \int_{-\infty}^{\infty} \int_{-\infty}^{\infty} \frac{1}{s^2} W_f(s,\tau) \psi\left(\frac{t-\tau}{s}\right) ds d\tau \tag{3.8}$$

Generally, the discrete formulas of the scale parameter s and the translation parameter τ are respectively taken from the CWT on a dyadic grid: for instance, $s_0 = 2$ and $t_0 = 1$, yielding $s = 2^j$ and $t = k \cdot 2^j$. Note that $s_0 \neq 1$ and when discretizing the translation parameter τ, we usually make a uniform discretization value to cover the entire time axis; and the sampling interval τ satisfies the Nyquist sampling theorem.

The hierarchical structure as shown in Figure 3.5 demonstrates the procedures of the DWT, where $x[n]$ denotes the original signal to be decomposed, and $g[n]$ and $h[n]$ are lowpass and highpass filters, respectively. The frequency in this case is normalized to π.

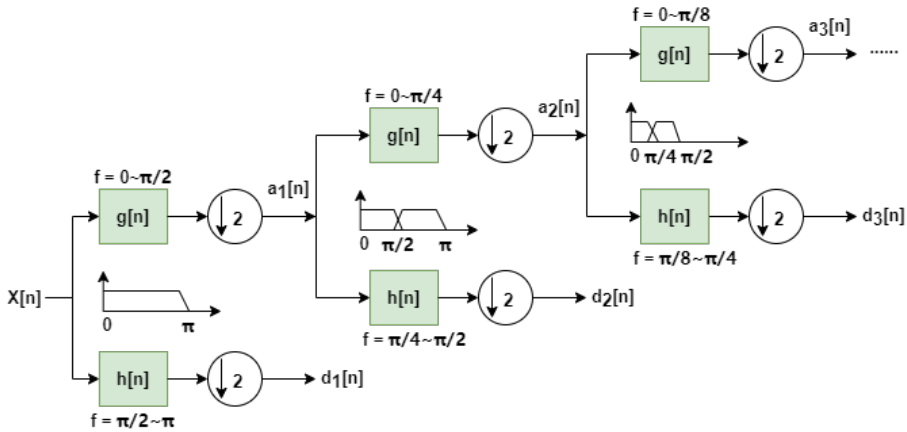

Figure 3.5: Third level filter bank block diagram representation of DWT

The Daubechies N (db N) wavelet is a widely used wavelet basis function in vital signal processing because of its excellent regularity, orthogonality and tight support[70, 71]. Db N wavelets are characterized by a larger order of vanishing moments as the order (sequence N) increases. The higher the vanishing moment, the better the smoothness, the stronger the localisation of the frequency domain, but it makes the time domain less tightly supported, while the computational effort increases significantly and the real time performance becomes worse[72]. Here the fourth order Daubechies basis was chosen[73, 74]. DWT with db4 base was used as a filter in the proposed algorithm to extract the respiration signal whose frequency locates in the interval of 0.1 to 0.7 Hz. After the nth level decomposition, $n = log_2\left(\frac{Fs}{2\times f_r}\right)$, respiration signal could be extracted from the range-time signal. The four lowpass and highpass, decomposition and reconstruction filters associated db4 wavelet and the scaling function as well as the wavelet waveform are shown in Figure 3.6

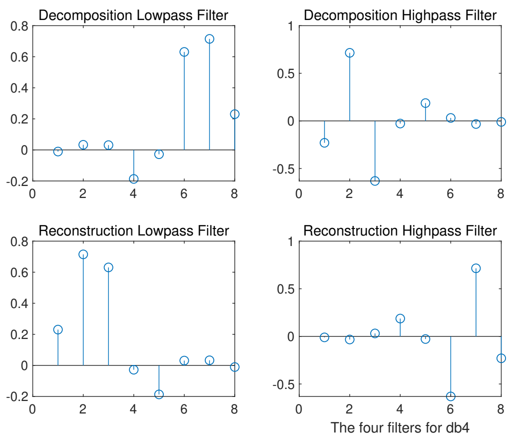

(a)

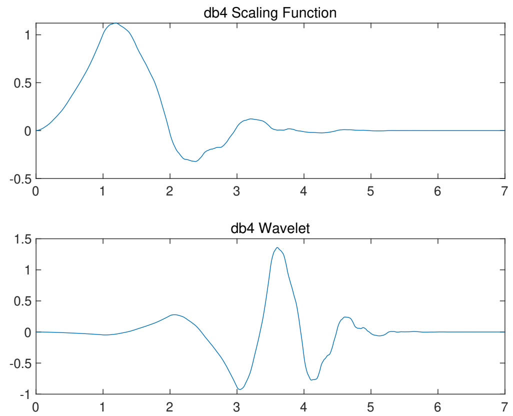

(b)

Figure 3.6: Characteristics of the Daubechies' extremal phase wavelet with 4 vanishing moments:(a) the four lowpass and highpass, decomposition and reconstruction filters associated db4 wavelet; (b) the scaling function and wavelet waveform.

The signal decomposition result in simulation environment when SNR = 20 dB could be seen in Figure 3.7. Waveform of respiration is marked in red.

3.2.4. ENVELOPE EXTRACTION

The envelope extraction algorithm is based on image processing. It aims to find the pixels with the highest red saturation in the time-frequency plot as shown in Figure 3.4.

1. Separate RGB channel and get the saturation of the red component;
2. For each column, compute the historgram of the red saturation and normalize it to 1;

3

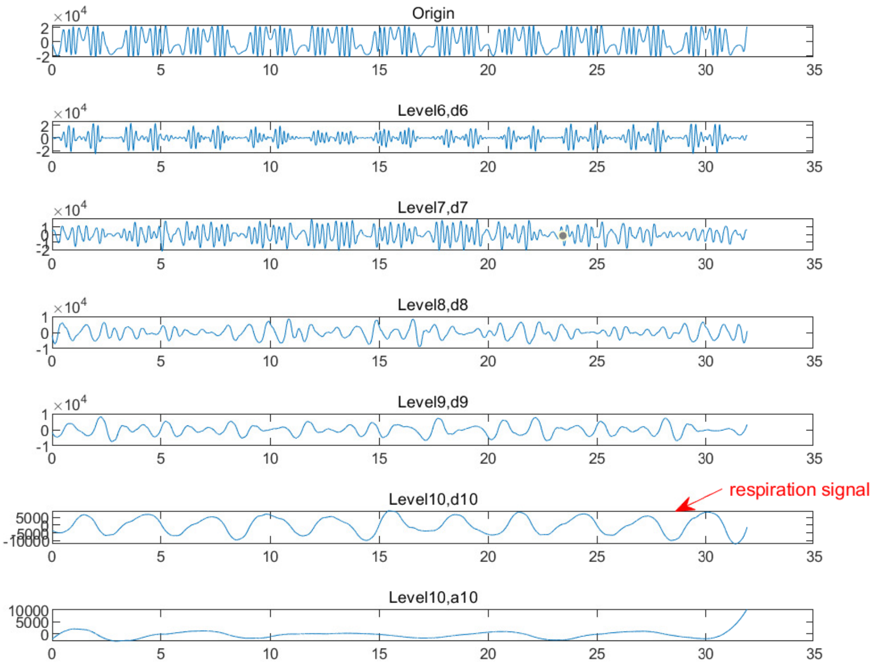

Figure 3.7: DWT decomposition of radar signal containing respiration, SNR = 20 dB

3. For each time bin, eliminate the the pixels with a value of normalized red saturation less than 0.9.

The extracted envelope is illustrated in Figure 3.8.

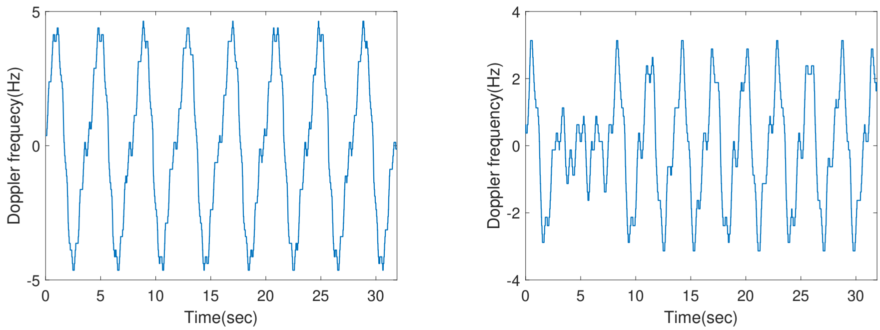

(a) (b)

Figure 3.8: Results of envelope extraction on simulation data: (a)normal respiration, without noise; (b) sleep apnea, without noise

3.2.5. NOISE REDUCTION AND SIGNAL SMOOTHING BASED ON VARIATIONAL MODE DECOMPOSITION

As can be seen in Figure 3.4, the signal waveform obtained by envelope extraction is not smooth and has many spikes due to the presence of noise as well as the heartbeat signal, which can negatively affect the subsequent breathing obstruction detection algorithm. It is necessary to decompose the respiratory signal and perform a denoising operation. Therefore, variational mode decomposition algorithm is introduced in the signal processing pipeline.

The basic concept of modal decomposition is to consider a signal as being a superposition of sub-signals of different "modes", while variational modal decomposition believes that the signal is superimposed by sub-signals with different frequencies. Here a mode, also called Intrinsic Mode Functions (IMF), is defined as a signal whose number of local extrema and zero-crossings should be the same, or differ by one at most. In many later researches, the definition was slightly revised to amplitude-modulated-frequency-modulated (AM-FM) signals, which can be expressed as:

$$u_k(t) = A_k(t)\, cos(\Phi_k(t)) \tag{3.9}$$

where the phase $\Phi_k(t)$ is a non-decreasing function whose first derivative is non-negative, ${\Phi_k}'(t) \geq 0$. It is worth noting that the envelope $A_k(t) \geq 0$ and the instantaneous frequency $\omega_k(t) := {\Phi_k}'(t)$ change much slower than the phase $\Phi_k(t)$[75][76]. This definition ensures that on a sufficiently long interval $[t-\delta, t+\delta], \delta \approx 2\pi/{\Phi_k}'(t)$, the mode $u_k(t)$ can be regarded as a pure harmonic signal who has a limited bandwidth. The total practical bandwidth of an IMF was estimated as[77]:

$$BW_{AM-FM} = 2\left(\Delta f + f_{FM} + f_{AM}\right) \tag{3.10}$$

VMD is to iteratively search for the optimised solution of the variational model to determine the mode $u_k(t)$ and its corresponding centre frequency $\omega_k(t)$ and bandwidth BW, note that the obtained IMF should result in a smallest sum of the bandwidth. The following scheme was proposed to determine the bandwidth of each IMF[78]:

1. The analytical signal corresponding to each intrinsic mode $u_k(t)$ is calculated through the Hilbert transform to obtain a unilateral spectrum:

$$u_{k,A}(t) = \left(\delta(t) + \frac{j}{\pi t}\right) * u_k(t) \tag{3.11}$$

where $\delta(t)$ represents Dirac function.

2. By multiplying $u_{k,A}(t)$ and the exponential signal to the corresponding estimated centre frequency ω_k, the spectrum of the pattern is shifted to the baseband:

$$\left[\left(\delta(t) + \frac{j}{\pi t}\right) * u_k(t)\right] e^{-j\omega_k t} \tag{3.12}$$

3. Estimate the bandwidth of each mode by determining the squared L^2-norm of the gradient. This forms a constrained variational problem:

$$\min_{\{u_k\},\{\omega_k\}} \left\{ \sum_k \left\| \partial_t \left[\left(\delta(t) + \frac{j}{\pi t}\right) * u_k(t)\right] e^{-j\omega_k t} \right\|_2^2 \right\} \quad \text{s.t.} \quad \sum_k u_k = f \tag{3.13}$$

where $\{u_k\} := \{u_1, ..., u_k\}$ and $\{\omega_k := \{\omega_1, ..., \omega_k\}$ represent set of all K IMFs and their centre frequencies, respectively.

The second penalty and Lagrangian multiplier are used to find the optimal solution to convert the appeal constraint problem into a non-constrained problem. The unconstrained problem is usually solved by using alternate direction multiplier, which is updated iteratively to eventually obtain all signal decomposition patterns[78].

Specifically, we follow the steps below to solve the problem:

1. We introduce the second penalty and the augmented Lagrangian multiplier $\mathscr{L}$ as follows:

$$\mathscr{L}(\{u_k\},\{\omega_k\},\lambda) := \alpha \sum_k \left\| \partial_t \left[\left(\delta(t) + \frac{j}{\pi t}\right) * u_k(t)\right] e^{-j\omega_k t} \right\|_2^2 \tag{3.14}$$

$$+ \left\| f(t) - \sum_k u_k(t) \right\|_2^2 + \left\langle \lambda(t), f(t) - \sum_k u_k(t) \right\rangle. \tag{3.15}$$

where α and $\lambda(t)$ are the quadratic penalty coefficient and the Lagrange multiplier respectively.

2. The original minimization problem is now converted to a convex problem which aims to find the saddle point of the $\mathscr{L}$. This could be solved by alternate direction method of multipliers (ADMM); the specific steps of the operation are as follows:

Algorithm 1 ADMM optimization concept for VMD

Initialize $\{u_k^1\}, \{\omega_k^1\}, \lambda^1, n \leftarrow 0$
repeat
set $n \leftarrow n+1$
for $k = 1 : K$ **do**
Update u_k:
$u_k^{n+1} \leftarrow \operatorname*{argmin}_{u_k} \mathscr{L}\left(\{u_{i<k}^{n+1}\}, \{u_{i\geq k}^n\}, \{\omega_i^n\}, \lambda^n\right)$ (subproblem. 1)
end for
for $k = 1 : K$ **do**
Update ω_k:
$\omega_k^{n+1} \leftarrow \operatorname*{argmin}_{\omega_k} \mathscr{L}\left(\{u_i^{n+1}\}, \{\omega_{i<k}^{n+1}\}, \{\omega_{i\geq k}^n\}, \lambda^n\right)$ (subproblem. 2)
end for
Dual ascent:
$\lambda^{n+1} \leftarrow \lambda^n + \tau\left(f - \sum_k u_k^{n+1}\right)$
until convergence: $\sum_k \|u_k^{n+1} - u_k^n\|_2^2 / \|u_k^n\|_2^2 < \epsilon$

3. In Algorithm 1, the problem of minimization $w.r.t.$ u_k and ω_k remains:

   A. minimization $w.r.t.$ u_k:
   In order to update the modes, subproblem. 1 could be converted to:

$$u_k^{n+1} = \operatorname*{argmin}_{u_k \in X} \left\{ \alpha \left\| \partial_t \left[\left(\delta(t) + \frac{j}{\pi t} \right) * u_k(t) \right] e^{-j\omega_k t} \right\|_2^2 + \left\| f(t) - \sum_i u_i(t) + \frac{\lambda(t)}{2} \right\|_2^2 \right\} \tag{3.16}$$

The above minimized term can be transformed to the frequency domain using the properties of Parseval/Plancherel Fourier isometry under the L^2-norm and the differential properties of the Fourier transform:

$$\hat{u}_k^{n+1} = \operatorname*{argmin}_{\hat{u}_k, u_k \in X} \left\{ \alpha \left\| j\omega \left[(1 + \operatorname{sgn}(\omega + \omega_k)) \, \hat{u}_k(\omega + \omega_k) \right] \right\|_2^2 + \left\| \hat{f}(\omega) - \sum_i \hat{u}_i(\omega) + \frac{\hat{\lambda}(\omega)}{2} \right\|_2^2 \right\}. \tag{3.17}$$

Replacing $\omega - \omega_k$ by ω, we could get:

$$\hat{u}_k^{n+1} = \underset{\hat{u}_k, u_k \in X}{\arg\min} \left\{ \alpha \left\| j(\omega - \omega_k) \left[\left(1 + \operatorname{sgn}(\omega)\right) \hat{u}_k(\omega) \right] \right\|_2^2 + \left\| \hat{f}(\omega) - \sum_i \hat{u}_i(\omega) + \frac{\hat{\lambda}(\omega)}{2} \right\|_2^2 \right\}. \tag{3.18}$$

Using the Hermitian symmetry of real signals in the reconstruction fidelity term, the two terms of Equation 3.18 can be rewritten as:

$$\hat{u}_k^{n+1} = \underset{\hat{u}_k, u_k \in X}{\arg\min} \left\{ \int_0^\infty 4\alpha(\omega - \omega_k)^2 \left| \hat{u}_k(\omega) \right|^2 + 2 \left| \hat{f}(\omega) - \sum_i \hat{u}_i(\omega) + \frac{\hat{\lambda}(\omega)}{2} \right|^2 d\omega \right\}. \tag{3.19}$$

By letting the first variation in the positive frequency disappear, it is easy to find a solution to this secondary optimization problem:

$$\hat{u}_k^{n+1}(\omega) = \frac{\hat{f}(\omega) - \sum_{i \neq k} \hat{u}_i(\omega) + \frac{\hat{\lambda}(\omega)}{2}}{1 + 2\alpha(\omega - \omega_k)^2} \tag{3.20}$$

B. minimization *w.r.t.* ω_k:
Due to the fact that the center frequencies ω_k only appears in the prior bandwidth, the corresponding problem subproblem. 2 could be converted to:

$$\omega_k^{n+1} = \underset{\omega_k}{\arg\min} \left\{ \left\| \partial_t \left[\left(\delta(t) + \frac{j}{\pi t} \right) * u_k(t) \right] e^{-j\omega_k t} \right\|_2^2 \right\} \tag{3.21}$$

As we have done to the previous optimization problem, we transform it to the spectrum domain and get:

$$\omega_k^{n+1} = \underset{\omega_k}{\arg\min} \left\{ \int_0^\infty (\omega - \omega_k)^2 \left| \hat{u}_k(\omega) \right|^2 d\omega \right\} \tag{3.22}$$

The interactive formula will be:

$$\omega_k^{n+1} = \frac{\int_0^\infty \omega \left| \hat{u}_k(\omega) \right|^2 d\omega}{\int_0^\infty \left| \hat{u}_k(\omega) \right|^2 d\omega} \tag{3.23}$$

4. By substituting the solutions to subproblem. 1 and subproblem. 2, the complete algorithm for VMD is discribed in Algorithm 2.

The VMD algorithm is used to decompose the extracted envelope into modes with different frequencies, and determine the respiratory signal by comparing the center frequencies of the IMFs with the respiratory frequency interval. Through this step, the heartbeat and

Algorithm 2 Complete Optimization of VMD

Initialize $\{\hat{u}_k^1\}, \{\omega_k^1\}, \hat{\lambda}^1, n \leftarrow 0$
repeat
  set $n \leftarrow n+1$
  for $k = 1 : K$ **do**
    Update $\hat{u}_k$ for all $\omega \geq 0$:
    $\hat{u}_k^{n+1}(\omega) \leftarrow \frac{\hat{f}(\omega) - \sum_{i<k} \hat{u}_i^{n+1}(\omega) - \sum_{i>k} \hat{u}_i^n(\omega) + \frac{\hat{\lambda}^n(\omega)}{2}}{1 + 2\alpha\left(\omega - \omega_k^n\right)^2}$
    Update ω_k:
    $\omega_k^{n+1} \leftarrow \frac{\int_0^\infty \omega \left|\hat{u}_k^{n+1}(\omega)\right|^2 d\omega}{\int_0^\infty \left|\hat{u}_k^{n+1}(\omega)\right|^2 d\omega}$
  end for
  Dual ascent for all $\omega \geq 0$:
  $\hat{\lambda}^{n+1}(\omega) \leftarrow \hat{\lambda}^n(\omega) + \tau\left(\hat{f}(\omega) - \sum_k \hat{u}_k^{n+1}(\omega)\right)$
until convergence: $\sum_k \left\| \hat{u}_k^{n+1} - \hat{u}_k^n \right\|_2^2 / \left\| \hat{u}_k^n \right\|_2^2 < \epsilon$

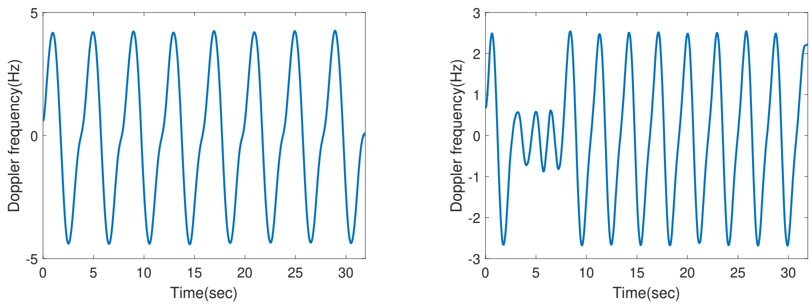

(a) (b)

Figure 3.9: Results of signal smoothing by VMD: (a)normal respiration, without noise; (b) sleep apnea, without noise

other noises are filtered out; the smoothed signal after VMD is applied is depicted in Figure 3.9. It could be seen that the respiration component is well retrieved.

After VMD smoothing, the improvement in signal reproduction is especially noticeable when the signal-to-noise ratio is low, as could be seen in Figure3.10. This is the result of the simulation with a SNR of three. Figure 3.10a, 3.10b and 3.10c show the envelope of normal breathing, CSA and OSA extracted from spectrogram, and Figure 3.10d, 3.10e and 3.10f corresponds to their results after VMD smoothing, respectively. It can be observed that plenty of burrs which might affect the result of the breathing obstruction test vanished.

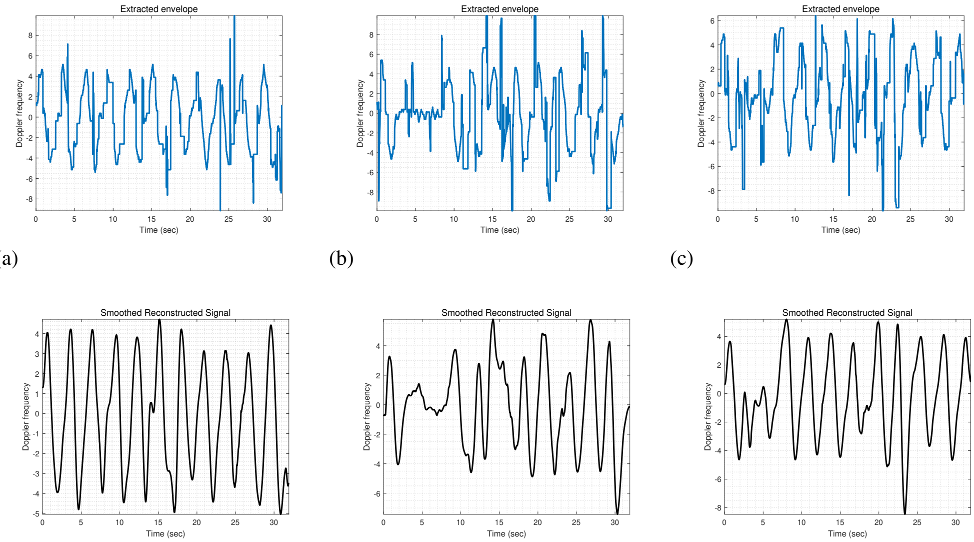

(a) (b) (c)

(d) (e) (f)

Figure 3.10: Improvement of reconstructed signal after VMD when SNR = 3 dB: signal before VMD (a) normal breath (b) CSA (c) OSA, and signal after VMD (d) normal breath (e) CSA (f) OSA

3.3. VITAL SIGNS FREQUENCY ESTIMATION

As demonstrated in Figure 3.1, after noise reduction process, the smoothed respiration signal is obtained, based on which the breathing rate could be estimated. The frequency is estimated by calculating the frequency spectrum of the reconstructed biological signal filtered by the second-order Butterworth bandpass filter. The filter is used to ensure that spurious and noise that may affect the estimation of the breathing frequency are filtered out and only signals with frequencies in the frequency range of normal breathing ($[0.1Hz, 0.7Hz]$, as demonstrated in the previous chapter) are retained. Here, a second-order Butterworth bandpass filter with a centre frequency of 0.4Hz and a bandwidth of 0.7Hz is applied. IIR filter is used because they typically meet a specific set of specifications at a much lower filter order than the corresponding FIR filter. Furthermore, the distortion caused by the non-linear phase of the IIR filter can be circumvented as the MATLAB "*filtfilt*" function allows the use of a non-causal zero-phase filtering method. Furthermore, as the signal used for frequency estimation has already been smoothed via VMD described previously, a higher-order filter is not required for accurate frequency screening. Thus, the order of the IIR filter has been determined to be second order.

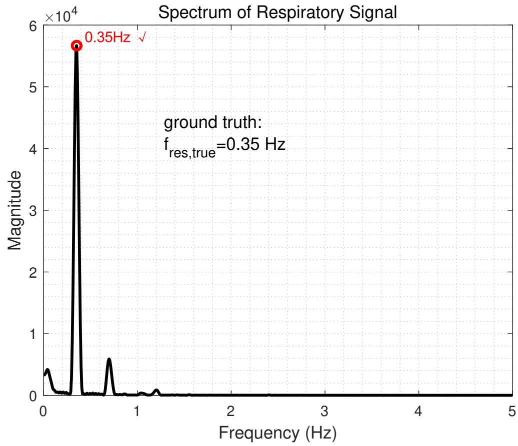

Figure 3.11: Respiration rate estimation for modelled signal under SNR = 20dB with ground truth $f_{res\_true} = 0.35Hz$

Frequency estimation result for the signal shown in Figure 3.9 could be seen in Figure 3.11. The comparison with the ground truth shows that the respiratory rate is accurately estimated.

The root mean square error of the respiratory frequency estimates for the sample set at different signal-to-noise ratios will be elaborated in Chapter 4.

3.4. SLEEP APNEA DETECTION

3.4.1. THRESHOLD-BASED DETECTION

As demonstrated in Chapter 2, the obstructive sleep apnea is modelled by a 50% drop in breathing amplitude and simulate CSA by vanishing of chest movement caused by respiration. Based on this simulation settings, a method that detects apnea by setting a threshold of 50% drop in average amplitude is proposed. According to the standard for sleep apnea detection introduced by the American Academy of Sleep Medicine (AASM), apnea is reported when there is a drop in the signal amplitude of the baseline for at least 10 seconds [79]. Note that when building the simulation environment, the sampling rate and PRF were set at a high value to obtain higher distances and Doppler resolution, resulting in a massively large radar data. Due to computer memory limitations, the duration of the generated apnea was half the duration of that in reality; thus the duration was set to half the clinical diagnostic criteria when performing the respiratory obstruction diagnosis. As a result, the reconstructed signal is split into segments of 5s with an overlap of 4s. Then the average amplitude for each segment is computed, and the amplitude drop is compared with the baseline, set to be the maximum average amplitude of these segments. Those segments with an amplitude decrease of more than 60% are labelled as apnea.

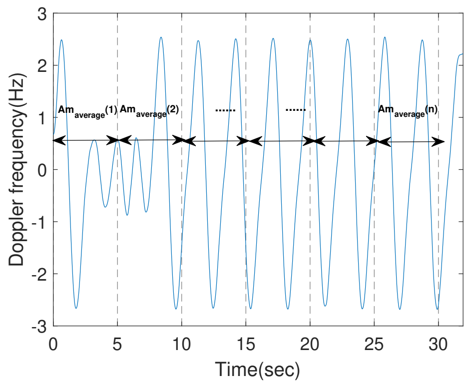

Figure 3.12: Demonstration of apnea detection based on threshold

3.4.2. Apnea Detection using Applied Machine Learning

In addition to applying simple methods of setting thresholds, classifiers based on machine learning have also been used for sleep apnea detection. The threshold-based approach is simple and easy to implement, but as the physiology of the subject during respiratory obstruction varies greatly in terms of the value of the change in chest wall displacement, the threshold setting has to change depending on the subject being monitored. Generally, several sets of reference tests are required to assist in setting the appropriate threshold after changing the subject, which results in a lack of adaptivity and portability of the algorithm. On the contrary, although machine learning-based classifiers require a large number of samples and time to train, the trained model is highly portable and more suitable for practical applications.

In this subsection, two of the simplest machine learning algorithms that are widely used for human motion recognition and sleep pattern classification are presented: support vector machines with Gaussian kernels and KNN.

Support Vector Machine

The basic theory of Support Vector Machine (SVM) is to find the separation hyperplane that can correctly divide the training data set and have the largest geometric interval. As shown in Figure 3.13, the $w \cdot x + b = 0$ is the separating hyperplane. For a linearly separable data set, the unique separable hyperplane with the most significant geometric interval can always be found among an infinite number of such hyperplanes.

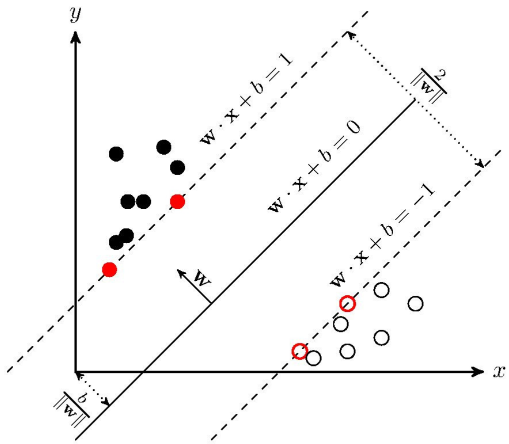

Figure 3.13: Demonstration of SVM principle with support vectors and separation hyperplane

Given a training data set on the feature space:

$$T = \{(\boldsymbol{x}_1, y_1), (\boldsymbol{x}_2, y_2), ..., (\boldsymbol{x}_N, y_N)\}$$

Where $\boldsymbol{x}_i \in \mathbb{R}^n$, $y_i \in \{+1, -1\}$, $\quad i = 1, 2, ..., N$, x_i is the ith eigenvector, and y_i is the class label. For a given data set T and hyperplane $w \cdot x + b = 0$, the geometric interval of the hyperplane with respect to the sample points (x_i, y_i) is defined as:

$$\gamma_i = y_i \left(\frac{\boldsymbol{w}}{\|\boldsymbol{w}\|} \cdot \boldsymbol{x}_i + \frac{b}{\|\boldsymbol{w}\|} \right)$$

The minimum value of the geometric interval of all sample points in the hyperplane is:

$$\gamma = \min_{i=1,2,...,N} \gamma_i$$

Therefore the problem of solving the maximum split hyperplane of the SVM model can be expressed as the following constrained optimization problem:

$$\begin{aligned} &\max_{w,b} \gamma \\ &\text{s.t.} \quad y_i \left(\frac{\boldsymbol{w}}{\|\boldsymbol{w}\|} \cdot \boldsymbol{x}_i + \frac{b}{\|\boldsymbol{w}\|} \right) \geq \gamma, \quad i = 1, 2, ..., N \end{aligned} \tag{3.24}$$

Which can be simplified to:

$$\begin{aligned} &\min_{\boldsymbol{w},b} \frac{1}{2} \|\boldsymbol{w}\|^2 \\ &\text{s.t.} \quad y_i (\boldsymbol{w} \cdot \boldsymbol{x}_i + b) \geq 1, \quad i = 1, 2, ..., N \end{aligned} \tag{3.25}$$

A delicate solution has been derived to solve this convex optimization problem, which could be seen in Algorithm 3.

3

Algorithm 3 Complete Solution to SVM

Input: $T = \{(\boldsymbol{x}_1, y_1), (\boldsymbol{x}_2, y_2), ..., (\boldsymbol{x}_N, y_N)\}$, in which $\boldsymbol{x}_i \in \mathbb{R}^n$ and $y_i \in \{+1, -1\}, i = 1, 2, ..., N$

Output: Hyperplane and classification decision function

1. Specify kernel function $K(x, z)$, penalty parameter $C > 0$

Solve: $\min\limits_{\alpha} \frac{1}{2} \sum_{i=1}^{N} \sum_{j=1}^{N} \alpha_i \alpha_j y_i y_j K(\boldsymbol{x}_i \cdot \boldsymbol{x}_j) - \sum_{i=1}^{N} \alpha_i$

s.t. $\sum_{i=1}^{N} \sum_{j=1}^{N} \alpha_i y_i = 0$

$0 \le \alpha_i \le C, \quad i = 1, 2, ..., N$

obtain the optimal solution $\boldsymbol{\alpha}^* = (\alpha_1^*, \alpha_2^*, ..., \alpha_N^*)^T$

2. Calculate $\boldsymbol{w}^* = \sum_{i=1}^{N} \alpha_i^* y_i \boldsymbol{x}_i$:

Select a component of $\boldsymbol{\alpha}^*$, α_j^* that satisfies the $0 < \alpha_j^* < C$

calculate $b^* = y_j - \sum_{i=1}^{N} \alpha_i^* y_i K(\boldsymbol{x}_i \cdot \boldsymbol{x}_j)$

3. Obtain the hyperplane:

$\boldsymbol{w}^* \cdot \boldsymbol{x} + b^* = 0$

and classification decision function:

$f(\boldsymbol{x}) = sign(\sum_{i=1}^{N} \alpha_i^* y_i K(x, x_i) + b^*)$

K-NEAREST NEIGHBOR ALGORITHM

K-Nearest Neighbour is a non-parametric machine learning algorithm based on the supervised learning technique. It does not involve a learning process from the training set; on the contrary, it is data-oriented, storing datasets and acting on them as it operates to classify them, which explains why it is also known as a lazy learner algorithm. The new data will be sorted into the category with the shortest Euclidean distance from it. The algorithm of KNN is demonstrated in Algorithm 4[80].

Algorithm 4 K-Nearest Neighbor Algorithm

Classify (X, Y, x)// X: training data, Y: class labels for X, x: unknown sample
for $i = 1 : m$ **do**
  Compute distance $d(X_i, x)$
end for
Compute set I containing indices for the k smallest distance $d(X_i, x)$.
return majority label for $\{Y_i where i \in I\}$

3.5. CONCLUSION

In this chapter, a signal processing pipeline that can provide the required details of thorax/abdomen movements with breath-to-breath accuracy is developed. Different pre-processing algorithms used to reconstruct the respiration waveform are discussed and compared. Based on the results the following conclusions could be drawn:

- Phase extraction is the simplest and most intuitive method, but is least robust to noise;
- Discrete wavelet transform is also a convenient approach and not easily interfered by noise, but the restoration of signal amplitude will be slightly distorted;

- Spectrogram shows superior robustness to noise and can restore signal waveforms very effectively; however, the extraction of the envelope requires additional image processing steps, and its performance will be limited by frequency resolution.

Moreover, sleep apnea detection methods based on threshold for signal magnitude and applied machine learning are also elucidated. The effectiveness of these algorithms will be further verified in the next two chapters by both the simulation data and experimental data.

4

Simulation Results

This chapter presents the simulation verification of the validity of the proposed algorithms. A model of vital signs captured by radar in different environments and on various subjects was built. Then the simulation signal was processed by the algorithms proposed in the previous chapter to obtain the features used to conduct apnea detection. The performance of the breath pattern classifiers is evaluated by the classification results on the simulated signal.

4.1. Strategy of Monte Carlo Simulation

In the previous chapter, the proposed algorithms were clarified, and the results of the preprocessing algorithm were given in a simulation environment where the rate and amplitude of heartbeat and respiration were fixed, and the $SNR = 20dB$. Monte Carlo simulation was introduced to study the effectiveness of this set of algorithms on different subjects under different noise levels and different sleeping positions. Monte Carlo simulation is a probabilistic model usually used in situations where there is intervention of random variables in a system to study the effect of random variables on the outcome, which will be environmental noise and parameters of vital signs in this research. The simulation process includes assigning multiple random values to the uncertain variables in the model to obtain their corresponding consequences, and obtain the estimated value by taking an average.

Two sets of Monte Carlo simulation will be performed. In this simulation, there are two random variables, the waveform of respiration signal and environmental noise. First, a set of Monte Carlo simulations for different test objects are designed, and the vital sign model established in it has a randomly selected amplitude and frequency. Because in reality, different targets breathe at distinct frequencies and amplitude, resulting in an inconsistent breathing signal. As introduced in Chapter 2, the ranges of respiratory rate is $[0.1Hz, 0.7Hz]$, while it's amplitude usually values in $[4mm, 12mm]$[48]. The cardiopulmonary activity usually has a frequency in the interval $[0.9Hz, 3Hz]$ and an amplitude about $5mm$[49]. For simplicity, all the parameters are assumed to be normally distributed with μ equals to the centroid of the corresponding range and $\sigma = 1$. A total of one hundred random samples were generate, where the respiratory frequency and amplitude of each sample were randomly selected from the normal distribution described.

Meanwhile, another set of Monte Carlo simulations for environmental noise was also performed. This set of simulations assumes that all measurements are conducted on the same person in different environments, which means that the waveform of the vital sign is constant, while the ambient noise is randomly added. The amplitude and frequency of vital signs are specified according to the values used in the mathematical model demonstrated in the Chapter 3, $A_r = 7mm$, $f_r = 0.35Hz$, $A_h = 0.5mm$ and $f_h = 1.2Hz$. The SNRs are taken iteratively from the set A, $A = \{x|0 \le x \le 30, x \in \mathbb{Z}\}$. Under each SNR, 200 sets of radar signals with white Gaussian noise are randomly generated, and the proposed algorithm is applied to them to obtain the average detection accuracy as the final result.

The results for each Monte Carlo simulation will be presented and analyzed in the following sections. Besides, the impact of sleeping posture on the simulation results was also studied and demonstrated.

4.1.1. EVALUATION METRICS

A confusion matrix is a visualization metric of the classification results of a classifier with n classes, which has a dimension of $n \times n$. A typical two-dimension confusion matrix is shown in Figure 4.1. It has two rows and two columns that reports the following meaning[81]:

- TP denotes the number of true positives predictions;
- FP denotes the number of false negatives predictions;
- FN denotes the number of false positives predictions;
- TN denotes the number of true negatives predictions.

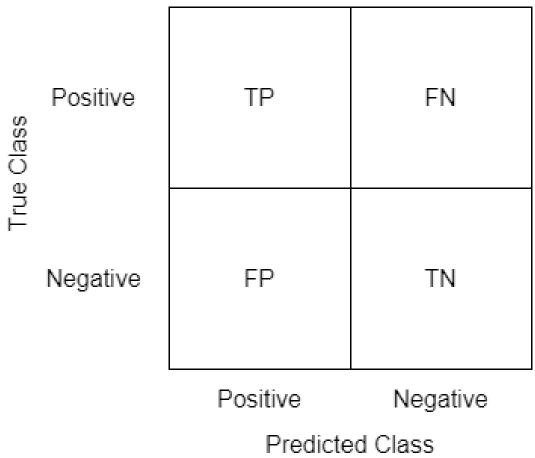

Figure 4.1: Confusion matrix for two-class classification problem.

The evaluation metrics are calculated by:

$$Accuracy = \frac{TP+TN}{TP+FP+FN+TN} \tag{4.1a}$$

$$Precision = \frac{TP}{TP+FP} \tag{4.1b}$$

$$Recall = \frac{TP}{TP+FN} \tag{4.1c}$$

$$F1Score = \frac{2 \times Recall \times Precision}{Recall + Precision} \tag{4.1d}$$

Where accuracy indicates the proportion of the total number of predictions that were correct, precision is a measure of the proportion of positive cases that are recognised properly, reports the percentage of all true positive cases that are correctly detected and F1-Score is the harmonic mean of precision and recall values for a classification problem.

4.2. MONTE CARLO SIMULATION FOR DIFFERENT SUBJECTS

To evaluate the performance of the proposed algorithm, a Monte Carlo simulation is performed to mimic different patients by selecting random combinations of frequency and amplitude for respiration and heartbeat. A hundred sets of data with Normally distributed random amplitude and frequency are generated to simulate the measurements on 100 different person. The STFT together with image processing is used in this case to extract the envelope of the signal. Details of signal processing and apnea detection algorithm are presented in Chapter 3. The simulation was assumed to be in the same environment, where the signal-to-noise ratio was set to 20 dB.

As Table 4.1 shows, the classifiers can provide apnea detection results with sufficient accuracy.

Table 4.1: Apnea Detection Results For 100 Simulated Subjects and 3 Classification Algorithms, SNR = 20dB

Algorithm	**Evaluation Matrices**			
	Accuracy	**Precision**	**Recall**	**F1 Score**
Threshold	97.0%	95.4%	100%	98.0%
KNN	94.0%	91.5%	100%	96.0%
SVM	93.0%	100%	89.2%	94.0%

4.2.1. ERROR ANALYSIS

After analyzing several examples where detection errors occur, it is observed that the cause of detection failures comes from the signal pre-processing step. To approximate the distribution of people's breathing rate in reality, a normal distribution is used in the simulation whose mean is centred in the middle of the range interval, which also means that the modelled signal's frequency will fall outside the regular interval in rare cases.

Figure 4.2 shows the outputs of each step of the signal pre-processing workflow for these examples where errors have occurred. The failure happened because the respiration rate was too high that the time resolution did not meet the requirement of a sound restoration, as could be seen in the plot of spectrogram. Hence, the outcomes of the envelope extraction are somewhat distorted, which further leads to the failure of the modal decomposition. Another reason for detection failure is that the apnea duration is too short, which is also a side effect of excessive frequency. Because the duration of apnea is set to two or three full respiratory cycles in the simulation, the rapid respiratory rate resulting in too short an apnea duration to be detected by the five-second detection window.

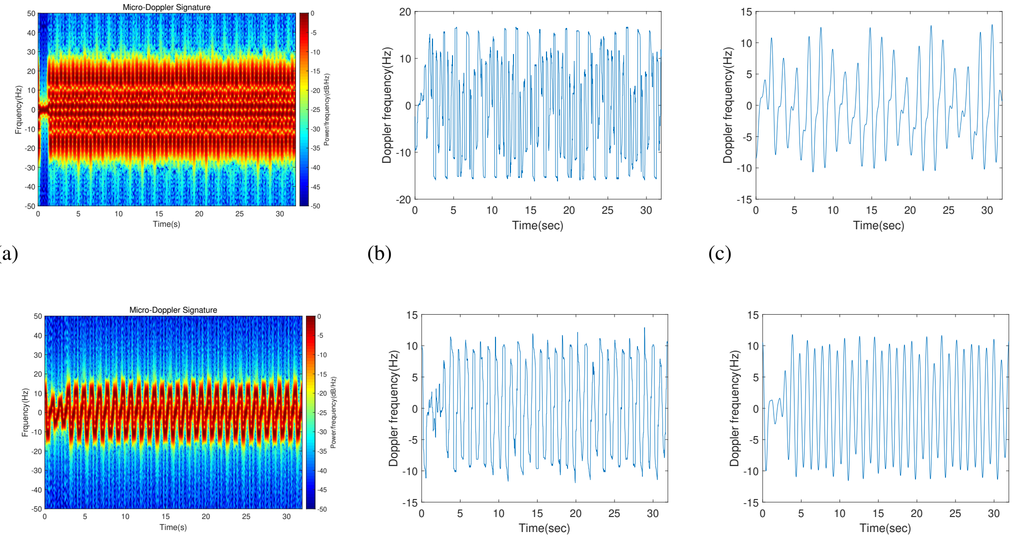

(a) (b) (c)

(d) (e) (f)

Figure 4.2: Results of each step of the signal pre-processing workflow: after STFT (Doppler-time spectrogram pattern) with (a) central sleep apnea and (d) obstructive sleep apnea, after envelope extraction (Doppler frequency vs time pattern) with (b) central sleep apnea and (e) obstructive sleep apnea, after VMD (Doppler frequency vs time pattern) with (c) central sleep apnea and (f) obstructive sleep apnea

However, in reality, breathing signals generally occur at low frequencies, hence such extreme cases do not affect the validity of the algorithm. When a uniformly distributed probability is used to generate the vital signal parameters, which implies that the frequency and amplitude are strictly limited to their range, fresh 420 sets of raw data are generated. The evaluation metrics for this dataset are shown in Table 4.2, where all three classification algorithms achieved nearly 100% accuracy. It is worth noticing that the model used to simulate respiration signal and sleep apnea is a highly idealized model and the signal, in reality, is much more complicated.

4.3. Monte Carlo Simulation for the Environment

Monte Carlo simulations for different environments represented by different signal-to-noise ratio SNR were performed to investigate the robustness of the proposed algorithm. The target was assumed to be the same person, with invariant amplitude and frequency of their vital signs. The signal-to-noise ratio traverses all values from 0 to 30, under which two hundred sets of data are generated and used for follow-up process and classification.

Table 4.2: Apnea Detection Results For 420 Simulated Subjects and 3 Classification Algorithms; Subjects are in supine position and SNR = 20dB

Algorithm	**Evaluation Matrices**			
	Accuracy	**Precision**	**Recall**	**F1 Score**
Threshold	100%	100%	100%	100%
KNN	99.8%	100%	99.8%	99.9%
SVM	100%	100%	100%	100%

4.3.1. RESULT FOR FREQUENCY ESTIMATION

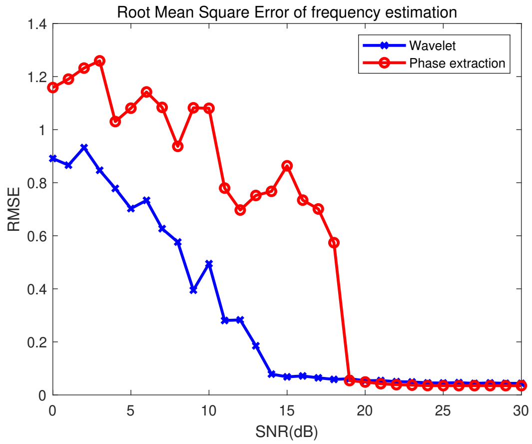

Figure 4.3: RMSE of respiration frequency estimation as a function of SNR for wavelet-based vs phase extraction approaches

Under different SNRs, the comparison between the frequency estimated by the two algorithms and the root mean square error of the true value is shown in Figure 4.3. Both algorithms could provide the estimation of the frequency with sufficient accuracy when SNR larger than a threshold. However, frequency estimation based on wavelet do show more robustness against noise.

4.3.2. SIMULATION IN SUPINE POSITION

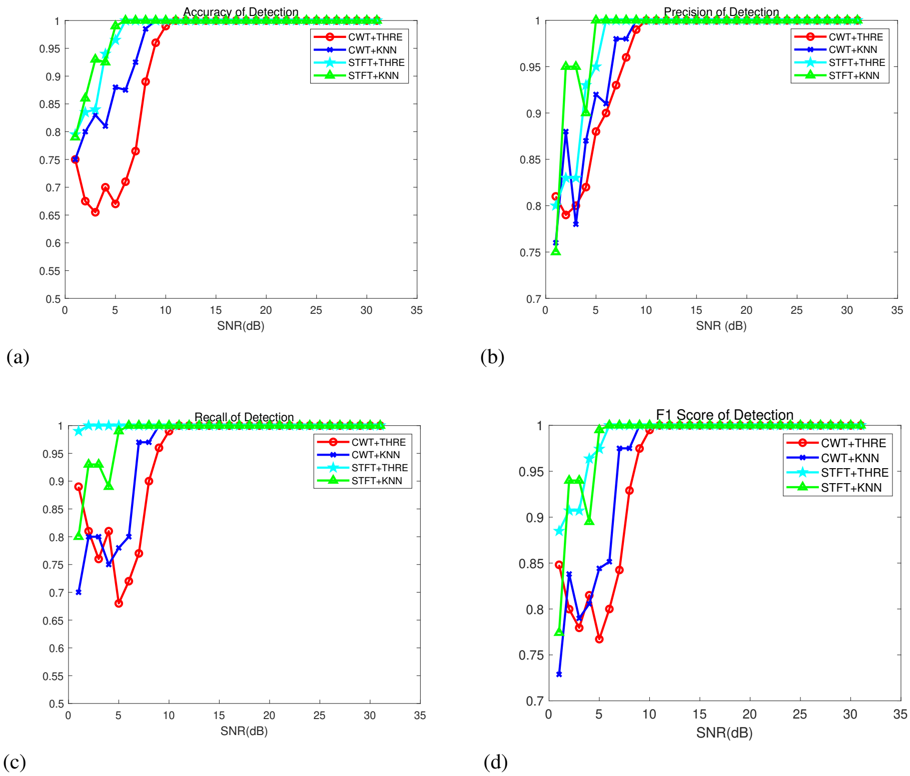

Figure 4.4: Evaluation metrics of Monte Carlo simulation on the environmental noise: (a) Accuracy (b) Precision (c) Recall (d) F1 Score

Figure 4.4 compares the accuracy, precision, recall and F1-score for two time-frequency distributions (the proposed STFT and the CWT for comparison) from which the envelope is extracted, and the usage of KNN classifier vs a simple amplitude threshold. STFT yields better results than CWT for lower SNR values, while in general results are above 70%. The difference between KNN vs simple detection threshold appears to be not too relevant.

4.3.3. SIMULATION FOR DIFFERENT SLEEPING POSTURE

To investigate the impact of sleeping posture on apnea detection, a model that simulates the radar echo at the chest wall was built, in which an ellipsoid is used to model the human torso. As shown in Figure 4.5, assume that the target lies on the xOy plane along the y axis, and the radar is placed at $(0,0,0.6)$. In general, a, b, c are taken as 0.15, 0.3, 0.1 respectively. These data are from one of the subjects in the subsequent experimental procedure who has a relatively small torso. However, this will not have an impact on the simulation results as the simulation is designed to capture the differences in sleep positions. Using the concept

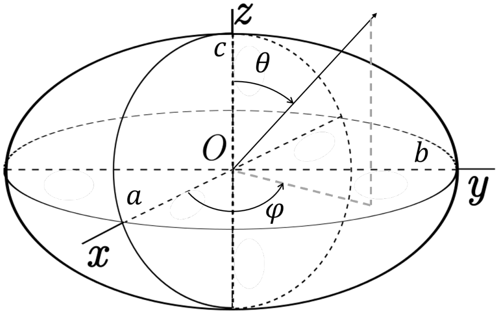

Figure 4.5: Ellipsoid geometry used to model human torso; target lies on the xOy plane along the y axis

of relative coordinates, the motion of the target turning over is equivalent to object keeping still and the radar rotating around the target. Under this condition, the equivalent radar cross section of the torso is defined as:

$$\sigma = \frac{\pi a^2 b^2 c^2}{\left(a^2 \sin^2\theta \cos^2\phi + b^2 \sin^2\theta \sin^2\phi + c^2 \cos^2\theta\right)^2} \tag{4.2}$$

Where (θ, ϕ) are $(0, \frac{\pi}{2})$, $(\frac{\pi}{2}, 0)$ and $(\pi, \frac{\pi}{2})$ for supine, side and prone position, respectively.

The modeling and simulation of signals for different sleeping positions are based on the following assumptions:

1. The physiological characteristics of breathing as well as heart rate do not change when the target is in different sleeping positions. This is a rather idealistic assumption, since studies have shown that the frequency of breathing as well as pulmonary ventilation and even respiratory abnormalities are associated with the sleep position[82][83][84]. Nonetheless, this correlation revealed very complex features, and no mathematical model has been proposed that can well simulate this alteration. Consequently, in this simulations, the changes in the physiological properties of breathing are ignored.

2. The ellipsoidal model mentioned above is applied to simulate the human torso, and the calculation of the radar scattering cross section is solely based on this assumption, which means that the influence of the limbs is neglected.

3. For reasons of simplicity and based on the research on "Effects of posture on chest-wall configuration and motion during tidal breathing" [84], the Anteroposterior (AP) diameter changes at the thorax in different sleeping positions was set quantitatively to $AP_{supine} : AP_{side} : AP_{prone} = 1 : 0.7 : 0.3$, $AP_{supine} = 0.7mm$.

This simulation does not fully reproduce the actual sleep situation, but only gives a reference for the analysis of the accuracy of sleep apnea detection with respect to the torso radar scattering cross section and skin surface displacement.

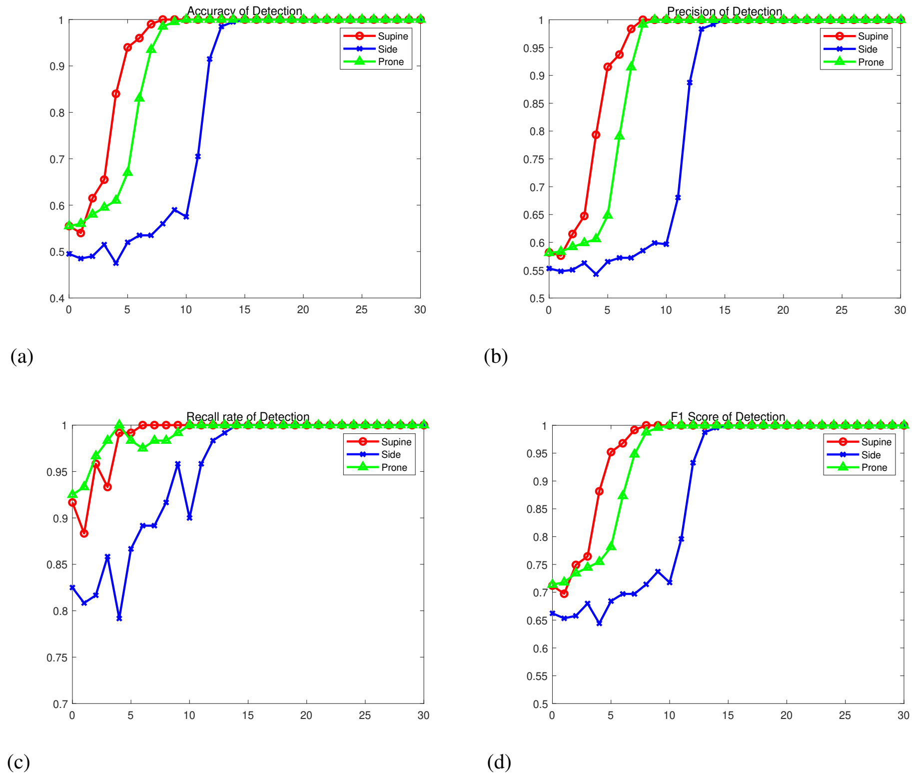

Figure 4.6: Evaluation metrics of Monte Carlo simulation on the environmental noise in different sleeping posture: (a) Accuracy (b) Precision (c) Recall (d) F1 Score

Figure 4.6 shows the Monte Carlo simulation results for the ambient noise when the target is in different poses. Following observation can be made:

1. The supine state has the highest detection accuracy, followed by prone and then side-lying.

2. In the supine and prone position, the radar cross section is larger, resulting in a higher reflected signal energy, which contributes to its robustness to noise.

3. Comparing the results for supine and prone, it can be concluded that the reduction of displacement amplitude doesn't have much effect on the results due to the sufficient Doppler resolution in the simulation.

4. As the signal in the simulation environment is relatively ideal and the high-resolution setting, the algorithm can achieve 100% detection accuracy in all three sleeping postures when the signal-to-noise level is above a certain threshold.

4.3.4. ERROR ANALYSIS

Figure 4.7 demonstrates the signal reduction for some examples where detection errors occurred. It can be seen that, as in the Monte Carlo simulation for patients, the problem lies mainly in the signal pre-processing procedure, where the signal is masked under the white noise in many simulations due to the very low signal-to-noise ratio. (In some cases the signal can still be restored, as shown in Section 3.2.5 in Chapter 3.)

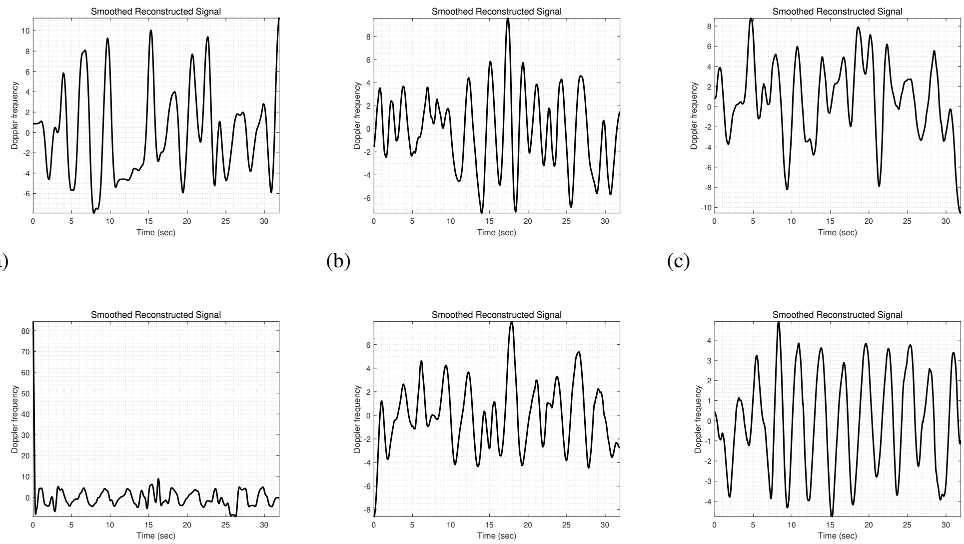

(a) (b) (c)

(d) (e) (f)

Figure 4.7: Examples of detection errors, i.e. patterns that are incorrectly recognised by the classification algorithms: for SNR = 0 dB (a) normal breath (b) CSA (c) OSA, and for SNR = 3 dB (d) normal breath (e) CSA (f) OSA

After the analysis of the error cases, the following findings can be obtained:

1. The effect of noise is mainly reflected in the signal amplitude;
2. Under a fixed signal-to-noise ratio, since the noise is randomly added, its influence on the detection result is unpredictable;
3. The proposed algorithm tends to generate false alarms at low SNRs instead of miss detection.

4.4. CONCLUSION

This chapter presents the results of Monte Carlo simulations for noise and vital signal parameters; different sleep positions are taken into account and error studies are performed. It is verified that the proposed pre-processing algorithms can restore the signal well except for extreme cases and cases where the $SNR < 5dB$. The obtained signal envelopes are also very effective as features for respiratory obstruction detection, and all three applied classification algorithms can obtain an accuracy rate of more than 90%. Simulations on sleeping posture point out that the RCS (which is directly related to the received signal energy) is the most critical factor in determining the detection effectiveness in a low SNR environment. However, this simulation is based on the premise that the signal model is highly idealized and the sleeping posture is highly standardized. It only provides a reference for analyzing the accuracy of sleep apnea detection from the torso RCS and skin surface displacement. The relationship between the real situation for sleeping posture and radar-based breathing obstruction detection will be characterised more in detail in the next chapter using experimental data.

5

Experimental validation

An experiment on 14 participants was conducted to verify the effectiveness of the proposed system and pre-processing and apnea detection algorithms illustrated in Chapter 3. This chapter will present the experimental procedure, measured data composition, and signal processing and apnea detection results, followed by some comments and discussion. Ethics approval for the research was provided by the Delft University of Technology Ethics Committee and written informed consent was obtained from each subject.

5.1. Experimental Environment Setup

The experiment took place in a project room at Delft University of Technology. As shown in Figure 5.1, the yoga mat was placed on an open area of the floor and the radar was fixed to the edge of the table. The subjects were asked to lie on the yoga mat with a pillow, and the radar was placed 110 cm directly above their chest. There was no obstruction between the subjects and the radar.

The radar used in this experiment is the Xethru X4M03 low power UWB module, which combining a 7.29/8.748 GHz transmitter with 1.5 GHz bandwidth. Coherent integration was used to achieve processing gain and the level of processing gain increase with higher integration. The sampling rate is 23.328 GS/s and the Pulse Repetition Frequency (PRF) is 100 Hz.

The subjects included 14 volunteers aged 22-35, 10 of whom were males and 4 were females. Their breathing was measured in the supine, side and prone positions. Note that these volunteers are not actual patients who suffer from obstructive sleep apnea, but healthy people. Thus the apnea events were simulated by the subjects holding their breath. And then the above measurements were repeated while the subjects were covered by a blanket. Lying in each position, they were asked first to breathe normally and then to hold their breath for several seconds. The simulated respiratory interruption generally lasted between ten and twenty seconds on average. Note that even if the experiment is not for true apnea, what we aimed for was to capture transitions between normal and holding. During the measurement, the participants were told to be as natural as possible, to be as they usually do when they sleep. For example, when lying on their side, their bodies are naturally curled up, and their arms are relaxed.

The composition of the experimental data is shown in the Table5.1. A total of 365 sets of data were measured, of which 181 sets were normal breathing and 184 were sleep apnea cases (simulated by subjects holding breath for more than 10s). The duration of each set of recordings is 40 s. Note that during these 365 sets of measurements, the subjects were asked to stay as still as possible and could not make movements such as turning over. Apart from this, we also conducted 23 sets of measurements during which the participants were allowed to change the sleeping position to study the feasibility of breathing monitoring when the subject is moving.

Figure 5.1: Picture of the experimental setup with radar in the red circle; the subject is lying on his side

Table 5.1: Experimental Data Composition; Units in the table: number of data collection

	Sleeping Position			Total
	Supine	Side	Prone	
Blanket	56	68	56	180
No Blanket	56	71	58	185
Total	112	139	114	365

In addition, a set of control experiments were carried out. As in the previous experiment, we measured the subjects' breathing in the supine, side and prone positions with and without the blanket. In this experiment, the only difference will be that the participant was

5

also wearing breathing belts to monitor his respiration while being measured by radar. This set of control data is used to verify the effectiveness of our algorithm against the measured data. Thus the algorithm can be appropriately improved according to the results.

Finally, we also performed respiration monitoring for one hour in an actual sleeping scenario on one of the subjects. During the test, the subject was lying on the bed and covered with a quilt, and the radar was placed 70 cm above the chest.

5.2. PRE-PROCESSING RESULTS

5.2.1. SIGNAL RECONSTRUCTED BY PHASE DEMODULATION

In Chapter 4 we verified the effectiveness of the signal processing algorithms by simulation data and perform Monte Carlo simulation for the noise level. The results indicated that in the case of a high signal-to-noise ratio (SNR> 20 dB), the phase extraction and Doppler frequency-based signal reconstruction are both reliable.

However, after processing and analyzing the experimental data, we found that phase demodulation does not always provide accurate results in this experimental environment. Phase demodulation for UWB radar is performed on slow time. The phase history demodulated from two sets of the radar signal, and the corresponding ground truth gathered by respiration belt was demonstrated in Figure 5.2. The trajectory extracted by the phase demodulation algorithm described in previous chapter is shown in Figure 5.2a and 5.2b, where Figure 5.2a demonstrates normal breathing and Figure 5.2b demonstrates apnea.

We could observe that the phase trajectories have an overall upward trend, which is inconsistent with the record measured by the breathing belt. After analyzing the extracted phase, it is discovered that this happens because the phase compensation is performed at the wrong phase discontinuity point. The phase demodulation process involves a process of compensating 2π when the phase suddenly changes more than an entire period. However, when an aberrant phase jump occurs, an error occurs in the result of phase demodulation. The appearance of anomalous phase jumps is related to noise, the initial phase of the pulse and relatively low PRF. We take the scenario of apnea depicted in Figure 5.2b as an example; at the points of time marked by the labels, there was an unexpected sudden change in the phase, which led to the failure of the demodulation algorithm. Unexpected phase discontinuities are usually caused by noise and low sampling frequency, especially when the respiratory signal is weak.

To solve this problem, we skipped the phase compensation step and repeat the demodulation operation. Therefore we reached the results shown in Figure 5.2c and 5.2d, which have shown consistency with the ground truth. However, the chest wall displacement caused by cardiopulmonary activity usually lies in the interval of $[4mm, 12mm]$ (supine position)[48]. According to Equation 2.31, the maximum phase shift caused by the chest wall movement to the UWB radar signal will be from 1.2 rad to 4.4 rad. Combining the initial phase, it may easily lie outside the interval of $[-\pi, \pi]$. Skipping unwrap procedure may sometimes causes the upwrapping failure at the normal phase jump that should be phase compensated. Examples are shown in Figure 5.3. In these two cases, the effectiveness of the two phase demodulation methods is completely opposite to that of the previous examples.

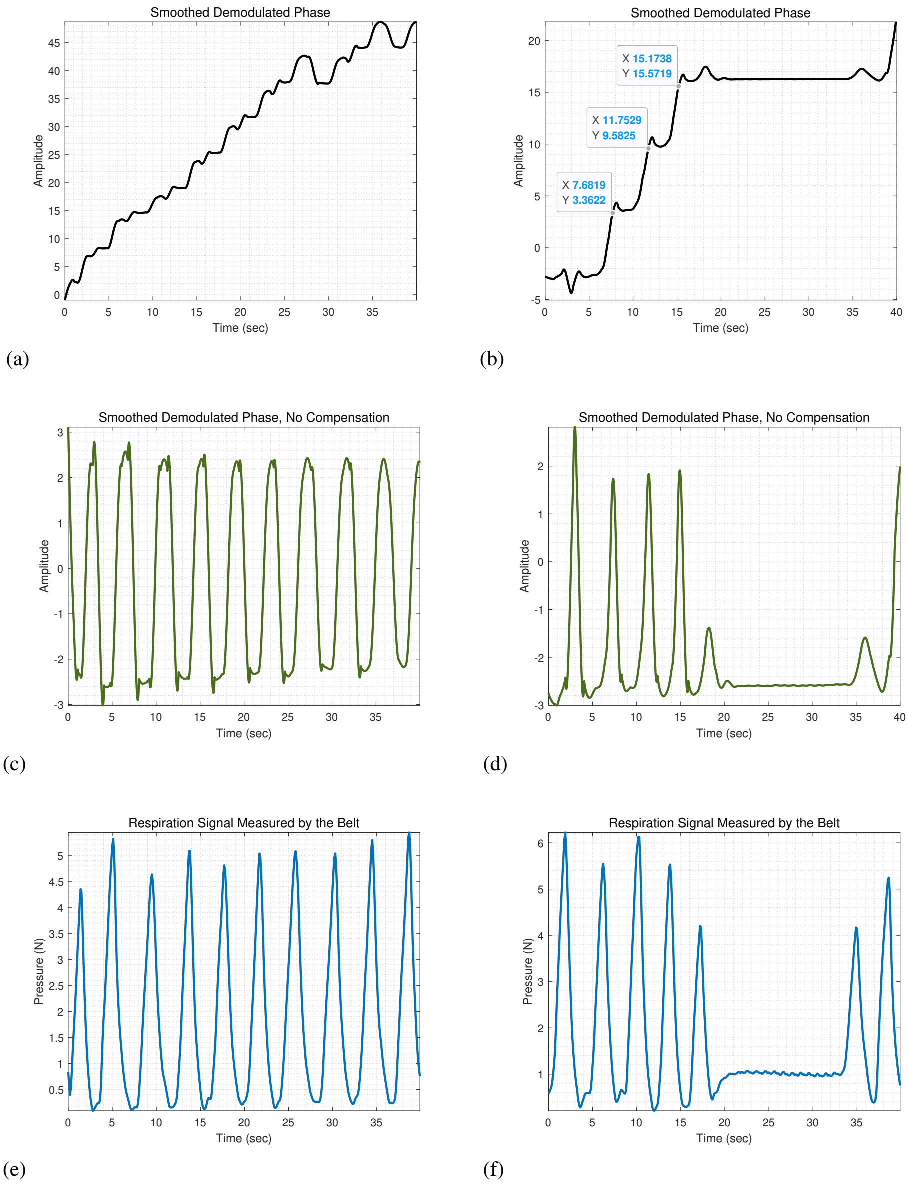

Figure 5.2: Phase demodulation results: normal breathing in supine position for phase demodulation with unwrap process (a) phase demodulation without unwrap process (c) and ground truth (e), and holding breath episode in supine position for phase demodulation with unwrap process (b) phase demodulation without unwrap process (d) and ground truth (f)

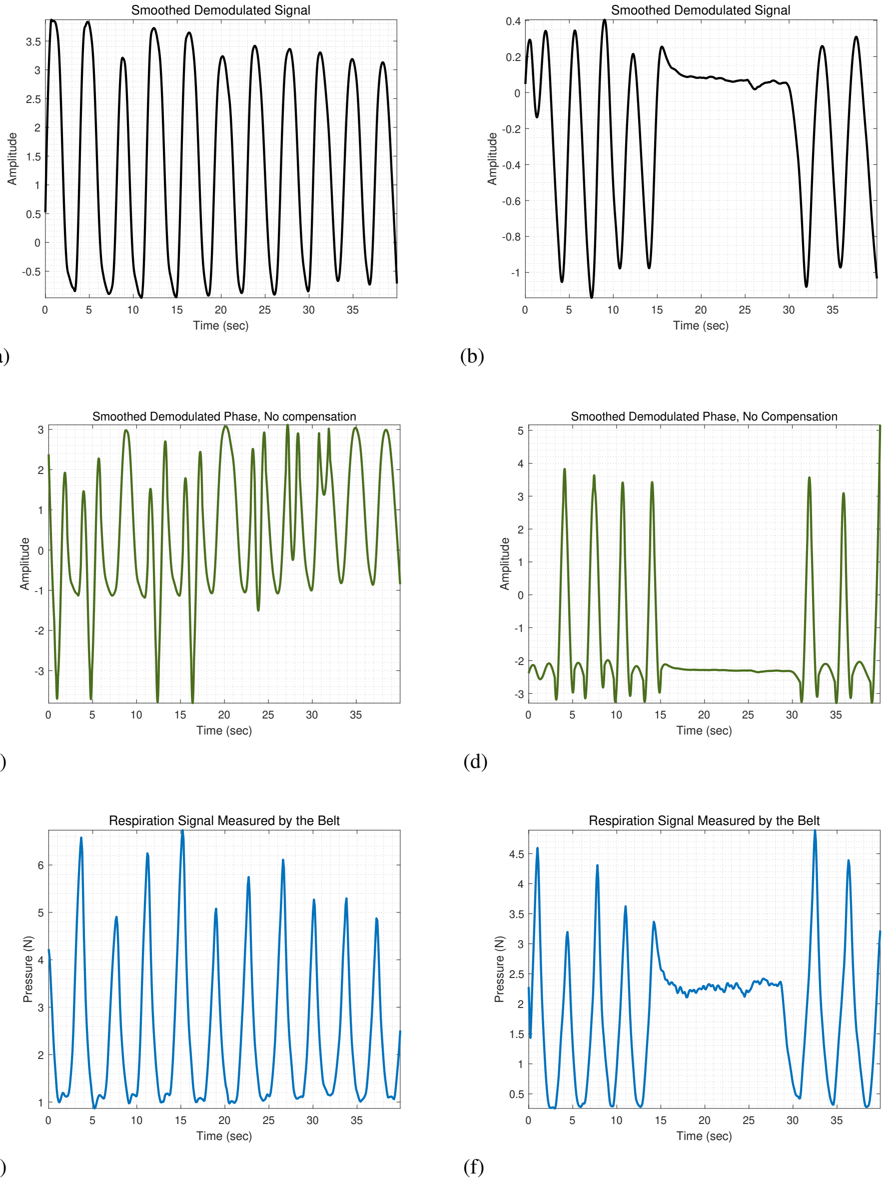

Figure 5.3: Phase demodulation results: normal breathing in side position for phase demodulation with unwrap process (a) phase demodulation without unwrap process (c) and ground truth (e), and holding breath episode in side position for phase demodulation with unwrap process (b) phase demodulation without unwrap process (d) and ground truth (f)

A conclusion could be drown that the modified approach to deal with compensation in experimental data works for the majority of the cases and allowed us to get good results.

However, in some cases the compensation produces phase errors that still remains to be fixed.

5.2.2. Signal Reconstructed by Short-time Fourier Transform

After investigating the performance of the phase demodulation on all the reference data, the conclusion that the signal phase is not robust to noise has been verified. The noise that appears at certain times can sometimes have a fatal effect on the phase. In contrast, we have validated in Chapter 3 that the signal spectrum is more robust to noise. The Doppler-time plot corresponding to the above four records can be seen in Figure 5.4. Figure 5.4a and 5.4c illustrate examples of normal breathing in supine and lateral recumbency respectively. Figure 5.4b and 5.4d show the sleep apnea in supine and side position, where sleep apnea were present in the (20s,35s) and (16s,31s) time intervals respectively.

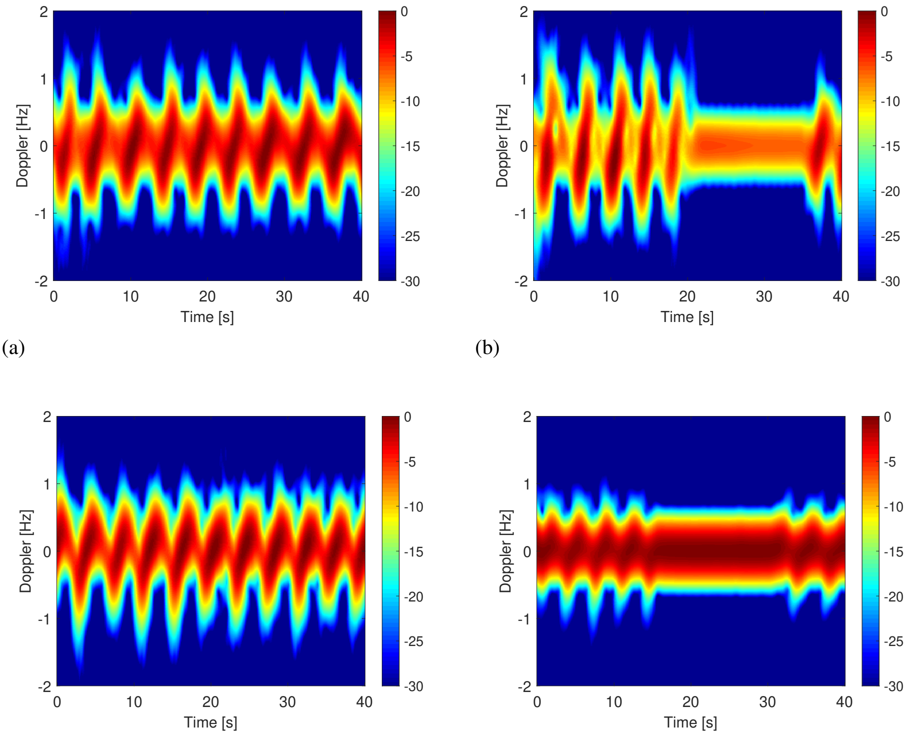

(a) (b) (c) (d)

Figure 5.4: Spectrogram for: normal breath in supine position (a), holding breath episode in supine position (b), normal breath in side position (c) and holding breath episode in side position (d)

Then we have studied the performance of short-time Fourier transform applied to all control data sets. It turns that spectrogram could be considered a dependable signal restoration method. The chest movement is captured by the radar spectrograms; however, due to the limitation of frequency resolution, the difference between the spectrogram of normal breath and sleep apnea (simulated by holding breath) is not so apparent that classifiers can easily distinguish it. An image processing algorithm is then applied to find the pixels with the highest red saturation in the image to extract the envelope. The reconstructed envelope is then processed for noise reduction and smoothing via VMD, whose explanatory introduction was presented in Chapter 3. The outcomes of this series of operations and their comparison with the ground truth measured by the breathing belt will be elaborated in Section 5.2.4.

5.2.3. SIGNAL RECONSTRUCTED BY DISCRETE WAVELET TRANSFORM

The signal decomposition result of reference experimental data could be seen in Figure 5.4. When configuring the radar, PRF is set to 100 Hz. Thus the respiration component will be extracted in the $8-th$ level, and its waveform is marked in red.

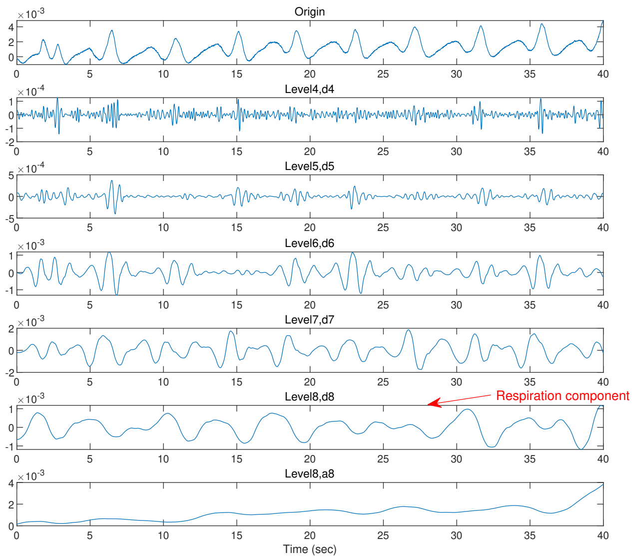

(a)

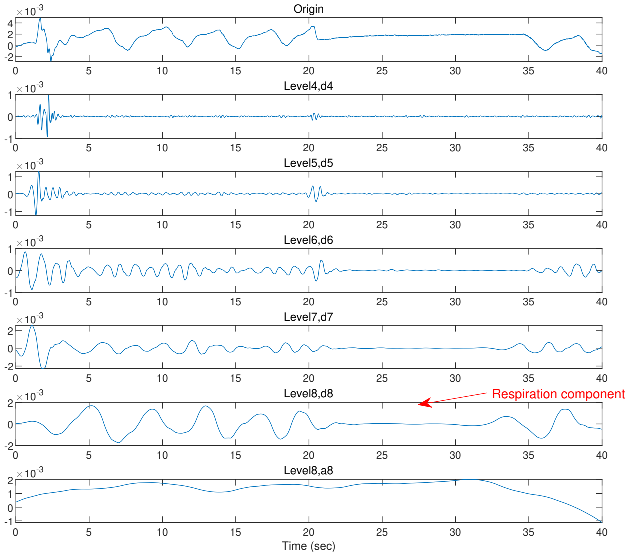

(b)

Figure 5.4: Wavelet decomposition (a) normal breath in supine position (b) apnea in supine position

5.2.4. COMPARISON WITH MEASUREMENTS OF RESPIRATION BELT

First, the respiration signal waveforms extracted by the proposed algorithm are compared with those derived from simultaneous measurements with a reference respiration belt. The belt uses a force sensor to measure respiratory event and breathing rate, which is secured to the subject's chest by a nylon strap. It has a resolution of 0.01 N and a response time of 50 ms. The respiration rate was calculated every 30 s with an advance interval of 10 s[85].

Figure 5.5: Picture of the Go Direct Respiration Belt product

The belt used for comparison is Go Direct Respiration Belt whose schematic diagram could be seen in Figure 5.5. In operation, the sensor is fixed to the chest by means of a nylon strap and the data is transmitted to the computer via Bluetooth.

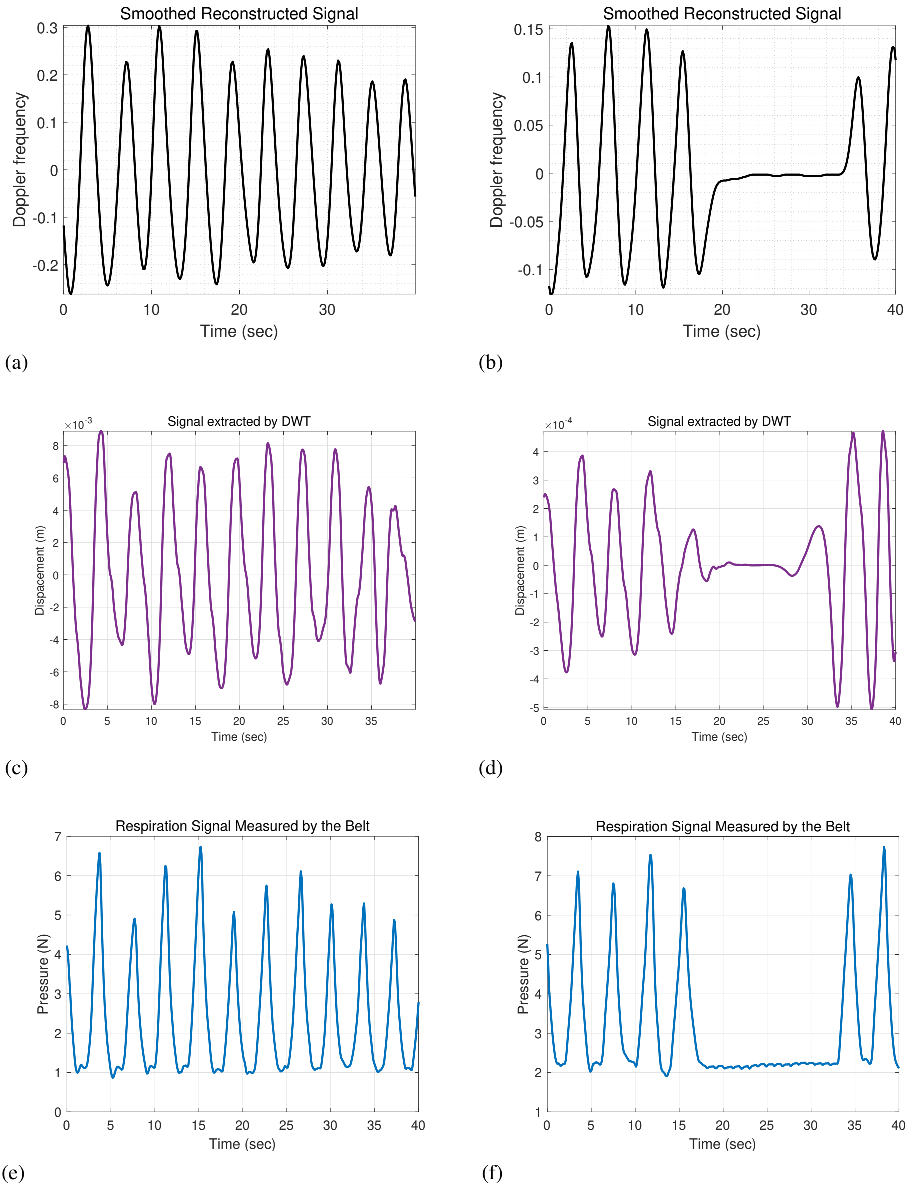

Figure 5.6: Waveform comparison radar vs reference respiration belt: normal breathing in side position for radar based on STFT (a) DWT (c) and for belt (e), and holding breath episode in prone position for radar based on STFT (b) DWT (d) and for belt (f)

Figure 5.6 demonstrate the breathing signal captured by the radar and the respiration belt, respectively, for normal breathing in the side-lying position and breath-holding in the prone position. It could be easily observed that, except for a time lag of about 1 second, the waveforms are consistent. The existence of time lag is due to the limitation of the experimental environment: the radar and the respiration belt are manually synchronized, and the respiration belt has a response time of 50ms.

As shown in Figure 5.7, breathing frequencies estimated by our algorithm for these two sets of data are 0.25 Hz and 0.24 Hz respectively, while the respiration rates measured by the belt are 15.8 bpm (0.27 Hz) and 15.5 bpm (0.26 Hz). The overall RMSE of the estimated frequency for the twenty control experiments compared to the reference respiratory belt data is 0.018 Hz. It turns out that the error is considerably small; thus we can get to the conclusion that the radar could provide us reliable vital sign monitoring result.

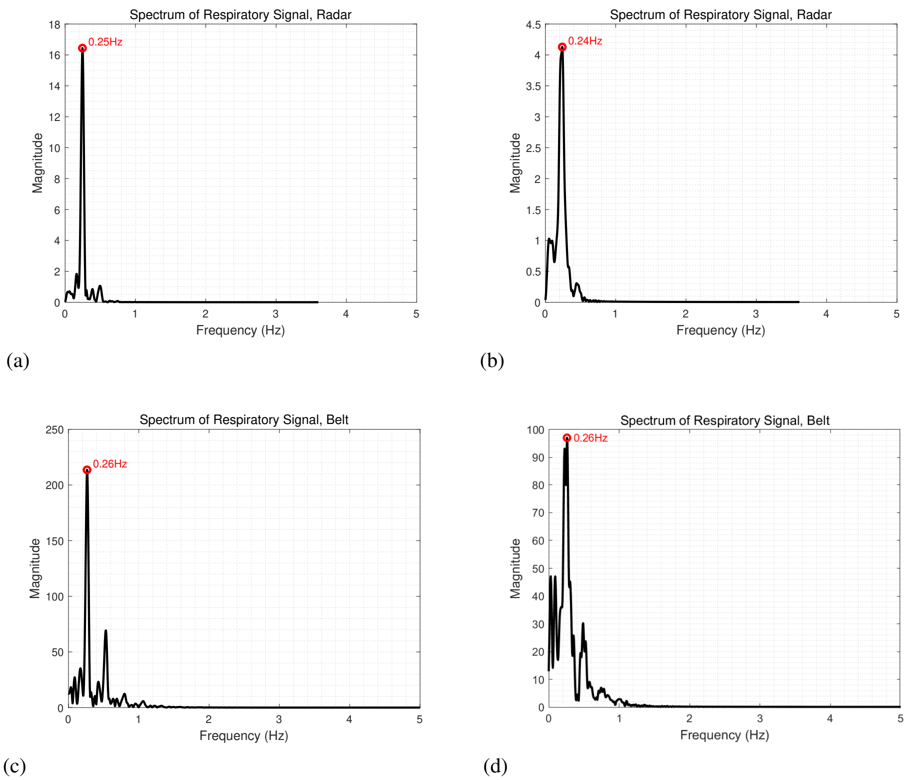

Figure 5.7: Spectrum comparison radar vs reference respiration belt: normal breathing in side position for radar (a) and belt (c), and holding breath episode in prone position for radar (b) and belt (d)

After comparing the respiratory waveforms reconstructed by the three signal pre-processing algorithms and the results measured with the belt, it can be observed that the outcomes of phase extraction are not always reliable. In contrast, both the short-time Fourier transform and the discrete wavelet transform could provide solid signal reconstruction results. Therefore, in the following section, the verification of the apnea algorithm is based on the signals obtained by STFT and DWT.

5.3. APNEA DETECTION RESULTS

5.3.1. APNEA DETECTION RESULTS FOR ALL THE EXPERIMENTAL DATA

According to the standard for sleep apnea detection introduced by the American Academy of Sleep Medicine (AASM), apnea is reported when there is a drop of more than 90% in the signal amplitude of the baseline for at least 10 seconds [79]. Based on this criterion, a method that detects apnea by setting a threshold of 90% drop in average amplitude is proposed. Because holding breath was used to simulate sleep apnea, respiration obstruction in our case can be considered central sleep apnea, manifested by the absence of chest wall displacement caused by breathing. Therefore, we set the signal amplitude threshold for judging respiratory obstruction to 10% of the benchmark.

Based on the threshold method, the results of respiratory obstruction detection on waveforms restored by different signal pre-processing methods are studied. The evaluation metrics are shown in Table 5.2. The result turns out signals restored by spectrogram provides stronger evidence for apnea detection. Therefore the exploration of machine learning classifiers is based on the results of spectrogram and image processing.

Table 5.2: Apnea Detection Results Based on Threshold For The Entire Experimental Dataset

Pre-processing Algorithm	Evaluation Matrices			
	Accuracy	Precision	Recall	F1 Score
Spectrogram	89.3%	89.6%	89.1%	89.3%
Discrete Wavelet Transform	86.0%	81.8%	92.9%	87.0%

When machine learning algorithms were applied, the proportion of the training set is set to 80% of all experimental data, and the remaining 20% is used for testing. For both KNN and SVM, holdout validation has been applied, the training was repeated six times according to the division ratio of training set: test set = 8:2 and the values of accuracy, precision, recall and F1 score are obtained by calculating the average. In terms of precision, recall and F1 score, we take their weighted average as the final values, which is, to calculate metrics for each label and find their average, weighted by support (the number of valid instances for each label). This calculation procedure takes the imbalance of labels into account, making changes to the data set at a macro level; as a result, it may result in F1 scores that are outside the range of precision and recall.

The apnea detection results for the entire experimental data set are shown in Table 5.3. Based on the signal reconstructed by the proposed algorithm, both classification methods with and without machine learning can provide compelling apnea detection results, with accuracy, precision, recall and F1 score all about 90%. Among these three classifiers (i.e. simple threshold, KNN, and SVM), KNN has the best classification performance. However, the performance of SVM is generally better than KNN. This might be because KNN is a lazy algorithm that hardly relies on statistics and comparisons. It's a non-sparse model that must track many features and use all training samples to obtain a prediction, while SVM aims to find the optimal hyperplane depending on the training set. After determining an equation that separates the two categories, the forecast is entirely based on this equation. We summarized several reasons why KNN performed better than SVM:

- The size of our data set is relatively small, which limits the search for the optimal hyperplane; however, KNN considers every samples when making decision, a relatively small data set will not be a problem.

- With an increasing number of features, the clearer optimal hyperplane could be obtained. SVM generally shows superiority when dealing with the high-dimensional problem, whereas the KNN tends to perform a bit degraded. We only used one feature, the signal envelope, to train the model, which results in SVM losing its superiority.

The algorithm proposed in [12] by Koda et al. in 2021 was also applied on the experimental data to compare the results. In their study, they also processed radar data with STFT; however, instead of extracting the envelope, they directly used the down-sampled images (20×30 pixels) of the spectrogram, which were then converted to 600×1 vectors, to train the SVM classifier. In this paper, the dimension of down-sampled spectrogram images is 27×36 as the original spectrograms had larger size.

The classification results are shown in Table 5.3, labelled as "Koda's algorithm". This method achieved an accuracy of about 80%. As discussed in chapter 3, the quality of the spectrogram was limited by resolution and existence of static clutter. A modification of their algorithm is also proposed, by adding a moving target indication filter to their signal processing pipeline. This improved the classification accuracy by approximately 10%, even if the results with the proposed envelope-based algorithm are still higher.

Table 5.3: Apnea Detection Results For The Entire Experimental Dataset

Apnea Detection Algorithm	Evaluation Matrices			
	Accuracy	Precision	Recall	F1 Score
Threshold	89.3%	89.6%	89.1%	89.3%
KNN	90.1%	91.0%	90.0%	90.0%
SVM	87.7%	89.3%	89.0%	89.0%
Koda's algorithm[12]	78.6%	78.5%	77.8%	76.7%
Koda's algorithm with MTI	87.6%	87.2%	87.3%	87.2%

5.3.2. APNEA DETECTION RESULTS FOR DIFFERENT SLEEPING POSTURES

Differences in sleeping postures in terms of apnea detection were also investigated, with results reported in Table 5.4. The best classification results were obtained for supine position, followed by side and prone positions. This is due to the differences in amplitude of the recorded respiration signal, the highest in supine position, followed by side and prone positions, due to the different extent of the chest and thorax movements. Noticeable variations of the signal levels and classification performance can be seen for different individuals, for example the effect of arm posture while in side position, as the arm and elbow over the chest can partially obscure the relevant movement. Note that Koda's algorithm [12] appears to be rather robust to differences in sleeping postures.

Table 5.4: Apnea Detection Experimental Results for Different Positions

Proposed Algorithm	**Accuracy**		
	Supine	**Side**	**Prone**
Threshold	98.2%	90.6%	78.9%
KNN	96.2%	90.5%	85.9%
SVM	90.3%	87.5%	81.2%
Koda's algorithm[12]	80.8%	71.5%	70.6%
Koda's algorithm with MTI	86.7%	86.9%	86.4%

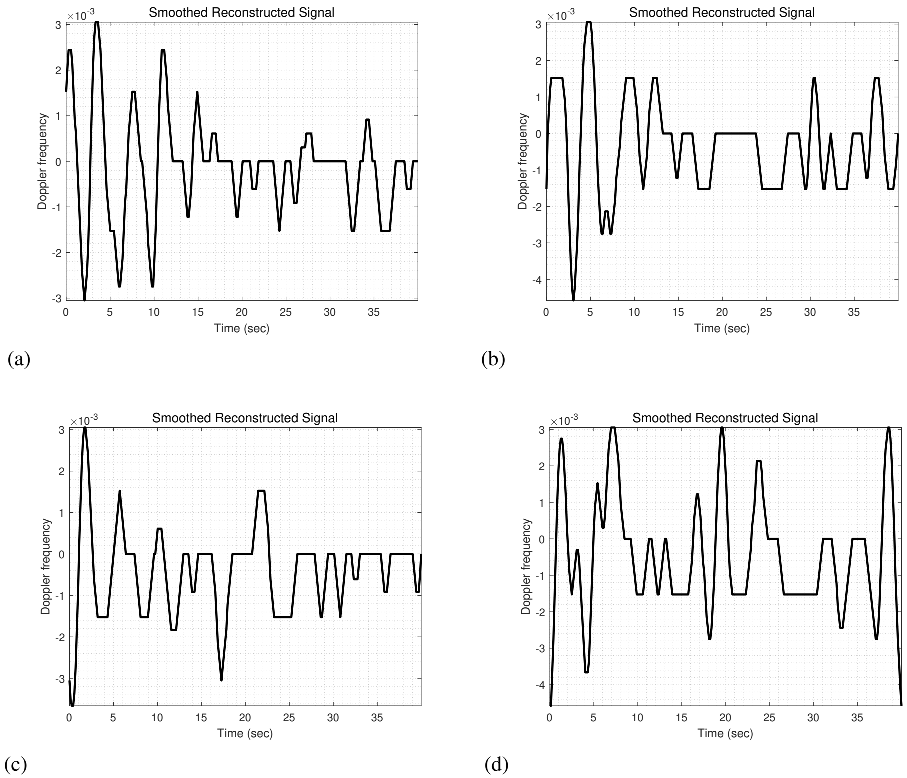

Figure 5.8: Signal reconstructed for Target 2 in prone position: normal breathing in prone position without blanket (a) with a blanket (c), and holding breath episode in prone position without blanket (b) with a blanket (d)

After analyzing the samples with errors in the detection of respiratory obstruction in each sleeping position, we have the following observations:

- For most of the participants, the recorded respiration signal shows a significant distinction in amplitude, the highest in supine position, followed by side and prone positions, $Amplitude_{supine} > Amplitude_{side} > Amplitude_{prone}$; this is due to the different extent of the chest and thorax movements. Due to the limitation of Doppler frequency resolution, the smaller the amplitude, the more challenging it is to reconstruct perfectly, which results in a higher possibility of classification failure. For target 2, the error of apnea detection only happens when she was lying on her belly. The restored signals measured in the prone position are as shown in Figure 5.8. It can be easily observed that the critical information to distinguish normal breath and sleep apnea is completely lost.
- The impact of side and prone position on accuracy varies greatly among individuals. However, after studying their relative position to radar, the inaccurate for side position could attribute to the posture of the target. For example, some people are more used to put their elbow on the chest and turn the torso slightly towards the ground. For instance, error of detection happens mostly when target 6 is in side position. As shown in Figure 5.9, normal respiration episodes are obscured. In contrast, the error in prone position is usually caused by the physical factor, that is, $Amplitude_{prone}$ is generally smaller.

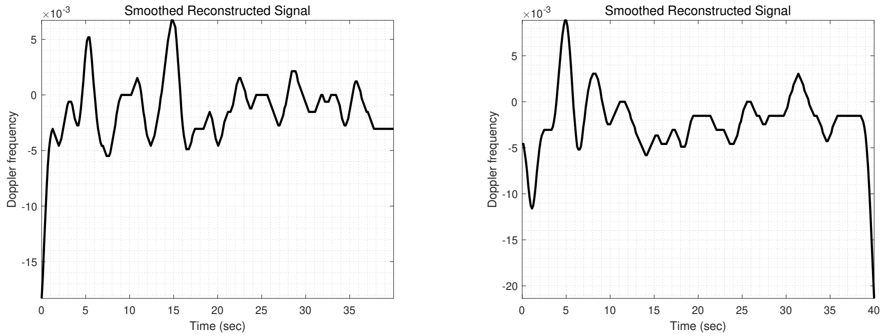

(a) (b)

Figure 5.9: Signal reconstructed for Target 6 in side position: holding breath episode in prone position without blanket (a) with a blanket (b)

For most of the participants, E.g. For target-2, error of apnea detection only happens when she was in prone position The impact of side and prone position on accuracy varies greatly among individuals. E.g. For target-6, error of detection happens mostly on side position. However, after studying their relative position to radar, the inaccurate for side position could attribute to the posture of the target. For example, some people are more used to put their elbow on the chest and turn the torso slightly towards the ground. In contrast, the error in prone position is usually caused by the “physical factor”, that is, a much smaller chest wall displacement.

5.3.3. APNEA DETECTION RESULTS VERSUS EXISTENCE OF BLANKET

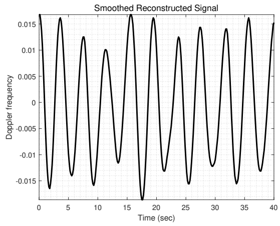

(a)

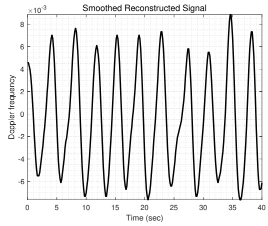

(b)

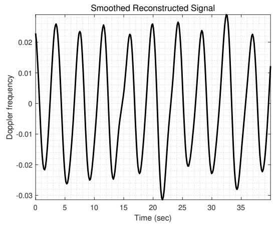

(c)

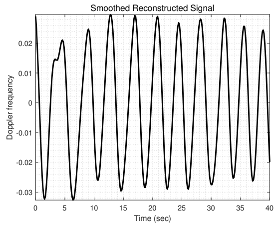

(d)

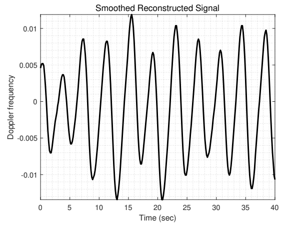

(e)

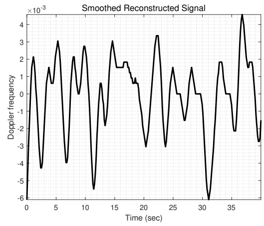

(f)

Figure 5.10: Reconstructed signal for Target 1: normal breathing in supine position (a) side position (b) prone position (c) without blanket, and normal breathing in supine position (d) side position (e) and prone position with a blanket

Table 5.5: Apnea Detection Results versus Blanket

	Accuracy	Precision	Recall	F1 Score
Blanket	88.9%	91.6%	85.4%	88.4%
No Blanket	89.7%	88.0%	92.6%	90.2%

The restored respiration signals for target 1 are demonstrated above in Figure 5.10, the presence of blanket did not show much difference. We could see the result when target was lying in his belly under a blanket is slightly distorted; however, after further study, this could attribute to the influence of position instead of the blanket.

5.3.4. RESULTS VERSUS GENDER

The impact on sleep apnea classification of participants’ gender was also investigated. No significant trend was observed with very similar evaluation matrix obtained for this comparison.

Table 5.6: Apnea Detection Results versus Gender

	Accuracy	Precision	Recall	F1 Score
Male	89.6%	91.1%	87.9%	89.5%
Female	88.1%	87.3%	89.8%	88.5%

5.4. NON-IDEALITY OF EXPERIMENT

Our experimental environment is not ideal, there are some unexpected factors that will affect the results of the experiment, such as the slight vibration of the radar during the measurement and the failure of the subject to simulate respiratory obstruction. In this section we will explain what causes these factors and study their impact on the results.

5.4.1. VIBRATION OF THE RADAR

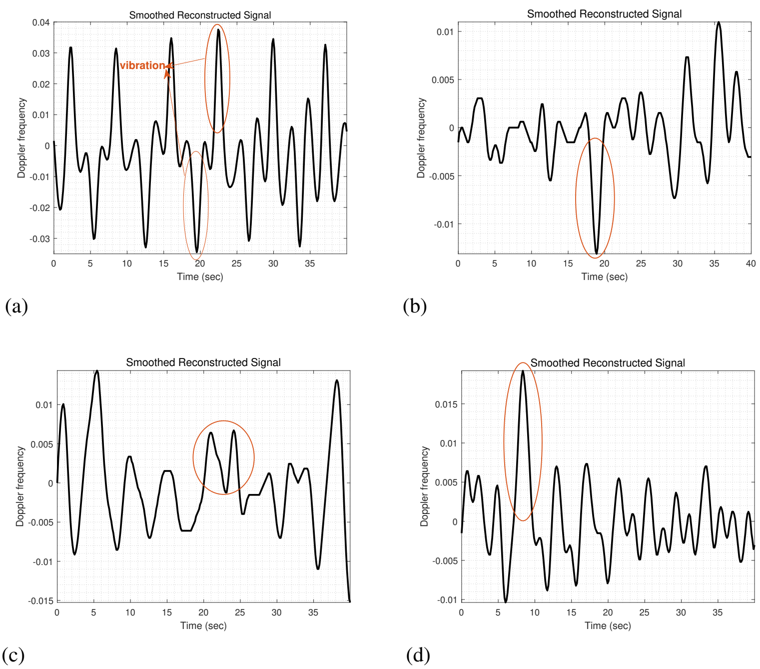

Figure 5.11: Examples of the effects on signal processing caused by radar vibration: target in supine normal without blanket (a) supine apnea with a blanket (b) prone apnea without blanket (c) side normal without blanket(d)

During the measurement, the radar should have been stationary; however, sometimes, slight vibration of the desk caused by a sudden hit or typing will make the radar slightly vibrates, which will add additional movement to the signal.

Figure 5.11 shows several typical examples of the effects on signal processing caused by radar vibration. As shown in Figure 5.11a, during this measurement on one of the participants breathing normally in the supine position, the radar jitter was caused by the recorder typing on the computer. This disturbance lasted for the entire measurement time (40 s). The radar vibration will not affect apnea detection based on the threshold, while it will decrease the performance of classifiers involving machine learning. This disturbance will definitely leads to an inaccurate frequency estimation, regardless of whether it has an impact on the breathing pattern classification. In terms of the scenario in Figure 5.11b and Figure 5.11c, the target was simulating sleep apnea in supine and prone position respectively. Measurement shown in Figure 5.11d was conducted when the participant was lying on his side and having a normal breath. In these three cases, the jitter appears owing to a sudden hit to the table, causing an undesired spike in vital signal. This type of radar jitter often results in failure of apnea detection, no matter which detecting approach is applied. In contrast, its impact on frequency estimation could be ignored.

5.4.2. PARTICIPANTS HOLDING BREATH FOR TOO LONG

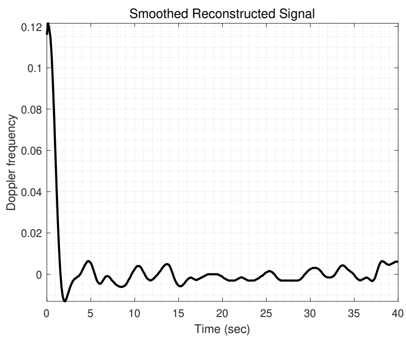

(a)

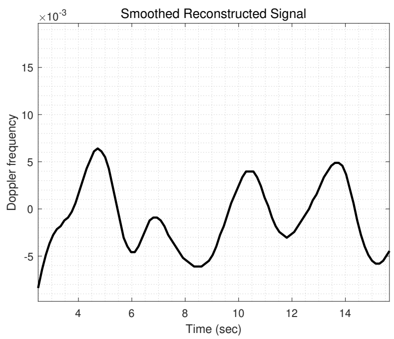

(b)

Figure 5.12: Example of the effect that participant holding breath for too long: reconstructed signal (a) reconstructed zoomed in (b)

During several measurements, the target held his breath for longer than thirty seconds, which will not occur in actual sleep apnea. The feature extracted for apnea detection is the signal amplitude, specifically the sudden drop of the signal magnitude. As could be seen in Figure 5.12a, only two seconds of normal breath could not provide us with a reliable reference of amplitude in standard breathing epoch. Meanwhile, it is not possible for us to detect apnea based on the absolute value of amplitude instead of the change in amplitude. Because when we zoom in the signal, as shown in Figure 5.12b, the absolute value in the magnitude of apnea in the supine position is comparable to that of normal breath in the prone position.

Such extreme examples account for only 2% of the total number of measurements and were retained in the evaluation of the classifier.

5.5. RESULTS IN REAL SLEEPING SCENARIO

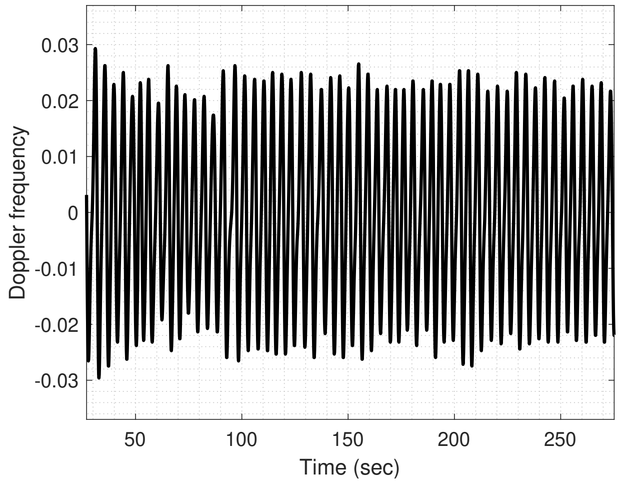

(a)

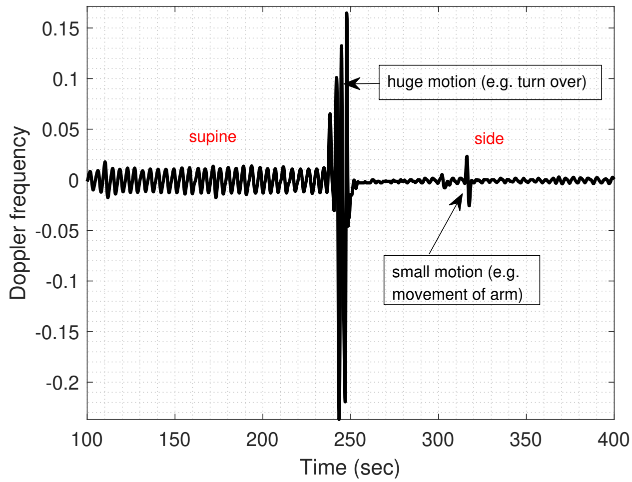

(b)

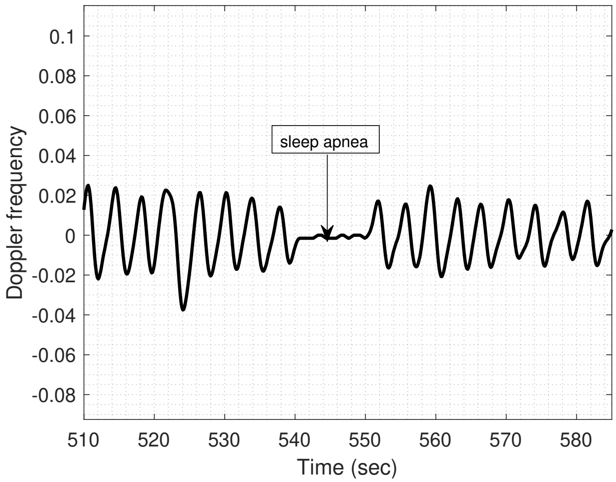

(c)

Figure 5.12: Typical examples of the measurement in sleeping scenario: (a) normal breath, (b) body movement during sleep and (c) possible sleep apnea

An experiment in real sleeping scenario was conducted, the purpose of this measurement is to argue the effectiveness of the proposed system in real sleep situations. The measurement was carried out in a home bedroom environment and the spatial relationship between the radar and the subject was similar to that in the project room described above, except that the subject was lying on a bed with a quilt instead of a yoga mat. The radar was fixed 70 cm above the chest and there was no cover between the radar and the subject except for the quilt. The subject was a healthy 23 year old female. Note that during this measurement the subject was in a natural sleep condition, which means that her body movements were not restricted. Some of the results are shown in Figure 5.12.

Figure 5.12 shows three typical examples of what appears in the measurement results. In Figure 5.13b, We could see clearly that there is a huge motion happens at about 250s, and after that the amplitude of respiration become smaller. This can be attributed to subject's turning over from supine to side. At about 320s, Doppler shows there is a small motion, but the respiration amplitude did not change after that, which indicates a consistency in posture.

As shown in Figure 5.12c, an apnea event was detected from 530s to 540s. The respiration disappeared for about ten seconds and reappear. The amplitude of breath before and after this period are the same, which means there is no change in sleeping position. An example of normal breath is demonstrated in Figure 5.13a. For most of the time not shown in the figure, there is a repetition of normal breathing in Figure 5.13a and rolling over and limb movement behaviour in Figure 5.13b. These results can be considered a good indication of realism applied to the algorithm.

5.6. VALIDATION WITH REAL PATIENT'S DATA

Furthermore, the proposed algorithm was applied to data measured on real patients to assess the overall performance of the system and made available through a research collaboration. The experiments were conducted at the Huai'an First People's Hospital, Jiangsu, China, with the participation of a patient who has been diagnosed with nocturnal respiratory disturbances. The experiment was approved by the relevant institutional review board of the hospital. Data includes up to seven hours of overnight monitoring on one patient, where the ground truth of respiratory obstruction were provided by the PSG device and the processed data collected with an FMCW radar.

5.6.1. PRE-PROCESSING OF THE RESULTS

The phase information extracted from the radar signal was also provided; Figure 5.13 and 5.14 show an example of normal breathing and respiratory obstruction as reflected in the phase information respectively. As it can be observed from the figures, the phase compensation failures caused by the phase bursts described in Section 5.2.1 are still present even in these data generated by the collaborators team. It is worth noting that this problem is prevalent in current research on radar signal processing and is an important factor limiting the accuracy of phase information, which needs to be addressed in future research.

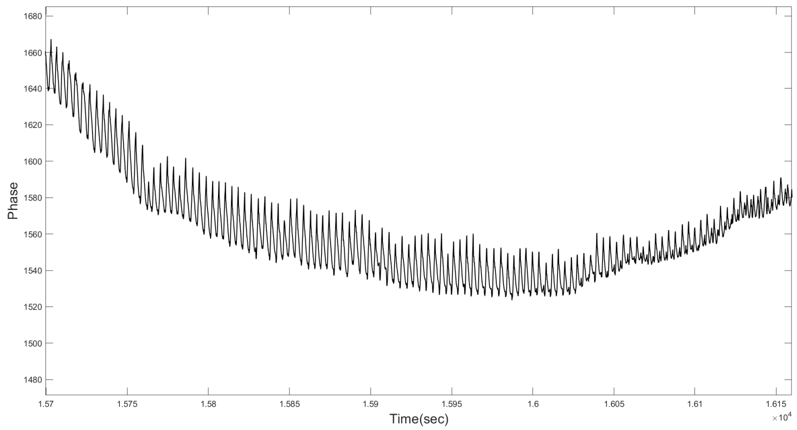

Figure 5.13: Phase information obtained by collaborators at Huai'an First People's Hospital, Jiangsu, China: an example of normal breath

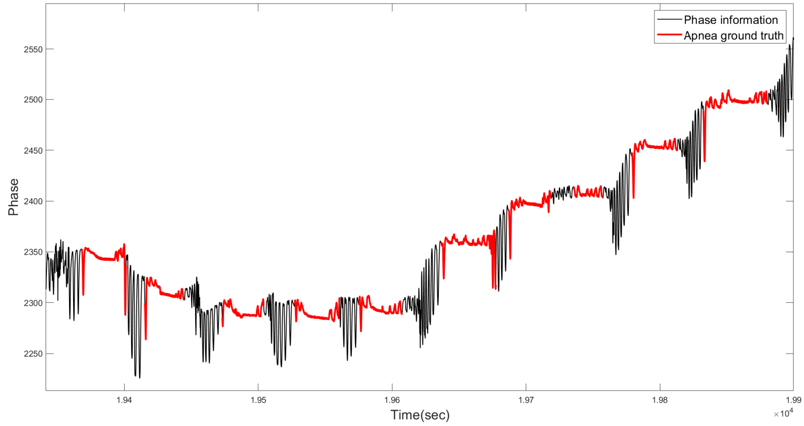

Figure 5.14: Phase information obtained by Huai'an First People's Hospital, Jiangsu, China: example of sleep apnea

5

The other two pre-processing algorithms discussed in Chapter 3 were also applied to this data set. Short-time Fourier transform (STFT) is used to generate the spectrogram of the respiration signal, followed by image-based extraction of its envelope and signal smoothing via variational mode decomposition (VMD). The reconstructed respiration signal is shown in Figure 5.15 and 5.16. Figure 5.15a demonstrates a period of normal breathing recorded while Figure 5.15b shows a record of breath containing ten apnea events, where the ground truth of apnea was marked in red. The corresponding results of Discrete Wavelet Transform (DWT) are shown in Figure 5.16a and Figure 5.16b. It is observed that there is a good correspondence between the signal obtained after processing by the proposed algorithm and the ground truth for both proposed algorithms, where spectrogram with envelope extraction methods better preserve the signal waveform. Therefore, the subsequent sleep apnea detection algorithm is based on the result of Figure 5.15.

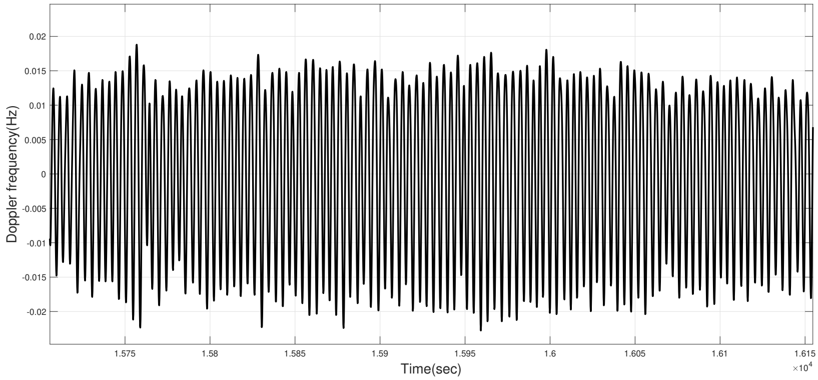

(a)

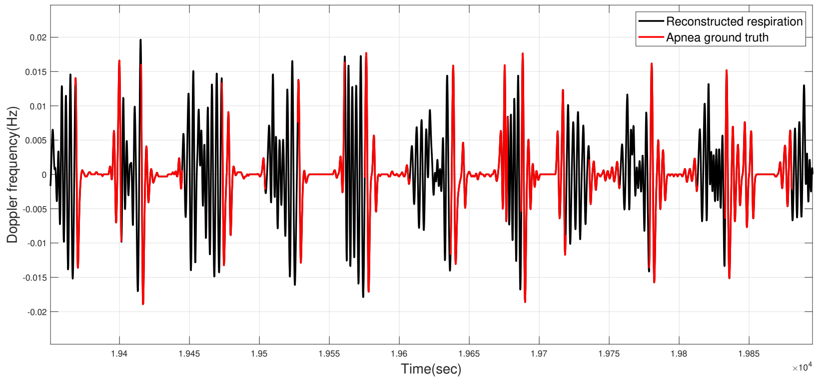

(b)

Figure 5.15: Reconstructed signal from spectrogram for real patient: (a) normal breath (b) sleep apnea episodes (with ground truth)

5

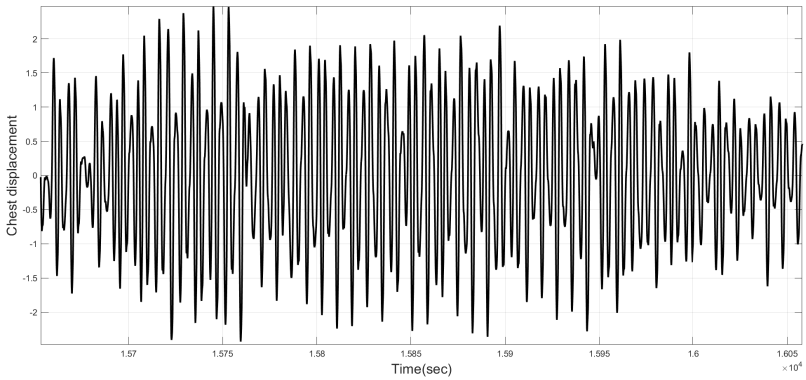

(a)

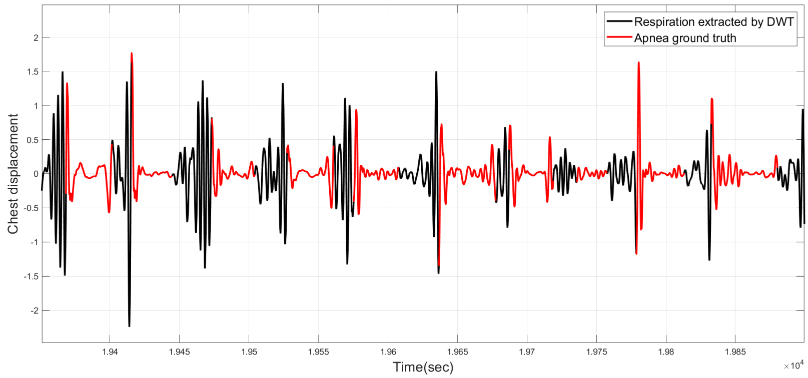

(b)

Figure 5.16: Reconstructed signal from DWT for real patient: (a) normal breath (b) sleep apnea episodes (with ground truth)

5.6.2. APNEA DETECTION RESULTS

APNEA DETECTION RESULTS VERSUS SEGMENTATION DURATION

The data obtained is an overnight monitoring period of seven hours in duration, which need to be preprocessed (results of which was discussed in the previous section) and segmented to train and test the classifier for apnea detection.

Firstly, the effect of segment duration on the results was investigated. The window size was set to 40 s, 60 s and 80 s with an overlap of 95% to sufficiently reflect the normal breathing section. Note that according to the basic facts given by the PSG, segments containing respiratory obstruction were in the majority after segmentation, causing an imbalanced data set. To prevent the model from overfitting to the majority class, it is necessary to ensure that each category in the training set contains the same number of samples. Thus, the segments labelled as normal breath were randomly upsampled by the imbalance ratio, which can be calculated by the number of class apnea segments divided by the number of normal class.

To ensure the reliability of the conclusions, the threshold method and machine learning classifier were applied separately to investigate the results of apnea detection with different segmentation durations. As indicated in Table 5.7 and 5.8, with both the application of threshold method and SVM classifier, segmentation interval of 80 second provides the best classification results. Because the duration of apnea or hypopnea is on average 25s to 45s ($Mean = 35s$ and $std = 10s$) based on the analysis of the ground truth, longer segments can contain more normal respiratory cycles, which makes it easier to capture the transition from normal breath to breathing disorders. However, a wider time window also means that the classification is less time-sensitive and less accurate in detecting the total number of occurrences of respiratory obstruction. This trade-off deserves further expansion in subsequent studies but was not discussed in depth in this final study due to time constraints. Therefore, in the following study, a cutting duration of 40s was used in order to have a more adequate amount of data and to ensure that each of the respiratory obstruction event was split out as independently as possible.

Table 5.7: Apnea Detection Results for Real Patient's data versus Segment Duration (Threshold based)

Segment Duration	Accuracy	Precision	Recall	F1 Score
40s	64.7%	59.5%	92.4%	72.4%
60s	69.9%	64.7%	87.3%	74.3%
80s	71.9%	66.9%	86.6%	75.5%

Table 5.8: Apnea Detection Results for Real Patient's data versus Segment Duration (SVM Classifier)

Segment Duration	Accuracy	Precision	Recall	F1 Score
40s	74.3%	75.0%	74.0%	74.0%
60s	89.1%	91.0%	89.0%	89.0%
80s	94.9%	95.0%	95.0%	95.0%

APNEA DETECTION RESULTS FOR DIFFERENT CLASSIFIER

The results of the respiratory patterns classification obtained by applying different classifiers with a 40s window length are shown in the Table 5.9.

Table 5.9: Apnea Detection Results for Real Patient's data - Different classifiers

Classification Methods	Accuracy	Precision	Recall	F1 Score
Threshold	64.7%	59.5%	92.4%	72.4%
KNN	62.5%	63.0%	63.0%	63.0%
SVM	74.3%	75.0%	74.0%	74.0%

Threshold-based detection methods could achieve a high level of accuracy in the previous tests due to the fact that a very idealised and simplistic model was used to simulate apnea. The effectiveness of the threshold method is directly related to the dominance of signal amplitude as a feature to distinguish normal breathing from respiratory obstruction. However, for clinical cases with real patient's data, the variation in the magnitude of chest wall displacement is far more complex than in the simulation model, let alone the disturbance of respiratory monitoring by body movement. These factors combine to make the threshold method least effective.

Note that as opposed to the previous experimental results shown in Table 5.3, the classification performance of SVM outperformed KNN in this data set of actual patient due to the large number of samples and the higher complexity and dimensionality, where the advantage of the SVM classifier became dominant. In addition, the large amount of data causes KNN to be very computationally intensive and takes a long time to obtain the classification results, which is also a very important disadvantage.

5.6.3. Error Analysis

The overall accuracy of above 74% can be considered acceptable as an initial, proof of concept result. However, studying error cases can help identify the limitations of the algorithms on realistic data.

Error Type I: Hypopnea

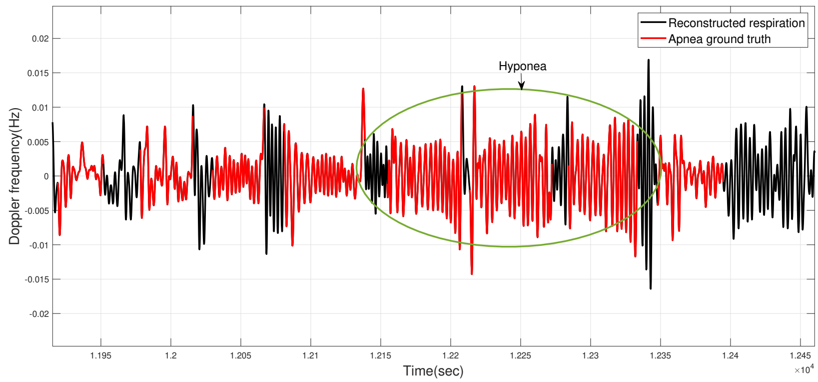

Figure 5.17: Error case for the result on real patient: Hypopnea

Figure 5.17 demonstrates the reconstructed signal for some examples where detection errors occurred. The algorithm failed to identify the hypopnea indicated by the ellipse in the figure. This is because:

1. The chest wall remains heaving when the hypopnea occurs and the reduction in amplitude of movement is not appreciable enough for the proposed algorithms to detect;
2. With successive occurrences of obstruction, the period of normal breathing between obstructed breaths was not sufficient to provide a sample against which to compare the hypopnea, which makes the algorithm failed to capture the transition between normal breath and hypopnea;

3. The fluctuations in amplitude caused by hypopnea can easily be confused with changes in chest wall displacement caused by small body movements.

ERROR TYPE II: RANDOM BODY MOVEMENT

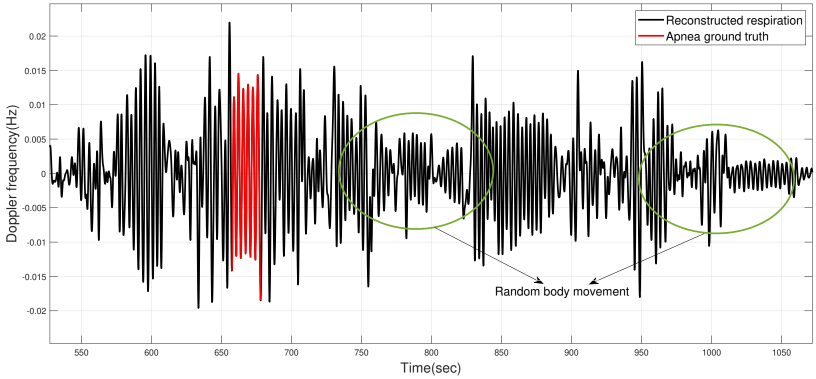

Figure 5.18: Error case for the result on real patient: Body movement

The second typical error usually occurs in records within an hour of falling asleep. This is when the patient is in a light sleep state with more physical activity, which distorted the breathing signal. As shown in Figure 5.18, during the period from 750s to 1050s, the signal amplitude fluctuated considerably, but the PSG device did not report any apnea/ hypopnea events, which could attribute to subject's random body movements. The same situation occurred in the 2018 research by Zhao et al.[86]. A set of control tests were performed, with the condition that the first hour of recording was eliminated. The results for this shortened data are shown in Table 5.10.

Table 5.10: Apnea Detection Results for Real Patient's data with segment duration of 40s; record with the first hour removed

Classification Methods	Accuracy	Precision	Recall	F1 Score
Threshold	72.1%	67.6%	72.8%	70.1%
KNN	67.1%	67.0%	68.0%	67.0%
SVM	80.1%	86.0%	80.0%	80.0%

Compared to Table 5.9, it can be observed that after discarding the first hour of data, the classification accuracy increases by about 6%.

5

ERROR TYPE III: RANDOM CASES

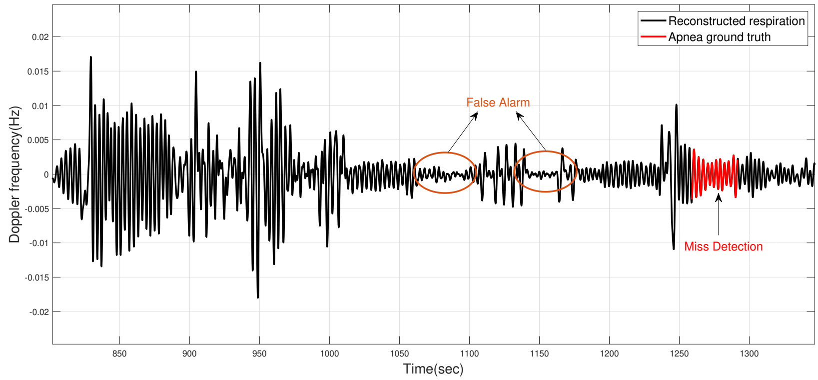

Figure 5.19: Error case for the result on real patient: Random case

Besides the two typical classification failures mentioned above, some other errors can be confusing and more challenging to explain, such as the ones shown in Figure 5.19. The two detected false alarms occur between the time intervals $[1058s, 1108s]$ and $[1138s, 1164s]$. In terms of the reduced signal, there is a clear decrease in respiratory amplitude of more than 50%; however, the ground truth is labelled as normal breathing. In contrast, the PSG system reported a sleep apnea between $1258s$ to $1291s$, whereas only a fluctuation in amplitude of less than 10% occurred here. The author's analysis of the causes of this phenomenon is set out below:

1. Apnea is a more complex phenomenon that just movements of the chest/abdomen. Although chest wall displacement is the most important factor that can be relied upon to determine respiratory obstruction, it is not the only and 100% absolute relevant factor.

2. In some transient episodes of OSA and MSA, the chest wall displacement remains at its original magnitude, but oxygenation does not happen because no air goes down to the lungs. This cannot be checked relying only on the radar data as done for this initial analysis in this section.

3. Very unlikely but still possible to be errors in the recording of PSG equipment.

In summary, the proposed method of extracting the spectrogram envelope as well as the classification algorithms is also feasible for these realistic data, providing an accuracy of at least 74% percent. It can be considered a good proof of concept result, but to generalise this to clinical significance there are further steps to take. Although the proposed algorithm achieves encouraging results in experiments in which healthy subjects held their breath to simulate respiratory obstruction, it does not work as well as expected on real cases. Here listed several possible improvements that could be done as follow up work:

1. Body movement cancellation algorithm can be explored;

2. Conduct more experiments to increase the amount of training data;

3. Try to apply classifiers involving deep learning to further improve the detection accuracy.

4. Combine other vital signals that can be obtained by radar or other contactless sensors and related to apnea event to provide a more comprehensive and clinically meaningful diagnosis.

5.7. CONCLUSION

In this chapter, the environment settings and procedure to verify the experiment of respiration monitoring using UWB radar are first presented. Then the effectiveness of the proposed algorithm is then verified by analysis of its performance on experimental data. The main contents and results are summarised below:

1. How the pre-processing algorithms described in Chapter 3 perform on the measured data is studied. Then the results are compared with the ground truth obtained from the respiration belt to further validate the algorithm. With regard to signal processing algorithms, the following comments can be made:

    - The phase extraction results were analysed, and it was found that in some instances, incorrect phase compensation was performed due to the presence of phase glitch points. In turn, if the phase compensation threshold is enlarged or if phase compensation is skipped, new problems are introduced, causing phase demodulation to fail. While the phase extraction works in general, solving the problems encountered sporadically for these episodes remains an aspect to address in future work.
    - In contrast to the phase extraction approach, spectrogram and DWT provide us with required details of thorax movements with breath-to-breath accuracy, where signal restored by spectrogram provides stronger evidence for apnea detection.
    - The signal after envelope extraction and smoothing was compared with the data measured by the respiration belt to prove its consistency with the ground truth, providing in general good agreement as can be seen in 5.2.4.

2. The effectiveness of the proposed classifiers was verified by experimental data with 14 participants measured in several body positions. Initial classification results on experimental data in controlled conditions (i.e. participants holding breath to simulate sleep apnea) show encouraging results with performance metrics above 90%.

3. Then Koda's algorithm[12] from the state of the art was explained and compared with ours in terms of the performance on apnea detection. An improvement strategy to his method was also proposed and valued.

4. A study was conducted to examine how sleep position, the presence of a blanket and gender altered the results of apnea detection. Classification results were found to be independent of gender and blanket coverage but correlated with sleep position. The

highest accuracy rate is achieved in the supine scenario with 96%, followed by lateral lying with 90% accuracy, followed by prone lying with 86% accuracy.

5. The non-ideal nature of the experimental environment and its effect on the results are analysed, focusing mainly on the radar jitter and subjects holding their breath for too long. These non-idealities of the experiment performed can be addressed in future verification studies to be performed as follow-up of this thesis.

6. The effectiveness of the developed system in the actual sleep environment with a subject sleeping in their bedroom has also been confirmed.

7. The proposed algorithm was applied on whole-night radar monitoring data obtained from real patients, reproducing the respiratory signal well and obtaining an acceptable classification accuracy. The error cases were analysed from a comprehensive perspective. Although further steps remains to be taken before clinical application, the results demonstrate the potential of the developed system to assist in clinical diagnosis.

6
Conclusion and Future Work

6.1. Conclusion

This research aims to develop a contactless, radar-based sleep apnea detection method; patients can be in either supine, side or prone position. In order to achieve this, development and simulations of signal processing algorithms that can provide the required details of thorax/abdomen movements and breath-to-breath accuracy is needed. Thus a simulation environment is built where target is assumed to be 0.5 m away from the radar and chest wall displacement information is stored in the radar range history. A signal processing pipeline is proposed which includes Doppler frequency based and phase based signal reconstruction method as well as three respiratory obstruction diagnostic approaches. The validation of the methods is conducted via simulation as well as experimental data collected on 14 volunteers in controlled conditions, including supine, side and prone positions and the presence of a blanket.

The main contributions of this thesis research are summarised below:

- The cardiopulmonary physiological activity of the human body is mathematically modelled with signals beyond simple sinusoidal functions. Then an appropriate model for monitoring respiration based on FMCW radar system and a simulation tool that allows modelling multiple subjects in a Monte Carlo fashion as well as different types of sleep apnea is established, with different sleep positions also being taken into account.
- A signal processing pipeline involving spectrogram envelope extraction based on image processing and signal smoothing (specifically VMD, Variational Mode Decomposition) algorithms is specifcally proposed and compared with the phase demodulation algorithm and discrete wavelet transform. Analysis of the algorithms' performance on simulated as well as experimental data reveals that the spectrogram and image processing based algorithm provides the highest accuracy in detecting sleep apnea.

- Monte Carlo simulations for different subjects and different environments are performed to validate the proposed algorithm in a modelling environment, taking into account different sleep postures. Simulation results show that at signal-to-noise ratios greater than 5 dB, the proposed pre-processing algorithm can recover the respiratory signal waveform well enough to use it as a feature for sleep apnea detection with all three applied classification algorithms demonstrating classification accuracies of over 90%. Simulations of standardised sleeping postures show that in a low SNR environment, the RCS becomes the most pivotal factor in detection effectiveness due to the direct correlation with the received signal energy.

- Initial results on simulated and experimental data in controlled conditions (i.e. participants holding breath to simulate sleep apnea) show encouraging results with performance metrics above 90%. The result is compared with state of art algorithm that proposed by Takato Koda[12] and one of its improved algorithm. Good agreement between radar measurements and a reference respiration belt is also demonstrated. Based on the experiment, a number of factors that may affect the results of the sleep apnea detection were also investigated. The results demonstrate that for all the different sleeping positions, the classification accuracy can reach more than 80%, with the highest accuracy in the supine scenario reaching 96%, followed by lateral lying with 90% accuracy, followed by prone lying with 86%. In contrast, the gender of the subjects and the presence or absence of a blanket had no effect on the classification success rate.

- The potential of the system for more realistic applications is confirmed by providing an example of monitoring a longer recording of respiration in real conditions in a home bedroom.

- The proposed algorithm was applied to radar data obtained from real patients and achieved a classification accuracy of up to more than 80%, demonstrating the potential of the developed system for clinical applications.

6.2. Future Work

1. The problem of phase demodulation failure due to phase mutation, identified in Chapter 5, is not perfectly addressed by the proposed scheme. This remains a major obstacle limiting the use of phase signal only as an effective feature for reliable respiratory impairment detection. An element of possible future work can be to investigate a final solution to this problem;

2. While this study explored the detection of sleep apnea in different sleep positions, it did not develop a solution when the subject was moving (e.g. turning over). Thus there is a great need for studying the algorithms for monitoring of vital signals and the diagnosis of respiratory obstruction in humans in the presence of significant and continuous movements;

3. In the study, it was found that clutter and multiple targets, as well as unconscious body movements, can cause interference with radar signals, both in the home and ward environment. As shown in Chapter 5, the simplest moving target identification

algorithm applied to Koda's algorithm can improve the detection success rate. Thus the exploration of algorithms that can distinguish between ward ambient clutter and interference caused by multiple targets and unconscious body movements can be an essential part of the next stage of research; Blind Source Separation (BSS) technique could be one option;

4. Sleep apnea, especially mixed sleep apnea, often shows complex clinical pathology, which means that chest wall displacement is not the only diagnostic vital characteristic. A combination of respiration and other physiological signals such as blood pressure, SaO_2, and carotid pulses (obtained by radar monitoring of the neck or head) can be considered to help obtain more accurate and clinically meaningful results;

5. As described in Chapter 1 in an overview of the different contactless sleep monitoring schemes available today, the various sensors used for respiratory monitoring (e.g. Camera-Based sensor, passive infrared sensor and pressure sensor) all have their advantages and disadvantages. Each of these solutions has many researchers working on them. This allows the fusion of radar-derived features with those from other contactless sensors for more accurate respiratory obstruction detection;

6. In this study, only two simple machine learning methods were considered. There is still plenty of room to explore in the field of deep learning, combined with estimation theory to study real-time respiratory obstruction detection.

REFERENCES

[1] N. Long, K. Wang, R. Cheng, K. Yang, W. Hu, and J. Bai, "Assisting the visually impaired: multitarget warning through millimeter wave radar and RGB-depth sensors," *Journal of Electronic Imaging*, vol. 28, no. 1, pp. 1 – 15, 2019. [Online]. Available: https://doi.org/10.1117/1.JEI.28.1.013028

[2] R. P. Pedrosa, L. F. Drager, C. C. Gonzaga, M. G. Sousa, L. K. de Paula, A. C. Amaro, C. Amodeo, L. A. Bortolotto, E. M. Krieger, T. D. Bradley, and G. Lorenzi-Filho, "Obstructive sleep apnea," *Hypertension*, vol. 58, no. 5, pp. 811–817, 2011. [Online]. Available: https://www.ahajournals.org/doi/abs/10.1161/HYPERTENSIONAHA.111.179788

[3] P. Lévy, M. Kohler, W. T. McNicholas, F. Barbé, R. D. McEvoy, V. K. Somers, L. Lavie, and J.-L. Pépin, "Obstructive sleep apnoea syndrome," *Nature Reviews Disease Primers*, vol. 1, Jun 2015.

[4] A. V. Benjafield, N. T. Ayas, P. R. Eastwood, R. Heinzer, M. S. M. Ip, M. J. Morrell, C. M. Nunez, S. R. Patel, T. Penzel, J.-L. Pépin, P. E. Peppard, S. Sinha, S. Tufik, K. Valentine, and A. Malhotra, "Estimation of the global prevalence and burden of obstructive sleep apnoea: a literature-based analysis," *The Lancet Respiratory Medicine*, vol. 7, no. 8, pp. 687–698, 2019.

[5] J. C. Jun, S. Chopra, and A. R. Schwartz, "Sleep apnoea," *European Respiratory Review*, vol. 25, no. 139, pp. 12–18, 2016. [Online]. Available: https://err.ersjournals.com/content/25/139/12

[6] A. R. Motamedi KK, McClary AC, "Obstructive sleep apnea: a growing problem," vol. 9, no. 3, pp. 149–53, 2009.

[7] I. T. Mohamad W, "Obstructive sleep apnoea hypopnea syndrome - an overview." vol. 6, no. 1, pp. 2–6, 2011.

[8] C. L. Ralls F, "A contemporary review of obstructive sleep apnea." vol. 25, no. 6, pp. 578–593, 2019.

[9] D. J. Eckert, A. S. Jordan, P. Merchia, and A. Malhotra, "Central sleep apnea: Pathophysiology and treatment," *Chest*, vol. 131, no. 2, pp. 595–607, 2007. [Online]. Available: https://www.sciencedirect.com/science/article/pii/S0012369215483515

[10] R. T. Muza, "Central sleep apnoea—a clinical review," *Journal of Thoracic Disease*, vol. 7, no. 5, 2015. [Online]. Available: https://jtd.amegroups.com/article/view/4455

[11] R. J. Thomas, J. E. Mietus, C.-K. Peng, G. Gilmartin, R. W. Daly, A. L. Goldberger, and D. J. Gottlieb, "Differentiating Obstructive from Central and Complex Sleep Apnea Using an Automated Electrocardiogram-Based Method," *Sleep*, vol. 30, no. 12, pp. 1756–1769, 12 2007. [Online]. Available: https://doi.org/10.1093/sleep/30.12.1756

[12] T. Koda, T. Sakamoto, S. Okumura, H. Taki, S. Hamada, and K. Chin, "Radar-based automatic detection of sleep apnea using support vector machine," in *2020 International Symposium on Antennas and Propagation (ISAP)*, 2021, pp. 841–842.

[13] A. D. Droitcour, O. Boric-Lubecke, S. Yamada, and V. M. Lubecke, *Introduction*. John Wiley Sons, Ltd, 2016, ch. 1, pp. 1–20. [Online]. Available: https://onlinelibrary.wiley.com/doi/abs/10.1002/9781119078418.ch1

[14] S. Ancoli-Israel, R. Cole, C. Alessi, M. Chambers, W. Moorcroft, and C. P. Pollak, "The Role of Actigraphy in the Study of Sleep and Circadian Rhythms," *Sleep*, vol. 26, no. 3, pp. 342–392, 05 2003. [Online]. Available: https://doi.org/10.1093/sleep/26.3.342

[15] A. Domingues, T. Paiva, and J. M. Sanches, "Sleep and wakefulness state detection in nocturnal actigraphy based on movement information," *IEEE Transactions on Biomedical Engineering*, vol. 61, no. 2, pp. 426–434, 2014.

[16] T. Yilmaz, R. Foster, and Y. Hao, "Detecting vital signs with wearable wireless sensors," *Sensors*, vol. 10, no. 12, pp. 10 837–10 862, 2010. [Online]. Available: https://www.mdpi.com/1424-8220/10/12/10837

[17] J. L. Martin and A. D. Hakim, "Wrist actigraphy," *Chest*, vol. 139, no. 6, pp. 1514–1527, 2011. [Online]. Available: https://www.sciencedirect.com/science/article/pii/S0012369211603140

[18] E. Dafna, A. Tarasiuk, and Y. Zigel, "Sleep-wake evaluation from whole-night non-contact audio recordings of breathing sounds," *PLOS ONE*, vol. 10, no. 2, pp. 1–22, 02 2015. [Online]. Available: https://doi.org/10.1371/journal.pone.0117382

[19] K. Humphreys, C. Markham, and T. Ward, "A cmos camera-based system for clinical photoplethysmographic applications," in *SPIE OPTO-Ireland*, 2005.

[20] V. Hers, D. Corbugy, I. Joslet, P. Hermant, J. Demarteau, B. Delhougne, G. Vandermoten, and J. Hermanne, "New concept using passive infrared (pir) technology for a contactless detection of breathing movement: a pilot study involving a cohort of 169 adult patients," *Journal of Clinical Monitoring and Computing*, vol. 27, pp. 521 – 529, 2013.

[21] I. Sadek, T. T. S. Heng, E. Seet, and B. Abdulrazak, "A new approach for detecting sleep apnea using a contactless bed sensor: Comparison study," *Journal of Medical Internet Research*, vol. 22, 2020.

[22] L. Antognoli, S. Moccia, L. Migliorelli, S. Casaccia, L. Scalise, and E. Frontoni, "Heartbeat detection by laser doppler vibrometry and machine learning," *Sensors*, vol. 20, no. 18, 2020. [Online]. Available: https://www.mdpi.com/1424-8220/20/18/5362

[23] F. Tan, S. Chen, W. Lyu, Z. Liu, C. Yu, C. Lu, and H.-Y. Tam, "Non-invasive human vital signs monitoring based on twin-core optical fiber sensors," *Biomed.*

Opt. Express, vol. 10, no. 11, pp. 5940–5952, Nov 2019. [Online]. Available: http://www.osapublishing.org/boe/abstract.cfm?URI=boe-10-11-5940

[24] J. Le Kernec, F. Fioranelli, C. Ding, H. Zhao, L. Sun, H. Hong, J. Lorandel, and O. Romain, "Radar signal processing for sensing in assisted living: The challenges associated with real-time implementation of emerging algorithms," *IEEE Signal Processing Magazine*, vol. 36, no. 4, pp. 29–41, 2019.

[25] H. Hong, L. Zhang, H. Zhao, H. Chu, C. Gu, M. Brown, X. Zhu, and C. Li, "Microwave sensing and sleep: Noncontact sleep-monitoring technology with microwave biomedical radar," *IEEE Microwave Magazine*, vol. 20, no. 8, pp. 18–29, 2019.

[26] W. Massagram, V. M. Lubecke, A. HØst-Madsen, and O. Boric-Lubecke, "Assessment of heart rate variability and respiratory sinus arrhythmia via doppler radar," *IEEE Transactions on Microwave Theory and Techniques*, vol. 57, no. 10, pp. 2542–2549, 2009.

[27] E. Antolinos, F. García-Rial, C. Hernández, D. Montesano, J. I. Godino-Llorente, and J. Grajal, "Cardiopulmonary activity monitoring using millimeter wave radars," *Remote Sensing*, vol. 12, no. 14, 2020.

6

[28] E. Turppa, J. M. Kortelainen, O. Antropov, and T. Kiuru, "Vital sign monitoring using fmcw radar in various sleeping scenarios," *Sensors*, vol. 20, no. 22, 2020.

[29] A. Ahmad, J. C. Roh, D. Wang, and A. Dubey, "Vital signs monitoring of multiple people using a fmcw millimeter-wave sensor," in *2018 IEEE Radar Conference (RadarConf18)*, 2018, pp. 1450–1455.

[30] F. Lin, Y. Zhuang, C. Song, A. Wang, Y. Li, C. Gu, C. Li, and W. Xu, "Sleepsense: A noncontact and cost-effective sleep monitoring system," *IEEE Transactions on Biomedical Circuits and Systems*, vol. 11, no. 1, pp. 189–202, 2017.

[31] K. Sun, D.-K. Kim, Y. Lee, Y.-H. Lim, H.-K. Park, S. H. Cho, and S. H. Cho, "Non-contact diagnosis of obstructive sleep apnea using impulse-radio ultra-wideband radar," *Scientific Reports*, vol. 10, 03 2020.

[32] M. Baboli, A. Singh, B. Soll, O. Boric-Lubecke, and V. M. Lubecke, "Wireless sleep apnea detection using continuous wave quadrature doppler radar," *IEEE Sensors Journal*, vol. 20, no. 1, pp. 538–545, 2020.

[33] N. Du, K. Liu, L. Ge, and J. Zhang, "Apnearadar: A 24ghz radar-based contactless sleep apnea detection system," in *2017 2nd International Conference on Frontiers of Sensors Technologies*, 2017, pp. 372–376.

[34] C. Wang, J.-H. Chan, S.-H. Fang, H.-T. Cheng, and Y.-L. Hsu, "Novel sleep apnea detection based on uwb artificial intelligence mattress," in *2019 IEEE International Conference on Artificial Intelligence Circuits and Systems (AICAS)*, 2019, pp. 158–159.

[35] D. R. Morgan and M. G. Zierdt, “Novel signal processing techniques for doppler radar cardiopulmonary sensing,” *Signal Processing*, vol. 89, no. 1, pp. 45–66, 2009. [Online]. Available: https://www.sciencedirect.com/science/article/pii/S0165168408002211

[36] X. Hu and T. Jin, “Short-range vital signs sensing based on eemd and cwt using ir-uwb radar,” *Sensors*, vol. 16, no. 12, 2016.

[37] L. Sun, H. Hong, Y. Li, C. Gu, F. Xi, C. Li, and X. Zhu, “Noncontact vital sign detection based on stepwise atomic norm minimization,” *IEEE Signal Processing Letters*, vol. 22, no. 12, pp. 2479–2483, 2015.

[38] M. Donelli, “A rescue radar system for the detection of victims trapped under rubble based on the independent component analysis algorithm,” *Progress in Electromagnetics Research M*, vol. 19, pp. 173–181, 2011.

[39] H. B. Kwon, D. Son, D. Lee, H. Yoon, M. H. Lee, Y. J. Lee, S. H. Choi, and K. S. Park, “Hybrid cnn-lstm network for real-time apnea-hypopnea event detection based on ir-uwb radar,” *IEEE Access*, pp. 1–1, 2021.

[40] V. P. Tran, A. A. Al-Jumaily, and S. M. S. Islam, “Doppler radar-based non-contact health monitoring for obstructive sleep apnea diagnosis: A comprehensive review,” *Big Data and Cognitive Computing*, vol. 3, no. 1, 2019. [Online]. Available: https://www.mdpi.com/2504-2289/3/1/3

[41] C. Li, J. Ling, J. Li, and J. Lin, “Accurate doppler radar noncontact vital sign detection using the relax algorithm,” *IEEE Transactions on Instrumentation and Measurement*, vol. 59, no. 3, pp. 687–695, 2010.

[42] J. Li, L. Liu, Z. Zeng, and F. Liu, “Advanced signal processing for vital sign extraction with applications in uwb radar detection of trapped victims in complex environments,” *IEEE Journal of Selected Topics in Applied Earth Observations and Remote Sensing*, vol. 7, no. 3, pp. 783–791, 2014.

[43] L. Sun, S. Huang, Y. Li, C. Gu, H. Pan, H. Hong, and X. Zhu, “Remote measurement of human vital signs based on joint-range adaptive eemd,” *IEEE Access*, vol. 8, pp. 68 514–68 524, 2020.

[44] M. Kagawa, H. Tojima, and T. Matsui, “Non-contact screening system for sleep apnea-hypopnea syndrome using the time-varying baseline of radar amplitudes,” in *2014 IEEE Healthcare Innovation Conference (HIC)*, 2014, pp. 99–102.

[45] A. Q. Javaid, C. M. Noble, R. Rosenberg, and M. A. Weitnauer, “Towards sleep apnea screening with an under-the-mattress ir-uwb radar using machine learning,” in *2015 IEEE 14th International Conference on Machine Learning and Applications (ICMLA)*, 2015, pp. 837–842.

[46] J. Xiong, J. Jiang, H. Hong, C. Gu, Y. Li, and X. Zhu, “Cw radar based osa detection solution with residual comparison method,” in *2019 IEEE MTT-S International Microwave Biomedical Conference (IMBioC)*, vol. 1, 2019, pp. 1–3.

[47] A. De Groote, M. Wantier, G. Cheron, M. Estenne, and M. Paiva, "Chest wall motion during tidal breathing," *Journal of Applied Physiology*, vol. 83, no. 5, pp. 1531–1537, 1997, pMID: 9375316. [Online]. Available: https://doi.org/10.1152/jappl.1997.83.5.1531

[48] T. Kondo, T. Uhlig, P. Pemberton, and P. Sly, "Laser monitoring of chest wall displacement," *The European respiratory journal*, vol. 10, no. 8, p. 1865—1869, 1997. [Online]. Available: https://doi.org/10.1183/09031936.97.10081865

[49] G. Ramachandran, "Three-dimensional reconstruction of cardiac displacement patterns on the chest wall during the p, qrs and t-segments of the ecg by laser speckle inteferometry," *Medical Biological Engineering Computing*, vol. 27, no. 5, pp. 525–530, 1989.

[50] M. Baldi, F. Appignani, B. Zanaj, and F. Chiaraluce, "Body movement compensation in uwb radars for respiration monitoring," 10 2012.

[51] V. LD., "Obstructive sleep apnea," *American family physician*, vol. 60, no. 8, pp. 2279–2286, 1999.

[52] F. Qi, C. Li, S. Wang, H. Zhang, J. Wang, and G. Lu, "Contact-free detection of obstructive sleep apnea based on wavelet information entropy spectrum using bio-radar," *Entropy*, vol. 18, no. 8, 2016. [Online]. Available: https://www.mdpi.com/1099-4300/18/8/306

[53] A. D. M. Fulvio Gini and L. Patton, *Waveform Design and Diversity for Advanced Radar Systems*. Institution of Engineering and Technology, 2012. [Online]. Available: https://app.knovel.com/hotlink/toc/id:kpWDDARS01/waveform-design-diversity/waveform-design-diversity

[54] W. L. Melvin and J. A. Scheer, *Principles of Modern Radar, Volume 3 - Radar Applications*. Institution of Engineering and Technology, 2014. [Online]. Available: https://app.knovel.com/hotlink/toc/id:kpPMRVRA06/principles-modern-radar/principles-modern-radar

[55] M.-G. Di Benedetto and G. Giancola, *Understanding Ultra Wide Band Radio Fundamentals*. Prentice Hall PTR, 2004.

[56] T. Z. et al., *Ultra-wideband RF system engineering*. Cambridge University Press, 2013.

[57] J. R. Fernandes and D. Wentzloff, "Recent advances in ir-uwb transceivers: An overview," in *Proceedings of 2010 IEEE International Symposium on Circuits and Systems*, 2010, pp. 3284–3287.

[58] A. Lázaro, D. Girbau, and R. Villarino, "Analysis of vital signs monitoring using an ir-uwb radar," *Progress in Electromagnetics Research-pier*, vol. 100, pp. 265–284, 2010.

[59] D. Espès, A. Pistea, C. Canaff, I. Iordache, P. L. Parc, and E. Rădoi, “New method for localization and human being detection using uwb technology: Helpful solution for rescue robots,” *ArXiv*, vol. abs/1312.4162, 2013.

[60] D. Yim, W. H. Lee, J. I. Kim, K. Kim, D. H. Ahn, Y.-H. Lim, S. H. Cho, H.-K. Park, and S. H. Cho, “Quantified activity measurement for medical use in movement disorders through ir-uwb radar sensor,” *Sensors*, vol. 19, no. 3, 2019. [Online]. Available: https://www.mdpi.com/1424-8220/19/3/688

[61] J. W. Choi, S. S. Nam, and S. H. Cho, “Multi-human detection algorithm based on an impulse radio ultra-wideband radar system,” *IEEE Access*, vol. 4, pp. 10 300–10 309, 2016.

[62] P. Wang, F. Qi, M. Liu, F. Liang, H. Xue, Y. Zhang, H. Lv, and J. Wang, “Noncontact heart rate measurement based on an improved convolutional sparse coding method using ir-uwb radar,” *IEEE Access*, vol. 7, pp. 158 492–158 502, 2019.

[63] L. Ren, Y. S. Koo, H. Wang, Y. Wang, Q. Liu, and A. E. Fathy, “Noncontact multiple heartbeats detection and subject localization using uwb impulse doppler radar,” *IEEE Microwave and Wireless Components Letters*, vol. 25, no. 10, pp. 690–692, 2015.

[64] D. Wang, S. Yoo, and S. H. Cho, “Experimental comparison of ir-uwb radar and fmcw radar for vital signs,” *Sensors*, vol. 20, no. 22, 2020. [Online]. Available: https://www.mdpi.com/1424-8220/20/22/6695

[65] Aardal and J. Hammerstad, “Medical radar literature overview,” *NorwayNorwegian Defence Research Establishment (FFI)*, 2010. [Online]. Available: http://hdl.handle.net/20.500.12242/2409

[66] J. Wang, X. Wang, L. Chen, J. Huangfu, C. Li, and L. Ran, “Noncontact distance and amplitude-independent vibration measurement based on an extended dacm algorithm,” *IEEE Transactions on Instrumentation and Measurement*, vol. 63, no. 1, pp. 145–153, 2014.

[67] A. E. Espíritu Santo and C. Carbajal, “Respiration rate extraction from ecg signal via discrete wavelet transform,” in *2010 2nd Circuits and Systems for Medical and Environmental Applications Workshop (CASME)*, 2010, pp. 1–4.

[68] M. N. Dar, M. U. Akram, A. Usman, and S. A. Khan, “Ecg biometric identification for general population using multiresolution analysis of dwt based features,” in *2015 Second International Conference on Information Security and Cyber Forensics (InfoSec)*, 2015, pp. 5–10.

[69] M. Shensa, “The discrete wavelet transform: wedding the a trous and mallat algorithms,” *IEEE Transactions on Signal Processing*, vol. 40, no. 10, pp. 2464–2482, 1992.

[70] M. Omidvar, A. Zahedi, and H. Bakhshi, “Eeg signal processing for epilepsy seizure detection using 5-level db4 discrete wavelet transform, ga-based feature selection and

ann/svm classifiers," *Journal of Ambient Intelligence and Humanized Computing*, pp. 1–9, 2021.

[71] T. Gandhi, B. K. Panigrahi, and S. Anand, "A comparative study of wavelet families for eeg signal classification," *Neurocomputing*, vol. 74, no. 17, pp. 3051–3057, 2011. [Online]. Available: https://www.sciencedirect.com/science/article/pii/S0925231211003158

[72] A. Abbate, C. DeCusatis, and P. Das, "Wavelets and subbands: Fundamentals and applications," 2002.

[73] V. J. Samar, A. Bopardikar, R. Rao, and K. Swartz, "Wavelet analysis of neuroelectric waveforms: A conceptual tutorial," *Brain and Language*, vol. 66, no. 1, pp. 7–60, 1999. [Online]. Available: https://www.sciencedirect.com/science/article/pii/S0093934X98920247

[74] K. D. Tzimourta, L. G. Astrakas, M. G. Tsipouras, N. Giannakeas, A. T. Tzallas, and S. Konitsiotis, "Wavelet based classification of epileptic seizures in eeg signals," in *2017 IEEE 30th International Symposium on Computer-Based Medical Systems (CBMS)*, 2017, pp. 35–39.

[75] I. Daubechies, J. Lu, and H.-T. Wu, "Synchrosqueezed wavelet transforms: An empirical mode decomposition-like tool," *Applied and Computational Harmonic Analysis*, vol. 30, no. 2, pp. 243–261, 2011. [Online]. Available: https://www.sciencedirect.com/science/article/pii/S1063520310001016

[76] J. Gilles, "Empirical wavelet transform," *IEEE Transactions on Signal Processing*, vol. 61, no. 16, pp. 3999–4010, 2013.

[77] J. R. Carson, "Notes on the theory of modulation," *Proceedings of the Institute of Radio Engineers*, vol. 10, pp. 57–64.

[78] K. Dragomiretskiy and D. Zosso, "Variational mode decomposition," *IEEE Transactions on Signal Processing*, vol. 62, no. 3, pp. 531–544, 2014.

[79] R. B. Berry, R. Budhiraja, D. J. Gottlieb, D. Gozal, C. Iber, V. K. Kapur, C. L. Marcus, R. Mehra, S. Parthasarathy, S. F. Quan, S. Redline, K. P. Strohl, S. L. D. Ward, and M. M. Tangredi, "Rules for scoring respiratory events in sleep: Update of the 2007 aasm manual for the scoring of sleep and associated events," *Journal of Clinical Sleep Medicine*, vol. 08, no. 05, pp. 597–619, 2012. [Online]. Available: https://jcsm.aasm.org/doi/abs/10.5664/jcsm.2172

[80] B. Tay, J. K. Hyun, and S. Oh, "A machine learning approach for specification of spinal cord injuries using fractional anisotropy values obtained from diffusion tensor images," *Computational and mathematical methods in medicine*, vol. 2014, p. 276589, 01 2014.

[81] S. Visa, B. Ramsay, A. Ralescu, and E. V. D. Knaap, "Confusion matrix-based feature selection."

[82] A. Oksenberg and D. S. Silverberg, "The effect of body posture on sleep-related breathing disorders: facts and therapeutic implications," *Sleep Medicine Reviews*, vol. 2, no. 3, pp. 139–162, 1998. [Online]. Available: https://www.sciencedirect.com/science/article/pii/S1087079298900181

[83] K. Mase, T. Noguchi, M. Tagami, S. Imura, K. Tomita, M. Monma, M. Nozoe, S. Takashima, and K. Kawakatsu, "Compression of the lungs by the heart in supine, side-lying, semi-prone positions," *Journal of Physical Therapy Science*, vol. 28, pp. 2470 – 2473, 2016.

[84] S. Takashima, M. Nozoe, K. Mase, Y. Kouyama, K. Matsushita, and H. Ando, "Effects of posture on chest-wall configuration and motion during tidal breathing in normal men," *Journal of Physical Therapy Science*, vol. 29, no. 1, pp. 29–34, 2017.

[85] Vernier, *Go Direct® Respiration Belt*, Vernier, 13979 SW Millikan Way, Beaverton, OR 97005 USA, 3 2021. [Online]. Available: https://www.vernier.com/files/manuals/gdx-rb/gdx-rb.pdf

[86] H. Zhao, H. Hong, D. Miao, Y. Li, H. Zhang, Y. Zhang, C. Li, and X. Zhu, "A non-contact breathing disorder recognition system using 2.4-ghz digital-if doppler radar," *IEEE Journal of Biomedical and Health Informatics*, vol. 23, no. 1, pp. 208–217, 2019.